University of California
Los Angeles

Computational Conformal Geometry and its Applications to Human Brain Mapping

A dissertation submitted in partial satisfaction
of the requirements for the degree
Doctor of Philosophy in Mathematics

by

Lok Ming Lui

2008

The dissertation of Lok Ming Lui is approved.

Luminita A. Vese

Paul M. Thompson

Mark Green

Tony F. Chan, Committee Chair

University of California, Los Angeles

2008

To my parents, brother and fiancee . . .

for their love and constant support.

Table of Contents

List of Figures

List of Tables

Acknowledgments

I would like to express my deepest gratitude to my advisor Prof. Tony F. Chan for his constant encouragement, guidance and support throughout my years at UCLA. I would also like to express my appreciation to Dr. Yalin Wang for his continuous guidance and suggestions. I am also thankful to Prof. Shing-Tung Yau for his valuable advice on differential geometry. My appreciation is further extended to Prof. Paul M. Thompson for his invaluable support and advice on the medical research. I would also like to thank my committee members, Prof. Luminita Vese and Prof. Mark Green, for their suggestions in my oral exams and PhD thesis.

Besides, I would like to extend my deepest gratitude to my parents, my brother and my fiancee. Without their encouragement, I would not be able to go through all the challenges and finish my PhD study at UCLA. Special thanks to my friends and schoolmates who were always with me during my study at UCLA.

Furthermore, I would like to thank the Department of Mathematics at UCLA and the Institute of Pure and Applid Mathematics (IPAM) for providing me with a comfortable environment and computing facilities for my research and study.

Finally, I would like to acknowledge that this dissertation was supported in part by the National Institutes of Health through the NIH Roadmap for Medical Research, grant U54 RR021813 entitled Center for Computational Biology (CCB). Additional support was provided by the NIH/NCRR resource grant P41 RR013642; National Science Foundation (NSF) under Contract DMS-0610079 and ONR Contract N0014-06-1-0345. This work was performed while Prof. Tony F. Chan was on leave at the National Science Foundation as Assistant Director

of the Directorate for Mathematics.

Vita

1981	Born, Hong Kong, China.
2003	B.S. (Mathematics), Hong Kong University of Science and Technology
2003-2004	Teaching Assistant, Department of Mathematics, UCLA. Taught: Multivariable Calculus, Linear Algebra, Complex Analysis, Differential Geometry.
2005	M.A. (Applied Mathematics), UCLA, Los Angeles, California.
2004 - 2007	Research Assistant, Department of Mathematics, UCLA.
2006 - 2007	President, UCLA Student Chapter of Society of Industrial and Applied Mathematics (SIAM)
2007	Visting Researcher, Microsoft Research Asia (from June 2007 - September 2007). Research Mentor for the RIPS@Beijing Program. Mentoring two research projects: 1. Hyperbolic Desktop; 2. Link Analysis of Google Page Rank.
2007-2008	Teaching Assistant, Department of Mathematics, UCLA. Taught: Multivariable Calculus.

Publications

L.M. Lui, Y. Wang, T.F. Chan, and P.M. Thompson, "Brain Anatomical Feature Detection by Solving Partial Differential Equations on General Manifolds", Discrete and Continuous Dynamical Systems B, 7(3), May 2007, pp. 605-618

L.M. Lui, Y. Wang, T.F. Chan and P.M. Thompson, "Landmark Constrained Genus Zero Surface Conformal Mapping and Its Application to Brain Mapping Research", Applied Numerical Mathematics 57, 2007, pp. 847-858

Y. Wang, L. M. Lui, X. Gu, K.M. Hayashi, T.F. Chan, P.M. Thompson and S.-T. Yau, "Brain Surface Conformal Parameterization using Riemann Surface Structure", IEEE Transaction of Medical Imaging, 26(6), June 2007, pp. 853-865

L. M. Lui, Y. Wang, T.F. Chan and P.M. Thompson, "Automatic Landmark Tracking and Its Application to the Optimization of Brain Conformal Mapping", IEEE Computer Society Conference on Computer Vision and Pattern Recognition (CVPR), New York, NY, Jun. 2006

L. M. Lui, Y. Wang, T.F. Chan and P.M. Thompson, "Automatic A Landmark-based Brain Conformal Parametrization with Automatic Landmark Tracking Technique" International Conference on Medical Image Computing and Computer Assisted Intervention - MICCAI 2006, LNCS 4191 pp. 308-316

L.M. Lui, Y. Wang, T.F. Chan, " PDE on manifold using global conformal parametrization", Variational, Geometric, and Level Set Methods in Computer Vision: Third International Workshop, VLSM 2005, Beijing, China, Oct. 16, 2005, pp. 307-319

Y. Wang, L.M. Lui, T.F. Chan and P.M. Thompson, "Optimization of Brain Conformal Mapping with Landmarks", Medical Image Computing and Computer-Assisted Internvention - MICCAI 2005: 8th International Conference, Palm Springs, CA USA, Oct. 26-29, 2005, Proceedings, Part II, pp. 675-683

B. Gutman, Y. Wang, L. M. Lui, T. F. Chan, and P.M. Thompson , " Hippocampal Surface Analysis Using Spherical Harmonic Function Applied to Surface Conformal Mapping ", 8th International Conference on Pattern Recognition (ICPR), Hong Kong, China, 2006, Vol. 3, pp. 964-967

B. Gutman, Y. Wang, L.M. Lui, T.F. Chan, P.M. Thompson, " Hippocampal Surface Discrimination via Invariant Descriptors of Spherical Conformal Maps", IEEE International Symposium on Biomedical Imaging - From Nano to Macro (ISBI), Washington D.C., USA, 2007, pp. 1316-1319

L.M. Lui, S. Thiruvenkadam, Y. Wang, P.M. Thompson and T. F. Chan, Optimized Conformal Parameterizations of Cortical Surfaces Using Shape Based Landmark Matching, Proceeding of 11th International Conference on Medical Image Computing and Computer Assisted Intervention, MICCAI 2008

L.M. Lui, Y. Wang, J. Kwan, and S. T. Yau , "Computation of Curvatures using Conformal Parameterization", Communications in Information and Systems

ABSTRACT OF THE DISSERTATION

Computational Conformal Geometry and its Applications to Human Brain Mapping

by

Lok Ming Lui

Doctor of Philosophy in Mathematics

University of California, Los Angeles, 2008

Professor Tony F. Chan, Chair

Analyzing the data and performing computation effectively on surfaces with complicated geometry is an important research topic, especially in Human Brain Mapping. In this work, we are interested in computing the conformal structure of the Riemann surface and applying it to Human Brain Mapping. In order to analyze the brain data efficiently, the complicated brain cortical surface is usually parameterized to a simple parameter domain such as the sphere or 2D rectangles. This allows us to transform the 3D problems into 2D problems. In order to compare data more effectively, the parameterization has to preserve the geometry of the brain structure while aligning the important anatomical features consistently. Conformal parameterization, that preserves the local geometry, is often used. In our work, we propose algorithms to compute the optimized conformal parameterization of the brain surface which aligns the anatomical features consistently while preserving the conformality of the parameterization as much as possible. With the conformal parameterization, we can solve variational problems and partial differential equations on the surface easily by solving the corresponding equations on the 2D parameter domain. The computation is simple because

of the simple Riemannian metric of the conformal map. Finally, we develop an automatic landmark tracking algorithm to detect the sulcal landmarks on the brain cortical surface, which involves solving variational problems on the brain surface.

CHAPTER 1

Introduction

Rapid development of computer technology has accelerated the acquisition and databasing of brain data. Analyzing the data and performing computation effectively on the brain surface with complicated geometry has become an important research topic in the Human Brain Mapping research. An effective way to do so is to parameterize them into a canonical space while retaining the original geometric information as far as possible. In this dissertation, we are interested in computing the conformal structure (or conformal parametrization) of the Riemann surface and applying it to brain mapping research.

Generally speaking, every Riemann surface (metric surface) admits a conformal structure. A conformal structure is a natural geometric structure on the Riemann surface, which governs many physical phenomena and embeds many geometric information of the surface. Specifically, a conformal structure is an "angle preserving" atlas of the surface, such that angles among tangent vectors can be coherently defined on different local coordinate systems. Consequently, a conformal parameterization of a surface preserves the local geometry of the surface. It is the main reason why conformal mapping is often used in the Human Brain Mapping research. With the conformal structure, concepts in complex analysis can be defined on the surface and it makes computation possible and easier on the surface. It is important in medical research such as solving variational problems or PDEs on brain cortical surfaces to analyze brain data. In this dissertation, we focus on the discussion of how we can compute the optimized conformal parameterization that aligns the landmark features while preserving the conformality as much as possible , and also how the conformal parameterization can be applied such as solving PDEs on brain surfaces, automatic detection of anatomical features and so on.

The organization of the dissertation is as follow. In Chapter 2, we briefly describe the mathematical background related to our work. These includes the basic mathematical definition from the conformal geometry, different approaches to compute the conformal structure of the Riemann surface, definition of geometric variants and so on.

In Chapter 3, we describe a variational method to compute the optimized conformal parameterizations of cortical surfaces which improve the alignment of the important anatomical features (landmarks) while preserving the conformality as much as possible. Here, we assume the landmarks are already labeled and the correspondence between landmarks on different cortical surfaces are known. This is done by minimizing a compounded energy which consists of the harmonic energy and the landmark mismatch energy.

In Chapter 4, we describe an explicit method to solve variational problems on general Riemann surfaces, using the conformal parameterization and covariant derivatives defined on the surface. This is done by mapping the surface conformally to the two dimensional rectangular domains, by computing the holomorphic 1-form on the surface. The conformal parameterization has a simple Riemannian metric. As a result, any PDEs or variational problems on the surface can be formulated to a 2D problem with a simple formula and can be efficiently solved by well developed numerical scheme on the 2D domain.

In Chapter 5, we present an algorithm to automatically detect sulcal landmark curves on cortical surfaces . This is done by two steps. First, we obtain a hypothesized landmark region using the Chan-Vese segmentation method, which solves a Partial Differential Equation (PDE) on a manifold with global conformal parameterization. Second, we propose an automatic landmark curve tracing method based on the principal directions of the local Weingarten matrix.

In Chapter 6, we describe an algorithm to find parametrizations of the cortical surfaces that are close to conformal and also give a shape-based correspondence between embedded landmark curves. Here, we assume the sulcal landmarks are labeled but the correspondence between landmarks on different cortical surfaces are not known. We propose a variational approach by minimizing an energy that measures the harmonic energy of the parameterizations, and the shape dissimilarity between mapped points on the landmark curves. The parameterizations computed are guaranteed to give a shape-based diffeomorphism between the landmark curves. We formulate our problem as a variational energy defined on a search space of diffeomorphisms generated as integral flows of smooth vector fields. The vector fields are restricted only to those that do not flow across the landmark curves, so as to enforce the exact landmark matching.

CHAPTER 2

Mathematical Background

In this chapter, we describe briefly the basic mathematical background related to our work in this dissertation.

2.1 Basic Definitions in Conformal Geometry

A surface with a conformal structure is called a *Riemann surface*. All metric surfaces are Riemann surfaces. Mathematically, a Riemann surface (S, g) (with Riemannian metric g) is a real differentiable two dimensional manifold S in which each tangent space is equipped with an inner product g in a manner which varies smoothly from point to point. This allows one to define various notions such as angles, lengths of curves, areas (or volumes), curvature, gradients of functions and divergence of vector fields [2][3][4]. Specifically, a Riemannian metric $g = \{g_p\}_{p \in S}$ on S is a family of inner products:

$$g_p : T_pS \times T_pS \to \mathbb{R}, \quad p \in S \tag{2.1}$$

such that, for all differentiable vector field X, Y, the application $p \mapsto g_p(X(p), Y(p))$ is differentiable. Let $\{(\frac{\partial}{\partial x_i})_p\}_i$ be a basis of tangent vectors over $p \in S$. Then, the coefficients

$$g_{ij}(p) :=< (\frac{\partial}{\partial x_i})_p, (\frac{\partial}{\partial x_j})_p >_p \tag{2.2}$$

induces a metric tensor, which is called the first fundamental form:

$$g := \sum_{ij} g_{ij} dx_i \wedge dx_j \tag{2.3}$$

Every Riemann surface admits a *conformal structure*. A *conformal structure* is a special atlas of the surface, such that angles among tangent vectors can be coherently defined on different local coordinate systems.

An *atlas* of a Riemann surface S is a family of charts $\{U_\alpha, \phi_\alpha\}$ for which U_α constitutes an open covering of S. As shown in Figure 2.1, suppose $\{U_\alpha, \phi_\alpha\}$ and $\{U_\beta, \phi_\beta\}$ are two charts on the surface S, $U_\alpha \cap U_\beta \neq \emptyset$, then the chart transition function, $\phi_{\alpha\beta}$ is defined as:

$$\phi_{\alpha\beta} = \phi_\beta \circ \phi_\alpha^{-1} : \phi_\alpha(U_\alpha \cap U_\beta) \to \phi_\beta(U_\alpha \cap U_\beta) \tag{2.4}$$

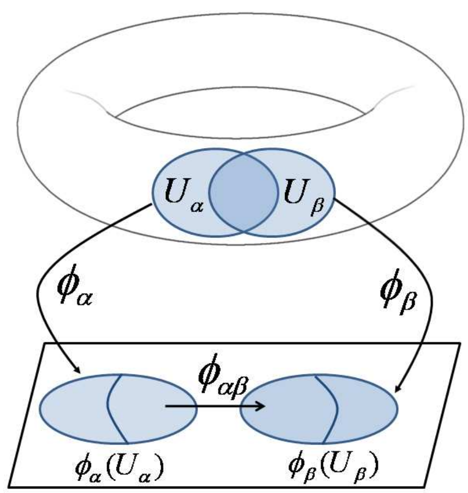

Figure 2.1: The structure of a manifold. An atlas is a family of charts that jointly form an open covering of the manifold

An atlas $\{U_\alpha, \phi_\alpha\}$ on a surface is called *conformal* if all chart transition function are holomorphic. A chart $\{U_\alpha, \phi_\alpha\}$ is *compatible* with an atlas $\mathcal{A}$ if the union $\mathcal{A} \cup \{U_\alpha, \phi_\alpha\}$ is still a conformal atlas. Two conformal atlases are compatible if their union is still a conformal atlas. Each conformal compatible equivalence class is a *conformal structure*. Strictly speaking, a two-manifold with a conformal structure is called a Riemann surface. It has been proven that all metric orientable surfaces are Riemann surfaces and admit conformal structures [5][6].

With the notion of conformal structure, holomorphic and meromorphic functions and differential forms can be generalized to Riemann surfaces. A holomorphic 1-form ω is a complex differential form, such that in each local frame $< u_\alpha, v_\alpha >$, $z_\alpha = u_\alpha + \mathbf{i}v_\alpha$, where $\mathbf{i} = \sqrt{-1}$, the parametric representation is $\omega = f(z_\alpha)dz_\alpha$ and $f(z_\alpha)$ is a holomorphic function. On a different chart $\{U_\beta, \phi_\beta\}$, with another local frame (u_β, v_β), $z_\beta = u_\beta + \mathbf{i}v_\beta$, where $\mathbf{i} = \sqrt{-1}$,

$$\omega = f_\beta(z_\beta)dz_\beta = f_\beta(z_\beta(z_\alpha))\frac{dz_\beta}{dz_\alpha}dz_\alpha \tag{2.5}$$

then $f_\beta(\frac{dz_\beta}{dz_\alpha})$ is still a holomorphic function. For a genus g closed surface, all holomorphic 1-forms form a $2g$ real dimensional linear space [7].

At a *zero point* $p \in M$ of a holomorphic 1-form ω, any local parametric representation has

$$\omega = f(z_\alpha)dz_\alpha, f|_p = 0. \tag{2.6}$$

According to the Riemann-Roch theorem, in general there are $2g-2$ zero points for a holomorphic 1-form defined on a closed surface of genus g, where $g > 1$.

A holomorphic 1-form induces a special system of curves on a surface, the so-called *conformal net* [8]. Horizontal trajectories are the curves that are mapped to iso-v lines in the parameter domain. Similarly, vertical trajectories are the curves that are mapped to iso-u lines in the parameter domain. The horizontal

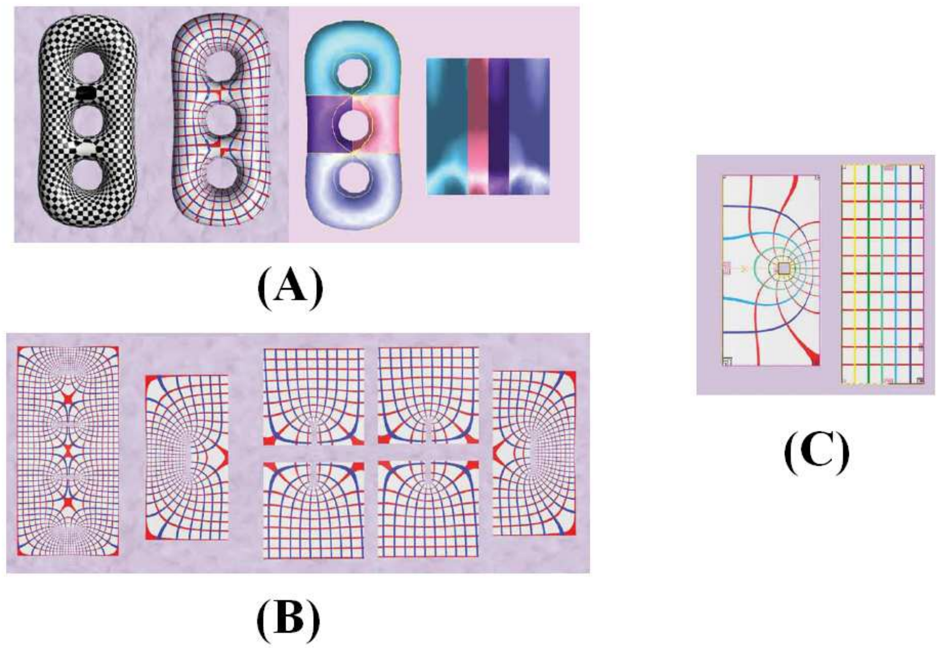

Figure 2.2: (A). Conformal net and critical graph of a closed 3-hole torus surface. There are 4 zero points, the critical horizontal trajectories partition the surface to 4 topological cylinders, color encoded in the 3rd frame. Each cylinder is conformally mapped to a planar rectangle. (B). Conformal net and critical graph of a open boundary 4-hole annulus on the plane. There are 3 zero points; the critical horizontal trajectories partition the surface to 6 topological disks. (C). Each segment is conformally mapped to a rectangle. The trajectories and the boundaries are color encoded and the corners are labelled.

and vertical trajectories form a web on the surface. The trajectories that connect zero points, or a zero point with the boundary are called *critical trajectories*. The critical horizontal trajectories form a graph, which is called the *critical graph*. In general, the behavior of a trajectory may be very complicated, it may have infinite length and may be dense on the surface. If the critical graph is finite, then all the horizontal trajectories are finite.

The critical graph partitions the surface into a set of non-overlapping patches that jointly cover the surface, and each patch is either a topological disk or a topological cylinder [9]. Each patch $\Omega \subset M$ can be mapped to the complex plane by the integration of holomorphic 1-form on it. The structure of the critical graph and the parameterizations of the patches are determined by the conformal structure of the surface. If two surfaces are topologically homeomorphic to each other and have similar geometrical structure, they can support consistent critical graphs and segmentations (i.e., surface partitions), and their parameterizations are consistent as well (a possible metric to evaluate how similar two surfaces' geometrical structures are is proposed as E_{dist} in [10]). Therefore, by matching their parameter domains, the entire surfaces can be directly matched in 3D. This generalizes prior work in medical imaging that has matched surfaces by computing a smooth bijection to a single canonical surface, such as a sphere or disk.

Figure 2.2 (A) and (B) show the conformal net and critical graph on closed surface and open boundary surface, respectively. The surface segmentation results are also shown. Figure 2.2 (C) illustrates how a segment in (B) is conformally mapped to a rectangle. In (C), conformal nets are labeled with different colors. In the parameter domain, we can also find the right angles between the conformal net curves are well preserved. The zero point on the left is mapped to two points on the opposite edges.

We call the process of finding the critical graph and segmentation as *holomorphic flow segmentation*, a process that is completely determined by the geometry of the surface and the choice of the holomorphic 1-form. Note that this differs from the typical meaning of segmentation in medical imaging, and is concerned with the segmentation, or partitioning, of a general surface. Computing holomorphic 1-forms is equivalent to solving elliptic differential equations on the surfaces, and in general, elliptic differential operators are stable (their solutions tend to be smooth functions and the boundary conditions of the Dirichlet problem can be

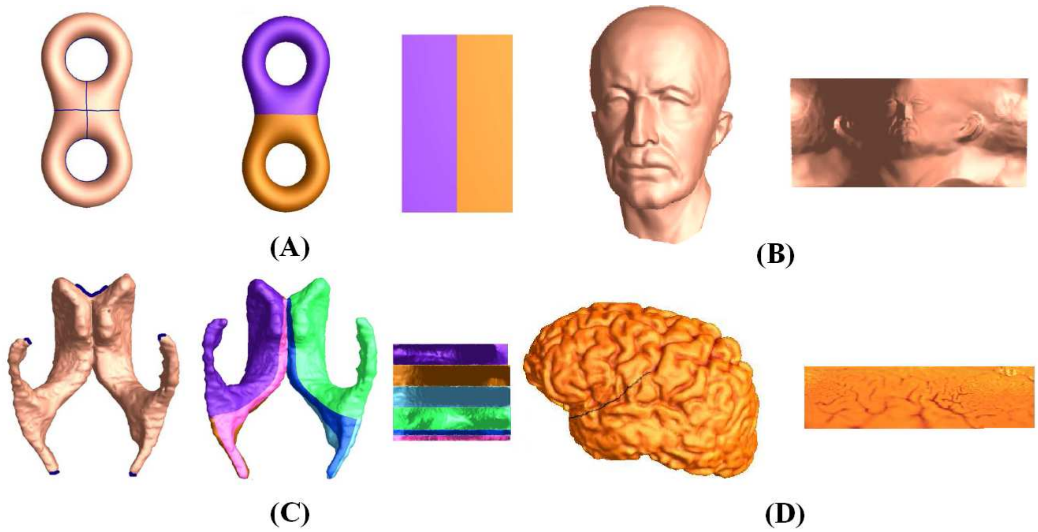

Figure 2.3: Illustration of the conformal parameterizations of different surfaces. The parameterizations are computed by integrating the holomorphic differential one form defined on the surfaces. (A), (B), (C) and (D) show the conformal parameterizations of a 2-torus, a human face, a lateral ventricular surface and a human brain cortical surface [1] respectively.

fulfilled). Therefore the resulting surface segmentations and parameterizations are intrinsic and stable, and are applicable for matching (potentially noisy) surfaces that are derived from medical images and topologically homeomorphic to each other [1]. Because the behavior of horizontal trajectory is solely determined by the conformal structure and the cohomology class of the holomorphic 1-form. In surface matching application, we guarantee that the cohomology classes are consistent on two surfaces and the two surfaces are with similar conformal structures, therefore, the corresponding trajectories will behave in the similar way.

2.2 Conformal Parameterization of the Riemann Surface

In this section, we talk about the conformal parameterization of the Riemann surface.

All Riemann surfaces are locally Euclidean. Given two Riemann surfaces M and N. We can represent them locally as $\phi_M(x_1, x_2) : R^2 \rightarrow M \subseteq R^3$ and $\phi_N(x_1, x_2) : R^2 \rightarrow N \subseteq R^3$ respectively, where (x_1, x_2) are their coordinates. The inner product of the tangent vectors at each point of the surface can be represented by its first fundamental form. The first fundamental form on M can be written as $ds_M^2 = \sum_{i,j} g_{ij} dx^i dx^j$, where $g_{ij} = \frac{\partial \phi_M}{\partial x^i} \cdot \frac{\partial \phi_M}{\partial x^j}$ and $i, j = 1, 2$. Similarly, the first fundamental form on N can be written as $ds_N^2 = \sum_{i,j} \widetilde{g}_{ij} dx^i dx^j$ where $g_{ij} = \frac{\partial \phi_N}{\partial x^i} \cdot \frac{\partial \phi_N}{\partial x^j}$ and $i, j = 1, 2$. Given a map $f : M \rightarrow N$ between the M and N. With the local parameterization, f can be represented locally by its coordinates as $f : R^2 \rightarrow R^2$, $f(x_1, x_2) = (f_1(x_1, x_2), f_2(x_1, x_2))$. Every tangent vectors $\vec{v}$ on M can be mapped (*push forward*) by f to a tangent vectors $f_*(\vec{v})$ on N. The inner product of the vectors $f_*(\vec{v_1})$ and $f_*(\vec{v_2}))$, where $\vec{v_1}$ and $\vec{v_2}$ are tangent vectors on M, is:

$$
\begin{aligned}
f^*(ds_N^2)(v_1, v_2) &:= < f_*(v_1), f_*(v_2) > \\
&= \sum_{i,j} \widetilde{g}_{ij} f_*(v_i) \cdot f_*(v_j) \\
&= \sum_{i,j} (\sum_{m,n} \widetilde{g}_{mn} \frac{\partial f_i}{\partial x^m} \frac{\partial f_j}{\partial x^n}) v_i v_j)
\end{aligned}
\tag{2.7}
$$

Therefore, a new Riemannian metric $f^*(ds_N^2)$ on M is induced by f and ds_N^2, called the *pull back metric*. We say that the map f is *conformal* if it preserves the first fundamental form up to a scaling factor. Mathematically, it means:

$$f^*(ds_N^2) = \lambda(x_1, x_2) ds_M^2 \tag{2.8}$$

The scaling factor λ is called the *conformal factor*.

A parameterization $\varphi : R^2 \rightarrow M$ is a *conformal parameterization* if φ is a conformal map.

Intuitively, a map is conformal if it preserves the inner product of the tangent vectors up to a scaling factor, called the conformal factor λ. An immediate consequence is that every conformal map preserves angles.

Figure 2.3 shows several examples of conformal parameterization examples. Figure 2.3(A), 2.3(B), 2.3(C) and 2.3(D) show the conformal parameterizations of a 2-torus, a human face, a lateral ventricular surface and a brain cortical surface respectively [1].

As an illustration of how conformal maps are angle-preserving, Figure 2.4(A) shows the texture mapping of a human brain. The brain is conformally mapped to a sphere. The sphere is mapped to the plane by sterographic projection. The planar coordinates are used as the texture coordinates. This texture parameter is mapped to the brain surface through the conformal mapping between the sphere and the brain surface. Note that all the right angles in the texture are preserved on the brain surface. Figure 2.4(B)shows the texture mapping of the human face. The face is conformally mapped to a 2D rectangle. The right angle is also well preserved under the conformal map.

Several research groups have reported work on brain surface conformal mapping. Brain surface parameterization has been studied intensively. Schwartz et al. [11], and Timsari and Leahy [12] compute quasi-isometric flat maps of the cerebral cortex. Drury et al. [13] present a multiresolution flattening method for mapping the cerebral cortex to a 2D plane [14]. Hurdal and Stephenson [15][16] reported a discrete mapping approach that uses circle packing to produce “flattened” images of cortical surfaces on the sphere, the Euclidean plane, or the hyperbolic plane. They obtained maps that are quasi-conformal approximations to classical conformal maps. Haker et al. [17][18] implemented a finite element

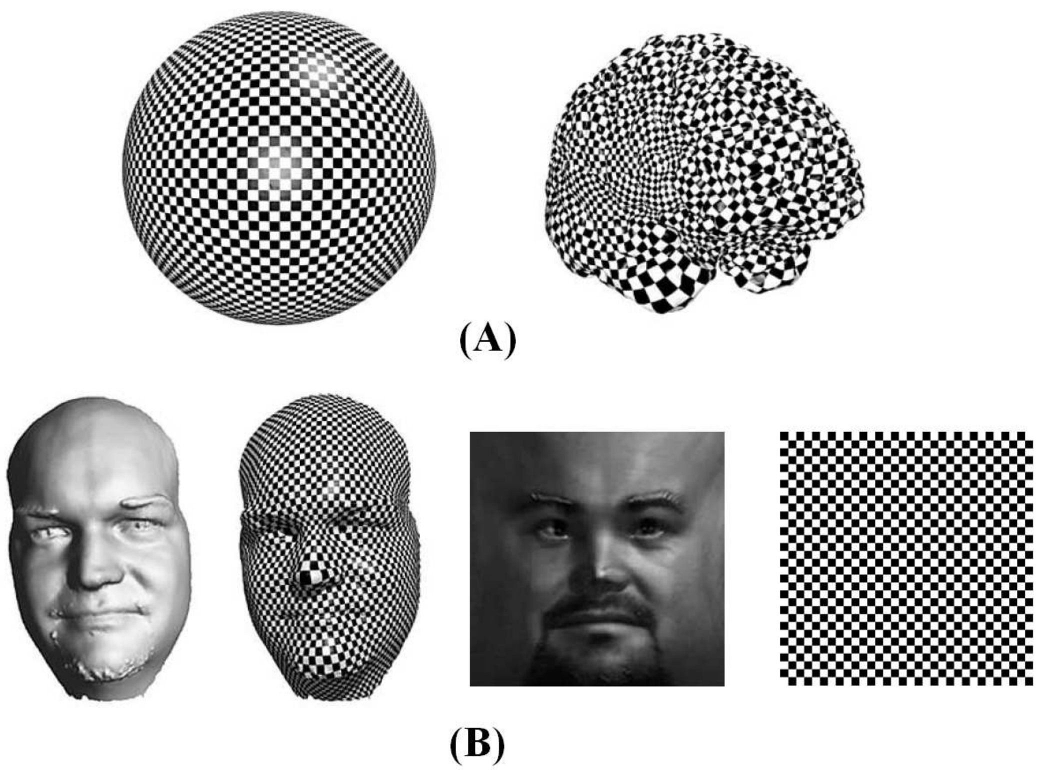

Figure 2.4: (A) shows the conformal texture mapping of the human brain. The brain is mapped conformally to a sphere. (A) left shows the texture mapping of the sphere. (B) shows the texture mapping of the brain. Note that the right angle is well-preserved, meaning that conformal mapping is angle-preserving. (B) shows the texture mapping of the human face. The face is conformally mapped to a 2D rectangle. The right angle is also well preserved under the conformal map.

approximation for parameterizing brain surfaces via conformal mappings. They represented the Laplace-Beltrami operator as a linear system and solved it for parameterizing brain surfaces via conformal mapping. Gu et al. [19] proposed a method to find a unique conformal mapping between any two genus zero manifolds by minimizing the harmonic energy of the map. They demonstrated this method by conformally mapping the cortical surface to a sphere. For general surfaces, Wang et al. [20][1][21] proposed a method to compute the conformal structures of high genus surfaces using the holomorphic 1-forms. They illustrated this ideas by computing conformal structures for several types of anatomical surfaces in MRI scans of the brain, including the cortex, hippocampus, and lateral ventricles. Based on the Riemann surface structure, they then canonically partitioned the surface into patches and each of these patches can be conformally mapped to a parallelogram. Ju et al. [22] present a least squares conformal mapping method for cortical surface flattening. Joshi et al. [23] propose a scheme to parameterize the surface of the cerebral cortex by minimizing an energy functional in the p^{th} norm. Recently, Ju et al. [24] report the results of a quantitative comparison of FreeSurfer [25], CirclePack [15], and least squares conformal mapping (LSCM) [22] with respect to geometric distortion and computational speed.

In our work, we apply the global conformal parameterization algorithms to parameterize the genus zero Riemann surface to a sphere and parameterize higher genus surface to the 2D rectangles [1][26][27]. The algorithms are described as below.

2.2.1 Computation of Conformal Parameterization of Genus Zero surface

For a diffeomorphism $f : S_1 \to S_2$ between two genus zero surfaces, a map is conformal if it minimizes the harmonic energy, $E_{harmonic}(f)$ [28]. Let g_1 and g_2 are the metric on S_1 and S_2 respectively. The harmonic energy $E_{harmonic}$ is defined as:

$$E_{harmonic}(f) = \frac{1}{2}\int_{S_1} |\nabla_{g_1} f|^2_{g_2} d_{S_1} \tag{2.9}$$

where ∇_g is the gradient operator with respect to the metric g and $|\cdot|_{g_2}$ is the norm in the image space with respect to the metric g_2. (In coordinates, we have $|\nabla_{g_1} f|^2_{g_2} = tr({}^t\partial f \partial f)$, where ∂f is the matrix of partial derivatives expressed in bases orthonormal with respect to g_1 and g_2.

Based on this fact, we can compute the conformal mapping by a variational approach, which minimizes the harmonic energy. The Euler-Lagrange equation of the harmonic energy is:

$$\frac{d}{dt} f^t = \Delta_{g_1} f \tag{2.10}$$

where $\Delta_{g_1} f$ is the Laplacian operator with respect to the metric g_1 and is a tangent vector on S_2.

In this section,we will formulate the basic mathematical theory in a rigorous way. The harmonic energy and its derivative will be defined. Since we are working on a triangulated mesh, their discretized version will be discussed.

Let K and H represent the simplicial realization (triangulation) of the Riemann surface S_1 and S_2 respectively, u, v dentote the vertices, and $[u, v]$ denote the edge spanned by u, v. Now, we use $C^{PL}(K)$ to denote the vector space of all piecewise linear functions defined on K. Suppose a set of string $k_{u,v}$ are assigned to each edge $[u,v]$. An inner product can be defined on $C^{PL}(K)$ as follow:

$$< f,h >= \frac{1}{2} \sum_{[u,v]\in K} k_{u,v}(f(u)-f(v))(h(u)-h(v)) \tag{2.11}$$

The string energy is defined as:

$$E(f) =< f,f >= \frac{1}{2} \sum_{[u,v]\in K} k_{u,v}(f(u)-f(v))^2 \tag{2.12}$$

Suppose edge $[v_1,v_2]$ has two adjacent faces T_α, T_β, with $T_\alpha = \{v_1,v_2,v_3\}$, $T_\beta = \{v_1,w_3,v_2\}$. Define the parameters on T_α

$$a^{\alpha}_{v_1,v_2} = \frac{(v_1-v_3)\cdot(v_2-v_3)}{2|(v_1-v_3)\times(v_2-v_3)|} \tag{2.13}$$

$$a^{\alpha}_{v_2,v_3} = \frac{(v_2-v_1)\cdot(v_3-v_1)}{2|(v_2-v_1)\times(v_3-v_1)|} \tag{2.14}$$

$$a^{\alpha}_{v_3,v_1} = \frac{(v_3-v_2)\cdot(v_1-v_2)}{2|(v_3-v_2)\times(v_1-v_2)|} \tag{2.15}$$

Parameters on T_β are defined similarly. Let $k_{v_1,v_2} := \frac{1}{2}(cot\alpha + cot\beta) = a^{\alpha}_{v_1,v_2} + a^{\beta}_{v_1,v_2}$. The string energy obtained is the harmonic energy $E_{harmonic}(f)$.

For a map $\overrightarrow{f} \in C^{PL}$, $\overrightarrow{f} = (f_0, f_1, f_2)$, we define the harmonic energy as:

$$E_{harmnoic}(\overrightarrow{f}) = \sum_{i=0}^{2} E_{harmonic}(f_i) \tag{2.16}$$

For a map between two genus zero surfaces, the map is conformal if the map is the minimizer of the harmonic energy $E_{harmnonic}$. The harmonic energy is always a quadratic form and is positive definite. This will guarantee the convergence of the steepest descent method.

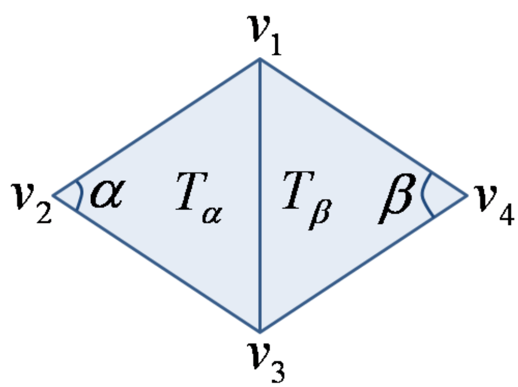

Figure 2.5: Discrete Laplace-Beltrami operator. Edge $\{v_1, v_2\}$ has two corners against it α, β The edge weight is defined as the summation of the cotangents of these corner angles.

To minimize the harmonic energy by the steepest descent method, we define the piecewise Laplacian. The piecewise Laplacian is the linear operator $\triangle_{PL}(f)$: $C^{PL} \to C^{PL}$ on the space of piecewise linear functions on K, defined on the formula

$$\triangle_{PL}(f) = \sum_{[u,v]\in K} k_{u,v}(f(u) - f(v)) \tag{2.17}$$

For a map $\vec{f} = (f_0, f_1, f_2)$, the piecewise Laplacian of $\vec{f}$ is defined as:

$$\triangle_{PL}(\vec{f}) = (\triangle_{PL}(f_0), \triangle_{PL}(f_1), \triangle_{PL}(f_2)) \tag{2.18}$$

A map $\vec{f}$ is harmonic if and only if Δ_{PL} only has a normal component, and its tangential component is zero. That is:

$$\Delta_{PL}(\vec{f}) = (\Delta_{PL}\vec{f})^{\perp} \tag{2.19}$$

We can now minimize the harmonic energy by steepest descent algorithm:

$$\frac{d\vec{f}(t)}{dt} = D\vec{f}^t \tag{2.20}$$

where $D\vec{f}^t$ is the absolute derivative that is defined as:

$$D\vec{f}^t = \Delta_{PL}\vec{f}^t - (\Delta_{PL}\vec{f}^t)^{\perp} \tag{2.21}$$

Using the algorithm, we can easily parameterize a genus zero surface conformally onto a unit sphere S^2.

In order to get a unique solution, we add the zero center of mass constraint to the minimization problem. Mathematically, the map $\vec{f} : S_1 \to S_2$ satisfies the zero center of mass constraint if and only if

$$\int_{S_1} \vec{f} dS_1 = 0 \tag{2.22}$$

In particular, all conformal maps from a surface S_1 to the sphere S^2 satisfying the zero center of mass constraint are unique up to the Euclidean rotation group.

To summarize, the computer algorithm for computing the conformal parameterization of the genus zero surface onto the sphere is as follow:

Algorithm 2.2.2.1 : Genus zero surface

Input : (mesh K of genus 0, step length δt, energy difference threshold δE),

Output :($f : C_2 \to S^2$), which minimizes E.

1. Given a Gauss map $I : C_2 \to S^2$. Let $f = I$, compute $E_0 = E_{new}(I)$

2. For each vertex $v \in K$, compute $D\vec{f}(v)$

3. Update $f(v)$ by $\delta f(v) = -D\vec{f}(v)\delta t$

4. Compute energy E_{new}

5. If $E_{new} - E_0 < \delta E$, return f. Otherwise, assign E to E_0. Repeat steps 2 to 5.

Figure 2.6 shows the conformal parameterizations of two different brain cortical surfaces onto the spheres. They are colored based on the mean curvature. Note that the geometry of the sulci are well preserved on the spherical domain, meaning that the conformal parameterization can preserve the local geometry effectively. After the brain is parameterized onto the sphere, spherical harmonic analysis can be done on the surface easily to study medical disease [29][30][31][32][33][34]

2.2.2 Computation of Conformal Parameterization of Higher Genus surface

Sometimes it is of great interest to parameterize a compact surface onto 2D rectangular domains. To parameterize a compact surface onto 2D rectangles, one intuitive technique is to cut it open along some suitable cutting boundaries. For example, a torus of genus one can be cut open and mapped to a rectangle along two cutting boundaries. Similarly, a torus of genus two can also be mapped to two rectangles by introducing suitable cut (See Figure 2.8). If the cut is suitably chosen, the parameterization could be conformal. In the algorithm that we use to parameterize the surface, we search for the suitable cutting boundaries on the surface in order to get a conformal map. This is done by computing the holomorphic one form on the surface. The holomorphic 1-form ω is a complex analytic differential form. A conformal parameterization from the surface onto the 2D

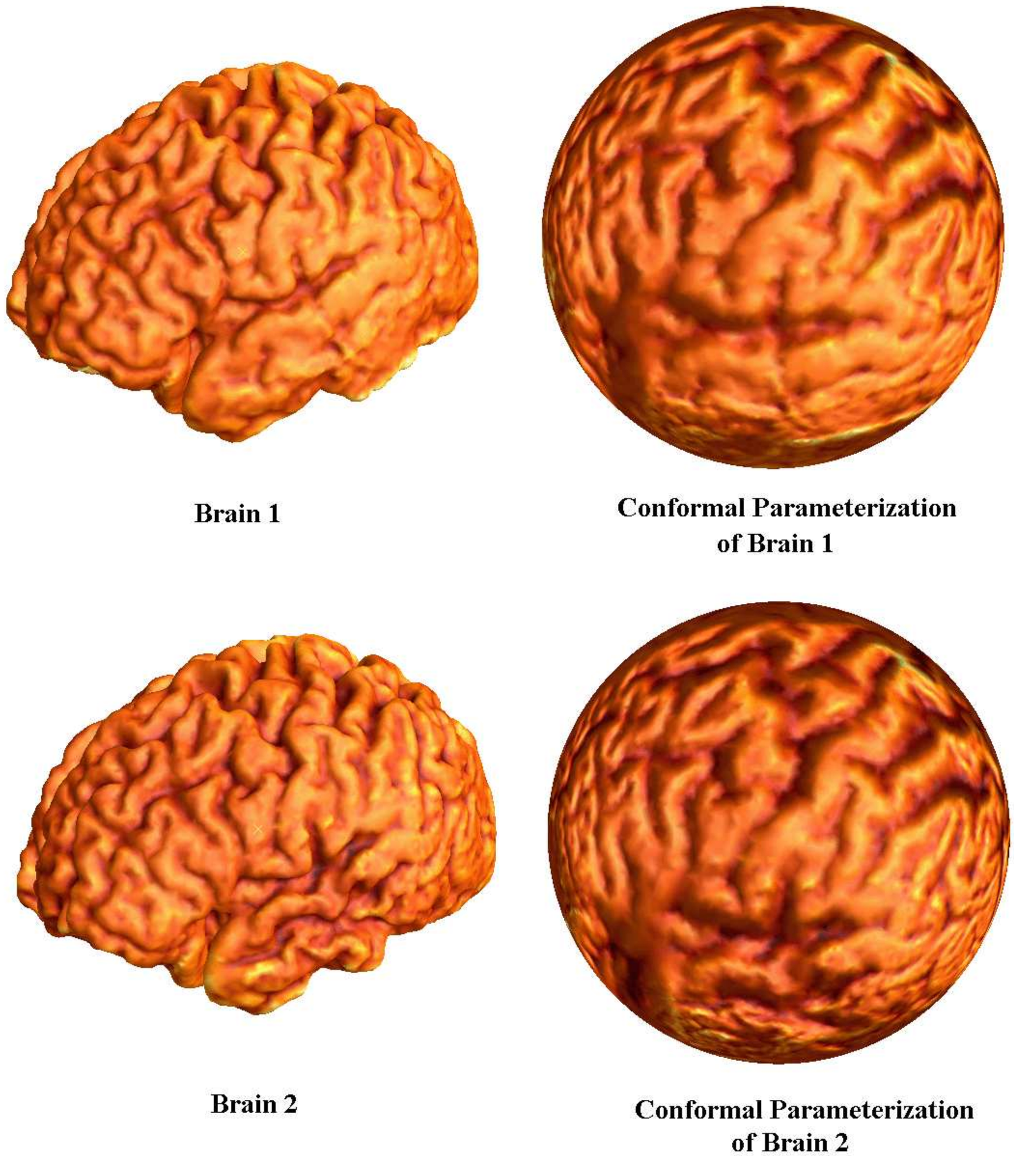

Figure 2.6: The top and bottom show the global conformal parameterization of Brain 1 and Brain 2 onto the spheres respectively. They are colored based on the mean curvature. Note that the geometry of the sulci are well preserved on the spherical domain, meaning that the conformal parameterization can preserve the local geometry effectively.

domain can be obtained by integrating the holomorphic one form [21][35][26][20].

To compute the holomorphic 1-form, we start by computing a harmonic 1-form ω on the surface. Similar to complex analysis, we can compute a harmonic conjugate $*\omega$ of ω, which is called the *Hodge star conjugate*, such that $W := \omega + i * \omega$ is a holomorphic (analytic) 1-form.

The basis of harmonic 1-form can be computed from the dual basis of the homology basis. All curves on a surface form a homology group. The homology basis is a set of non-constant closed curves (up to homotopic) on the surface that can be deformed to any closed curves on the surface by operations including replicating, merging and splitting. A surface can be cut along a homology basis (a cut graph) to a topological disk, which is called a *fundamental domain.* For example, Figure 2.7 shows the homology basis on different surfaces. (A) shows the homology basis $\{e_1, e_2\}$on a genus one torus. (B) shows the homology basis of a genus two surface, which consists of 4 cutting boundaries. (C) shows the homology basis of a genus four surface, which consists of 8 cutting boundaries. As we cut along the suitable cutting boundaries of the surface, we can map the surface onto the 2D rectangles.

We firstly explain the concept of homology and cohomology in a rigorous way. Let K be a simplicial complex whose topological realiation $|K|$ is homeomorphic to a compact 2-dimensional manifold. Suppose there is a piecewise linear embedding, $F : |K| \to R^3$. The pair (K, F) is called a triangular mesh and we denote it as M. Let $[v_0, v_1, ..., v_p]$ be the p-cells of K. The $p - chain$ is defined as a linear combination of $q - simplies$,

$$\sum_{[v_0,v_1,...,v_p]\in K} c_{[v_0,v_1,...,v_p]}[v_0, v_1, ..., v_p] \tag{2.23}$$

Denote the set of all p-chains by C_pK. We can define the boundary operator $\partial : C_pK \to C_{p-1}K$ by:

$$\partial[v_0, v_1, ..., v_p] = \sum_{i=0}^{p}[v_0, ..., v_{i-1}, v_{i+1}, ..., v_p] \tag{2.24}$$

We can define *chain complex* as $C_*K = \{C_pK, \partial_p\}_{p\geq 0}$ and *cochain complex* as $C^*K = \{C^pK, \delta^p\}_{p\geq 0}$, where $C^pK = Hom(C_pK; R)$ and $\delta^p\omega\sigma = \omega\partial_{p+1}\sigma$, $\omega \in C^pK$ and $\sigma \in C_{p+1}K$. Now, the *p-th homology group* is defined as:

$$H_pK = Z_pK/B_pK \tag{2.25}$$

where Z_pK is the kernel of ∂_p and B_p is the image of ∂_{p+1}. Similarly, the *p-th cohomology group* can be defined as:

$$H^pK = Z^pK/B^pK \tag{2.26}$$

where Z^pK is the kernel of δ^p and B_p is the image of δ^{p+1}.

Given a homology basis $\{e_1, ..., e_{2g}\}$ on the surface, we can compute a set (basis) of the harmonic 1-forms $\{\omega_1, ..., \omega_{2g}\}$ (cohomology). According to Hodge theory, given $2g$ real numbers $c_1, c_2, ..., c_{2g}$, there is a unique real gradient field ω which satisfies the following system of equations:

$$\begin{cases} d\omega = \sum_{i=1}^{3}\omega([u_{j-1}, u_j]) = 0, \forall[u_0, u_1, u_2] \in M, u_0 = u_3 & \text{(closedness);} \\ \triangle\omega = \sum_{[u,v]\in M}\omega([u, v]) = 0\forall[u, v] \in M & \text{(harmonicity);} \\ \int_{e_i}\omega = \sum_{i=1}^{n_i}\omega([u^i_{j-1}, u^i_j]) = \delta_{ij}\forall e_i = \sum_{j=1}^{n_i}[u^i_{j-1}, u^i_j], u^i_0 = u^i_{n_i} & \text{(conjugacy).} \end{cases} \tag{2.27}$$

where $[u_0, u_1, u_2]$ represents a face on M; $[u, v]$ represents an edge on M; $k_{uv} = \frac{1}{2}(cot\alpha + cot\beta)$ in which α, β are the angles against the edge $[u, v]$.

The equation $d\omega = 0$ indicates ω is closed, where d is the exterior differential operator. The equation $\Delta\omega = 0$ represents the harmonicity of ω, where Δ is the Laplacian-Beltrami operator. The equation $\int_{e_i} \omega = c_i,\ i = 1, 2, ..., 2g$ restricts the cohomology class of ω by the values of the integration along the homology basis e_i's. In order to get a basis of the conformal gradient fields, we choose $2g$ sets of $\{c_i\}$, where the jth set is $\{\delta^i_j\}$. It can be shown that the linear system of equations is of full rank.

After we have computed ω, we can compute the $*\omega$ by using the discrete Hodge star operator. Intuitively, the Hodge star operator $*\omega$ can be obtained by rotating ω about the normal $\vec{n}$ on the tangent plane at each point of the surface. Suppose $\{\omega_1, \omega_2, ..., \omega_{2g}\}$ are a set of basis of all the solution of the system 2.27. Therefore, we can represent $*\omega$ as a linear combination of ω_i's:

$$*\omega = \sum_{i=1}^{2g} \lambda_i \omega_i \tag{2.28}$$

We can solve for λ_i through a linear system by considering the relationship between the *wedge product* $\wedge$ and *star wedge product* $*\wedge$.

Given two 1-forms ω and τ, the wedge product on smooth surface S is defined as the following integration:

$$\int_S \omega \wedge \tau = \int_S \omega \times \tau \cdot \vec{n} dS \tag{2.29}$$

where $\vec{n}$ is the normal field on S. Suppose $\{d_0, d_1, d_2\}$ are the oriented edges of a triangle T, their lengths are $\{l_0, l_1, l_2\}$, and the area of T is s, then the discrete wedge product $\wedge$ is defined as:

$$\int_T \omega \wedge \tau = \frac{1}{6} \begin{vmatrix} \omega(d_0) & \omega(d_1) & \omega(d_2) \\ \tau(d_0) & \tau(d_1) & \tau(d_2) \\ 1 & 1 & 1 \end{vmatrix} \tag{2.30}$$

The star wedge product $*\wedge$ of ω and τ on smooth surface S is defined as follows:

$$\int_S \omega * \wedge \tau = \int_S \omega \wedge * \tau = \int_S \omega \times * \tau \cdot \vec{n} \tag{2.31}$$

The discrete star wedge product on mesh T is defined as

$$\int_T \omega * \wedge \tau = UMV^T, \tag{2.32}$$

where

$$M = \frac{1}{24s} \begin{pmatrix} -4l_0^2 & l_0^2 + l_1^2 - l_2^2 & l_0^2 + l_2^2 - l_1^2 \\ l_1^2 + l_0^2 - l_2^2 & -4l_1^2 & l_1^2 + l_2^2 - l_0^2 \\ l_2^2 + l_0^2 - l_1^2 & l_2^2 + l_1^2 - l_0^2 & -4l_2^2 \end{pmatrix} \tag{2.33}$$

and vectors U, V are

$$U = (\omega(d_0), \omega(d_1), \omega(d_2)); V = (\tau(d_0), \tau(d_1), \tau(d_2)) \tag{2.34}$$

Based on the formula:

$$\int_S \omega_i \wedge * \omega = \int_S \omega_i * \wedge \omega, i = 1, 2, ..., 2g, \tag{2.35}$$

we can expand each term with the discrete wedge product and discrete star wedge product to get the following linear system:

$$W\Lambda = B \tag{2.36}$$

where W has entries $w_i j = \sum_{T \in S} \int_T \omega_i \wedge \omega_j$, Λ has entries λ_i and B has entries $b_i = \sum_{T \in S} \int_T \omega_i * \wedge \omega$.

After we get the holomorphic 1-form, we can compute the conformal parameterization ϕ by integrating the one form: $\phi(p) = \int_\gamma \omega = \int_\gamma f(z_\alpha) dz_\alpha$, where γ is any path joining p to a fixed point c on the surface and $\omega = f(z_\alpha)dz_\alpha$.

Double covering techniques are applied to surfaces with boundaries to convert them to closed symmetric surfaces. Suppose surface S has boundaries, we construct a copy of S denoted as S'. We reverse the orientation of S' by changing the order of vertices of each face from $[u, v, w]$ to $[v, u, w]$. We then glue S and S' together along their boundaries. The resulting mesh is denoted as $\overline{S}$, and called the double covering of S. The double covering is closed and so we can apply the holomorphic segmentation algorithm to compute the conformal parameterization.

To summarize, the algorithm for computing the conformal parameterization of higher genus surfaces are as follow:

Algorithm 2.2.2.2 : Higher genus surface

1. Given a high genus surface, find the homology basis $\{\xi_1, ..., \xi_{2g}\}$ of its homology group.

2. Given the homology basis $\{\xi_1, ..., \xi_{2g}\}$, compute its dual basis $\{w_1, ..., w_{2g}\}$ which is called the cohomology basis.

3. Diffuse the cohomology basis elements to harmonic 1-forms. This can be done by solving the following simultaneous equations: (1) $dw = 0$ $(closedness)$

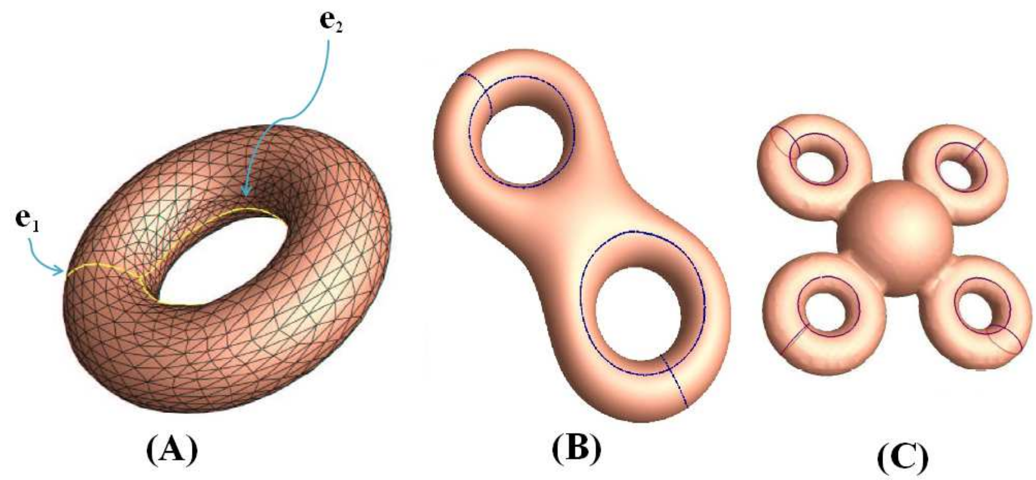

Figure 2.7: Homology basis (cutting boundaries) on different surfaces. (A) shows the homology basis $\{e_1, e_2\}$on a genus one torus. (B) shows the homology basis of a genus two surface, which consists of 4 cutting boundaries. (C) shows the homology basis of a genus four surface, which consists of 8 cutting boundaries.

(2) $\Delta w = 0$ (*harmonity*) (3) $\int_{\xi_i} w_j = \delta_{ij}$ (*duality*). The existence of solution is guaranteed by Hodge theory.

4. Compute the Hodge star conjugate $\{{}^*w_1, ..., {}^*w_{2g}\}$ of $\{w_1, ..., w_{2g}\}$

5. Integrate the holomorphic 1-form and get the conformal mapping: $f(x) = \int_\gamma w + i^*w$, where $w = \Sigma\lambda_i w_i$

This method for parameterizing surfaces onto 2D rectangular domains has been effectively used in medical research for disease analysis [36][37][38][39][1]

2.3 Geometric invariants on the Riemann Surface

Geometric invariants are quantities defined on the Riemann surface. They describe the geometric properties of the surface and are useful for distinguishing different surfaces. They are also useful for determining a surface. For exam-

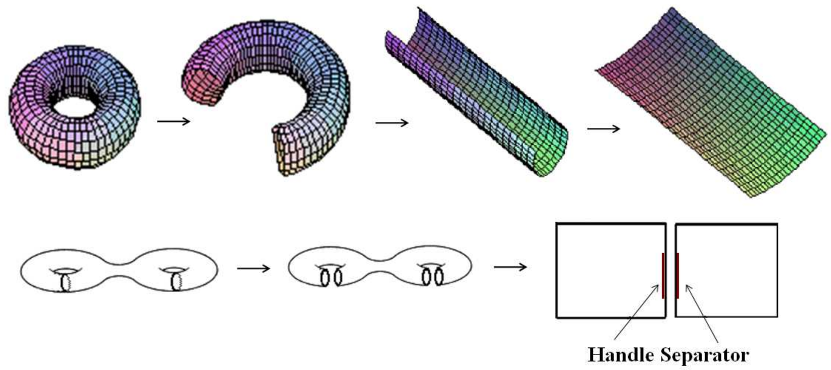

Figure 2.8: Illustration of how the conformal parameterization can be computed by introducing suitable cutting boundaries. The top shows how a genus one surface can be mapped to a 2D rectangles by cutting along the suitable cutting boundaries. The bottom shows how a genus two surface (2-torus) can be mapped to two rectangles.

ple, the mean curvature and surface normal can be used to reconstruct a surface uniquely up to a rigid motion. In this section, we describe the definition of several important geometric variants such as mean curvature, gaussian curvature, principal curvature, conformal factor and so on. We also describe briefly how these geometric variants can be computed.

An important geometric variant is the curvature. There are different types of curvature including principal curvatures, mean curvature and gaussian curvature. Intuitively, curvature is the amount by which a geometric object deviates from being flat.

For space curve, curvature is a value that measures how curved is the curve at a point on a curve. At any point P on the curve, there is a circle of right size, called the osculating circle, that touches P and fits the most. The flatter the curve at P, the larger is its osculating circle. The sharper the curve at P, the smaller is its osculating circle. Thus, we can define the value of curvature as $1/r$, where r is the radius of the osculating circle. When the osculating circle is large, the curvature $1/r$ is small. Mathematically, let $\gamma(s)$ be a regular parametric curve, where s is the arc length, or natural parameter. It determines the unit tangent vector T, the unit normal vector N, the curvature $\kappa(s)$, the signed curvature $k(s)$ and the radius of curvature r at each point:

$$T(s) = \gamma'(s),\ T'(s) = k(s)N(s),\ \kappa(s) = |\gamma''(s)| = |k(s)|,\ r(s) = \frac{1}{\kappa(s)} \tag{2.37}$$

The curvature of a straight line is identically zero. The curvature of a circle of radius R is constant, i.e. it does not depend on the point and is equal to the reciprocal of the radius:

$$\kappa = \frac{1}{R} \tag{2.38}$$

For a Riemann surface, consider the intersection of the surface with a plane containing the normal vector and one of the tangent vectors at a particular point. The intersection is a plane curve and has a curvature. This is the normal curvature, and it varies with the choice of the tangent vector. The maximum and minimum values of the normal curvature at a point are called the principal curvatures, k_1 and k_2, and the directions of the corresponding tangent vectors are called principal directions. The gaussian curvature K is defined as the product of the principal curvatures $K = k_1 k_2$. The mean curvature H is defined as the average of the principal curvatures $H = \frac{k_1+k_2}{2}$.

Mathematically, the curvatures can be computed from the second fundamental form. Consider the tangent plane $\mathrm{T}_p M$ of the surface M for each point $p \in M$. We have the surface normal $n(p)$, which varies smoothly with p. Then we have a map $n : M \to S^2$. It is called the normal map or Gauss map.

The second fundamental form is the tensor field $\mathcal{II}$ on M defined by $\mathcal{II}_p(\xi, \eta) = -\langle \mathrm{D}n_p(\xi), \eta, \xi, \eta \in \mathrm{T}_p M$ where $\langle , \rangle$ is the dot product of $\mathbb{R}^3$, and we consider the

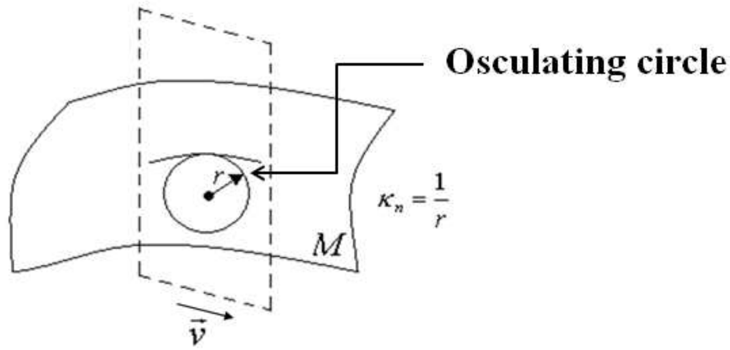

Figure 2.9: Illustration of how the normal curvature is defined. Consider the intersection of the surface with a plane containing the normal vector and one of the tangent vectors at a particular point. The intersection is a plane curve and has a curvature. This is the normal curvature, and it varies with the choice of the tangent vector.

tangent planes of surfaces in $\mathbb{R}^3$ to be subspaces of $\mathbb{R}^3$.

The linear transformation $\mathrm{D}n_p$ is in reality the tangent mapping $\mathrm{D}n_p\colon \mathrm{T}_pM \to \mathrm{T}_{n(p)}S^2$, but since $\mathrm{T}_{n(p)}S^2 = \mathrm{T}_pM$ by the definition of n, we prefer to think of $\mathrm{D}n_p$ as $\mathrm{D}n_p\colon \mathrm{T}_pM \to \mathrm{T}_pM$.

The tangent map $\mathrm{D}n$, is often called the Weingarten map.

We can compute the matrix representation W, called the Weingarten matrix, for $-\mathrm{D}n$ in u, v-coordinates. Now, the normal curvature κ_n of a Riemann surface in a given direction is the reciprocal of the radius of the circle that best approximates a normal slice of the surface in that direction, which varies in different directions. The Weingarten matrix satisfies:

$$\kappa_n = \mathbf{v}^T W \mathbf{v} = \mathbf{v}^T \begin{pmatrix} e & f \\ f & g \end{pmatrix} \mathbf{v} \tag{2.39}$$

for any tangent vector $\mathbf{v}$. Its eigenvalues and eigenvectors are called principal curvatures and principal directions respectively. The mean of the eigenvalues is the mean curvature. A point on the Riemann surface at which the Weingarten matrix has the same eigenvalues is called an *umbilic point*.

The mean curvature and gaussian curvature can be computed from the conformal factor [40][41]. Given the conformal parameterization of the surface, we can obtain a conformal factor function λ. By definition, the conformal parameterization has a simple Riemannian metric, namely,

$$g_{ij} = \begin{cases} \lambda & \text{if } i = j; \\ 0 & \text{if } i \neq j. \end{cases}$$

In other words, the four metric coefficients are reduced to one coefficient metric λ, called the conformal factor. With this property, surface differential operators can be expressed within the conformal coordinates with simple formulae. The expressions are similar to the usual Euclidean differential operators, except for a scalar multiplication of the conformal factor. The conformal factor at a point p on the surface S can be determined by computing the scaling factor of a small area around p under the parameterization $\phi : R^2 \rightarrow S$. Mathematically, $\lambda(p) = \frac{\mathbf{Area}(B_\epsilon(p))}{\mathbf{Area}(\phi^{-1}(\mathbf{B}_\epsilon(\mathbf{p})))}$, where $B_\epsilon(p)$ is an open ball around p of radius p. After we have computed the conformal factor, we can compute the mean curvature and gaussian curvature easily. This can be described by the following theorems.

Lemma 2.3.1 :

$$K = -[(\Gamma^2_{12})_u - (\Gamma^2_{11})_v + \Gamma^1_{12}\Gamma^2_{11} + \Gamma^2_{12}\Gamma^2_{12} - \Gamma^2_{11}\Gamma^2_{22} - \Gamma^1_{11}\Gamma^2_{12}]/E \qquad (2.40)$$

Lemma 2.3.2 :

Suppose ϕ is orthogonal ($F = 0$). The gaussian curvature K can be computed by:

$$K = -\frac{1}{2\sqrt{EG}}[(\frac{E_v}{\sqrt{EG}})_v + (\frac{G_u}{\sqrt{EG}})_u] \tag{2.41}$$

Proof :

With $F = 0$, $\Gamma_{12}^2 = \frac{G_u}{2G}$; $\Gamma_{11}^2 = -\frac{E_v}{2G}$; $\Gamma_{12}^1 = \frac{E_v}{2E}$; $\Gamma_{11}^1 = \frac{E_u}{2E}$; $\Gamma_{11}^2 = -\frac{E_u}{2E}$; $\Gamma_{22}^2 = \frac{E_u}{2E}$. Putting them into equation 2.40, we have:

$$\begin{aligned}
K &= -[(\frac{G_u}{2G})_u + (\frac{E_v}{2G})_v - \frac{E_v^2}{4EG} + \frac{G_u^2}{4G^2} + \frac{E_vG_v}{4G^2} - \frac{E_uG_u}{4EG}]/E \\
&= -[(\frac{G_{uu}}{2G} - \frac{G_u^2}{2G^2}) + (\frac{E_{vv}}{2G} - \frac{E_vG_v}{2G^2}) - \frac{E_v^2}{4EG} + \frac{G_u^2}{4G^2} + \frac{E_vG_v}{4G^2} - \frac{E_uG_u}{4EG}]/E \\
&= -[\frac{G_{uu}}{2EG} + \frac{E_{vv}}{2EG} - \frac{E_{vv}^2}{4E^2G} - \frac{G_u^2}{4EG^2}) - \frac{E_vG_v}{4EG^2} - \frac{E_uG_u}{4E^2G}] \\
&= -\frac{1}{2\sqrt{EG}}[(\frac{E_v}{\sqrt{EG}})_v + (\frac{G_u}{\sqrt{EG}})_u]
\end{aligned} \tag{2.42}$$

Theorem 2.3.1 :

Suppose ϕ is conformal with $E = G = \lambda$ and $F = 0$, where λ is the conformal factor. The gaussian curvature K can be computed by:

$$K = -\frac{1}{2\lambda}\Delta log\ \lambda \tag{2.43}$$

Proof :

Suppose ϕ is conformal and $\lambda = \lambda(u, v)$ is the conformal factor with respect to

ϕ. Put $E = G = \lambda$ into equation 2.41, we have:

$$\begin{aligned} K &= -\frac{1}{2\sqrt{\lambda^2}}[(\frac{\lambda_v}{\sqrt{\lambda^2}})_v + (\frac{\lambda_u}{\sqrt{\lambda^2}})_u] \\ &= -\frac{1}{2\lambda}[(\frac{\lambda_v}{\lambda})_v + (\frac{\lambda_u}{\lambda})_u] \\ &= -\frac{1}{2\lambda}\Delta log\ \lambda \end{aligned} \tag{2.44}$$

Theorem 2.3.2 :

Suppose ϕ is conformal with $E = G = \lambda$ and $F = 0$, where λ is the conformal factor. The mean curvature H can be computed by:

$$H = \frac{1}{2\lambda}\mathbf{sign}(\phi)|\Delta\phi| = \pm\frac{1}{2\lambda}|\phi_{uu} + \phi_{vv}| \tag{2.45}$$

where $\vec{N}$ is the (unit) surface normal, $\mathbf{sign}(\phi) = \frac{<\Delta\phi,\vec{N}>}{|\Delta\phi|} = \pm 1$.

Proof :

Suppose ϕ is conformal and $\lambda = \lambda(u, v)$ is the conformal factor with respect to ϕ.

We have $< \phi_u, \phi_u >=< \phi_v, \phi_v >= \lambda$ and $< \phi_u, \phi_v >= 0$. By differentiation, we have:

$$< \phi_{uu}, \phi_u >=< \phi_{vu}, \phi_v >= - < \phi_u, \phi_{vv} >$$

We get: $< \phi_{uu} + \phi_{vv}, \phi_u >= 0$. And similarly we get: $< \phi_{uu} + \phi_{vv}, \phi_v >= 0$. Therefore, $\Delta\phi$ is parallel to $\vec{N}$ and $\mathbf{sign}(\phi) = \frac{<\Delta\phi,\vec{N}>}{|\Delta\phi|} = \pm 1$.

Now,

$$H = \frac{1}{2}\frac{Eg - 2fF + Ge}{EG - F^2} = \frac{1}{2}\frac{g + e}{\lambda} = \frac{1}{2}\frac{< \phi_{uu} + \phi_{vv}, \vec{N} >}{\lambda}$$

So,

$$H = \frac{1}{2}\frac{< \Delta\phi, \vec{N} >}{\lambda} = \frac{1}{2}\frac{< \Delta\phi, \vec{N} >}{|\Delta\phi|\lambda}|\Delta\phi| = \frac{1}{2\lambda}\mathbf{sign}(\phi)|\Delta\phi|$$

Q.E.D.

Another important geometric variant on the surface is the geodesic curve. Let M be a Riemann surface with Levi-Civita connection ∇. The solution to the equation $\nabla_{\dot\gamma}\dot\gamma = 0$ defined in the interval $[0, a]$, is called a geodesic or a geodesic curve. When M is compact, the curve γ is the shortest possible curve between the points $\gamma(0)$ and $\gamma(a)$, and is often referred to as a minimizing geodesic between these points. Conversely, any curve which minimizes the distance between two arbitrary points in a manifold, is a geodesic. Therefore, on a compact Riemann surface M, we can regard a geodesic between two points to be the shortest path joining the two points.

We can compute a smooth approximation of the geodesic on the spline (smooth) mesh using the conformal parameterization. This can be described by the following theorem.

Theorem 2.3.3 :

Let S be a Riemann surface. Suppose ϕ is the conformal parameterization of S with conformal factor λ. Then the geodesic between $\phi(p)$ and $\phi(q)$ on S can be computed on the 2D parameter domain by minimizing the following energy:

$$E(\vec{c}(t)) = \int_0^1 \lambda(\vec{c}(t))||\vec{c}\,'(t)||^2 dt \tag{2.46}$$

where $\vec{c}(0) = p$ and $\vec{c}(0) = q$.

The geodesic on S will be $\phi(\vec{c}(t))$.

The energy can be minimized iteratively by:

$$\frac{\vec{c}_{n+1}(t) - \vec{c}_n(t)}{dt} = \beta(t)[-||\vec{c}_n'(t)||^2 \nabla\lambda(\vec{c}_n(t)) + (\lambda(\vec{c}_n(t))\vec{c}_n'(t))'] \tag{2.47}$$

where $\beta(t) = e^2 e^{-\frac{1}{||t-\frac{1}{2}|-\frac{1}{2}|}}$. The multiplication of $\beta(t)$ is to make sure that the curve is evolved with the end points fixed.

Proof :

Let $\vec{\alpha} : [0,1] \to S$ be any curve on S. By Cauchy-Schwartz inequality,

$$\begin{aligned} L(\vec{\alpha})^2 &= (\int_0^1 |\vec{\alpha}'(t)|dt)^2 \\ &= (\int_0^1 1 \cdot |\vec{\alpha}'(t)|dt)^2 \\ &\leq (\int_0^1 1dt)^2 (\int_0^1 |\vec{\alpha}'(t)|^2 dt) := E_S(\vec{\alpha}) \end{aligned}$$

So, $L(\vec{\alpha})^2 \leq E_S(\vec{\alpha})$.

Let $\vec{\gamma} : [0,1] \to D$ be the projection of a minimizing geodesic curve on S onto D. We have:

$$\frac{D\vec{\gamma}'}{dt} = 0 \Rightarrow <\vec{\gamma}'', \vec{\gamma}'>= 0$$

Thus, $<\vec{\gamma}', \vec{\gamma}'>= k$ for some constant k.

Now, $L(\vec{\gamma})^2 = (\int_0^1 |\vec{\alpha}'(t)|dt)^2 = k = E(\vec{\gamma})$ and so $E(\vec{\gamma}) = L(\vec{\gamma})^2 \leq L(\vec{\alpha})^2 \leq E(\vec{\alpha})$.

As a result, let $\vec{c} : [0,1] \to D$ be any curve on the parameter domain D and $\vec{\Upsilon} : [0,1] \to D$ be the projection of $\vec{\gamma}$ onto the parameter domain, we have: $E(\vec{c}) = E_S(\phi(\vec{c})) \leq E_S(\phi(\vec{\Upsilon})) = E_S(\vec{\Upsilon})$.

Now, let $\vec{w}(t) = \beta(t)[-||\vec{c}'(t)||^2 \nabla\lambda(\vec{c}(t)) + (\lambda(\vec{c}(t))\vec{c}'(t))']$. Consider:

$$\begin{aligned}
\frac{d}{ds}|_{s=0} E(\vec{c}(t) + s\vec{w}(t)) &= \frac{d}{ds}|_{s=0} \int_0^1 \lambda(\vec{c}(t) + s\vec{w}(t))||\vec{c}'(t) + s\vec{w}'(t)||^2 dt \\
&= \int_0^1 ||\vec{c}'(t)||^2 \nabla\lambda(\vec{c}(t)) \cdot \vec{w}(t) + (\lambda(\vec{c}(t))\vec{c}'(t)) \cdot \vec{w}'(t) dt \\
&= \int_0^1 [||\vec{c}'(t)||^2 \nabla\lambda(\vec{c}(t)) - (\lambda(\vec{c}(t))\vec{c}'(t))'] \cdot \vec{w}(t) dt \\
&= -\int_0^1 || \ \ ||\vec{c}'(t)||^2 \nabla\lambda(\vec{c}(t)) - (\lambda(\vec{c}(t))\vec{c}'(t))'||^2 dt < 0
\end{aligned}$$

Thus, the energy can be minimized iteratively by:

$$\frac{\vec{c}_{n+1}(t) - \vec{c}_n(t)}{dt} = \beta(t)[-||\vec{c}_n'(t)||^2 \nabla\lambda(\vec{c}_n(t)) + (\lambda(\vec{c}_n(t))\vec{c}_n'(t))'] \tag{2.48}$$

where $\beta(t) = e^2 e^{-\frac{1}{||t-\frac{1}{2}|-\frac{1}{2}|}}$.

Q.E.D.

CHAPTER 3

Optimized Brain Conformal Parameterization and Its Application to Human Brain Mapping

3.1 Introduction

Rapid development of computer technology has accelerated the acquisition and databasing of brain data. An effective way to analyze and compare brain data from multiple subjects is to map them into a canonical space while retaining the original geometric information as far as possible. Surface-based approaches often map cortical surface data to a parameter domain such as a sphere, providing a common coordinate system for data integration [28, 42]. One method to do this is to conformally map cortical surfaces to the sphere. It is well known that any genus zero Riemann surface can be mapped conformally to a sphere. Cortical surface is a genus zero surface. Therefore, conformal mapping offers a convenient method to parameterize cortical surfaces without angular distortion, generating an orthogonal grid on the cortex that locally preserves the metric. Although conformal mapping preserves the local geometry well, the important anatomical features, such as the sulci landmarks, are usually not aligned consistently. To compare cortical surfaces more effectively, it is advantageous to adjust the conformal parameterizations to match consistent anatomical features across subjects [43][44]. Here we refer to these anatomical features as landmarks. Some examples of landmarks are shown in Figure 3.1. This matching of cortical patterns improves the alignment of data across subjects, although it is more challenging to create a consistent conformal (orthogonal) parameterization of anatomy across subjects when landmarks are constrained to lie at specific locations in the spherical parameter space. Here we describe and compare two methods to accomplish the task. The first approach is based on pursuing an optimal Möbius transformation to minimize the landmark mismatch error. The second approach is based on a new energy functional, to optimize the conformal parameterization of cortical surfaces by using landmarks. Experimental results on a dataset of 40 brain hemispheres showed that the landmark mismatch energy can be significantly reduced while effectively preserving conformality. The key advantage of these conformal parameterization approaches is that any local adjustments of the mapping to match landmarks do not affect the conformality of the mapping significantly. A detailed comparison between the two approaches will be discussed. The first approach can generate a map which is exactly conformal, although the landmark mismatch error is not reduced as effective as the second approach. The second approach can generate a map which significantly reduces the landmark mismatch error, but some conformality will be lost [45][46][47].

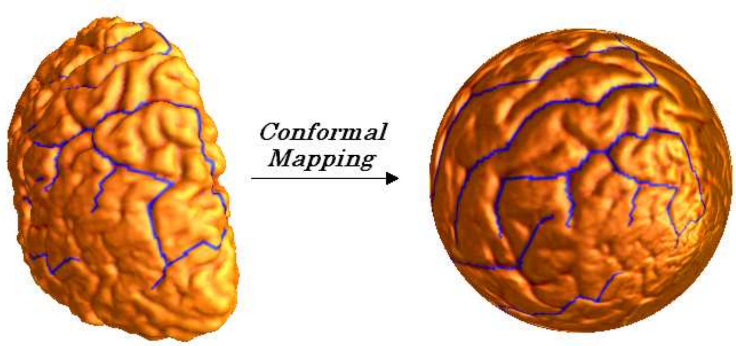

Figure 3.1: Manually labeled landmarks on the brain surface. The original surface is on the left. Its conformal mapping result to a sphere is on the right.

3.2 Previous works

Optimization of surface diffeomorphisms by landmark matching has been studied intensively. Joan et al. [48] proposed to generate large deformation diffeomorphisms of the sphere onto itself, given the displacements of a finite set of template landmarks. The diffeomorphism obtained can match the geometric features significantly but it is, in general, not a conformal mapping. Leow et al. [49] proposed a level set based approach for matching different types of features, including points and 2D or 3D curves represented as implicit functions. Cortical surfaces were flattened to the unit square. Nine sulcal curves were chosen and were represented by the intersection of two level set functions, and used to constrain the warp of one cortical surface onto another. The resulting transformation was interpolated using a large deformation momentum formulation in the cortical parameter space, generalizing an elastic approach for cortical matching developed in Thompson et al. [50]. Duygu et al. [51] proposed a more automated mapping technique that results in good sulcal alignment across subjects, by combining parametric relaxation, iterated closest point registration and inverse stereographic projection. Gu et al. [19] proposed to optimize the conformal parametrization by composing an optimal Möbius transformation so that it minimizes the landmark mismatch energy. The resulting parameterization remains conformal. In this chapter, we are going to compare this method with a variational approach that gives an optimized brain conformal parameterization.

3.3 Optimization of Brain Conformal Parametrization

In this section, we describe two methods to adjust conformal parameterizations of the cortical surface so that they match consistent anatomical features across subjects. This matching of cortical patterns improves the alignment of data across subjects, e.g., when integrating functional imaging data across subjects, measuring brain changes, or making statistical comparisons in cortical anatomy [52].

3.3.1 Optimal Möbius Transformation

In this approach, the brain conformal parametrization is improved by compositing it with an optimal Möbius transformation which reduces the landmark mismatch error.

By definition, a *Möbius transformation* is a bijective conformal map of the extended complex plane $\widehat{\mathbb{C}} = \mathbb{C} \cup \infty$ (i.e. the complex plane augmented by the point at infinity) of the form:

$$f(z) = \frac{az + b}{cz + d} \tag{3.1}$$

where z, a, b, c, d are complex numbers satisfying $ad - bc \neq 0$. It can be usefully expressed as a matrix $\mathfrak{H}$:

$$\mathfrak{H} = \begin{pmatrix} a & b \\ c & d \end{pmatrix} \tag{3.2}$$

The condition $ad - bc \neq 0$ is equivalent to the condition that the determinant of above matrix be nonzero (i.e. the matrix should be non-singular). Note that multiplying $\mathfrak{H}$ by any complex number λ gives rise to the same transformation. Such matrix representations are called *projective representations*. It is often convenient to normalize $\mathfrak{H}$ so that its determinant is equal to 1. The matrix $\mathfrak{H}$ is then unique up to sign. To preserve the orientation, we can assume $ad - bc = 1$.

The set of all *Möbius transformation* forms a group, called the *Möbius trans-*

formation group. The *Möbius transformation* can be regarded as a bijective conformal diffeomorphism of the sphere $\mathbb{S}^2$ using the sterographic transformation. A sterographic projection $\varsigma : \mathbb{S}^2 \to \widehat{\mathbb{C}}$ is a bijective map between the sphere $\mathbb{S}^2$ and the extended complex plane $\widehat{\mathbb{C}}$. Therefore, a *Möbius transformation* $f : \widehat{\mathbb{C}} \to \widehat{\mathbb{C}}$can be regarded as a bijective conformal diffeomorphism $\tilde{f} : \mathbb{S}^2 \to \mathbb{S}^2$ of the sphere $\mathbb{S}^2$ by the following:

$$\tilde{f} = \varsigma^{-1} \circ f \circ \varsigma \tag{3.3}$$

We define an energy to measure the quality of the parameterization. Suppose two brain surfaces S_1, S_2 are given, conformal parameterizations are denoted as $f_1 : \mathbb{S}^2 \to S_1$ and $f_2 : \mathbb{S}^2 \to S_2$, we can define the matching energy as:

$$E(f_1, f_2) = \int_{\mathbb{S}^2} ||f_1(u, v) - f_2(u, v)||^2 dudv \tag{3.4}$$

We can compose an optimal Möbius transformation τ with f_2 which minimizes the landmark matching energy. That is,

$$E(f_1, f_2 \circ \tau) = min_{\zeta \in \Omega} E(f_1, f_2 \circ \zeta)) \tag{3.5}$$

In order to match the important geometric features on the brains, landmarks are commonly used. Suppose the landmarks are represented as discrete point sets and denoted as $\{p_i \in S_1\}$ and $\{q_i \in S_2\}$, p_i matches q_i, $i = 1, 2, ..., n$. The landmark mismatch functionl for $u \in \Omega$ is as follow:

$$E(u) = \sum_{i=1}^{n} ||f_1^{-1}(p_i) - u(f_2^{-1}(q_i))||^2, u \in \Omega, p_i \in S_1, q_i \in S_2 \tag{3.6}$$

We next convert the nonlinear variational problem into a least square problem. We project the sphere to the complex plane, then the Mӧbius transformation is represented as a complex linear rational formula. If we assume u maps infinity to infinity, then u can be represented in a linear form as $u = az + b$. Then $E(u)$ can be simplified as:

$$E(u) = \sum_{i=1}^{n} g(z_i)|az_i + b - \tau_i|^2 \tag{3.7}$$

where z_i is the stereographic projection of q_i, τ_i is the projection of p_i, g the conformal factor from the plane to the sphere which can be simplified as:

$$g(z) = 4/(1 + |z|^2) \tag{3.8}$$

The problem becomes a least squares problem. The solution $(a, b) \in \mathbb{C}^2$ of u can be solved easily by the following linear system:

$$\begin{pmatrix} \sum_{i=1}^{n} g(z_i)z_i^2 & \sum_{i=1}^{n} g(z_i)z_i \\ \sum_{i=1}^{n} g(z_i)z_i & \sum_{i=1}^{n} g(z_i) \end{pmatrix} \begin{pmatrix} a \\ b \end{pmatrix} = \begin{pmatrix} \sum_{i=1}^{n} g(z_i)z_i\tau_i \\ \sum_{i=1}^{n} g(z_i)\tau_i \end{pmatrix} \tag{3.9}$$

This algorithm allows us to produce an optimal map that preserves exactly the conformality. However, since this method minimizes the energy with respect to the six degree of freedom of the Mӧbius transformation group, the minimization of the landmark mismatch error is not as effective as our second approach, the variational approach, which will be discussed in the next section.

3.3.2 Variational approach

The second method, which is based on a new energy functional, optimizes the conformal parameterization of cortical surfaces by using landmarks. This is done by minimizing the compound energy functional $E_{new} = E_{harmonic} + \lambda E_{landmark}$, where $E_{harmonic}$ is the harmonic energy of the parameterization and $E_{landmark}$ is the landmark mismatch energy. We prove theoretically that our proposed E_{new} is guaranteed to be decreasing and studied the rate of changes of $E_{harmonic}$ and $E_{landmark}$. Experimental results show that our algorithm can considerably reduce the landmark mismatch energy while effectively retaining the conformality property. Based on these findings, we argue that the conformal mapping provides an attractive framework to help analyze anatomical shape, and to statistically combine or compare 3D anatomical models across subjects.

The proposed algorithm is a variational approach that optimizes the conformal parameterization using discrete landmarks. This algorithm optimizes the landmark mismatch energy over all degrees of freedom in the reparameterization group. The map obtained can considerably reduce the landmark mismatch energy while retaining conformality as far as possible.

Suppose C_1 and C_2 are two cortical surfaces we want to compare. We let $f_1 : C_1 \to S^2$ be the conformal parameterization of C_1 mapping it onto S^2. We manually label the landmarks on the two cortical surfaces as discrete point sets, as shown in Figure 3.1. We denote them as $\{p_i \in C_1\}$, $\{q_i \in C_2\}$, with p_i matching q_i. We proceed to compute a map $f_2 : C_2 \to S^2$ from C_2 to S^2, which minimizes the harmonic energy as well as minimizing the so-called landmark mismatch energy. The landmark mismatch energy measures the Euclidean distance between the corresponding landmarks. Note that it makes sense to use Euclidean distance instead of geodesic distance. On $\mathbb{S}^2$, all the geodesic curves move along the great circle. As the Euclidean distance decreases, the geodesic distance will also decrease. In other words, the computed map should effectively preserve the conformal property and match the geometric features on the original structures as far as possible.

Let $h : C_2 \rightarrow S^2$ be any homeomorphism from C_2 onto S^2. We define the landmark mismatch energy of h as, $E_{landmark}(h) = 1/2 \sum_{i=1}^{n} ||h(q_i)) - f_1(p_i)||^2$. where the norm represents distance on the sphere. By minimizing this energy functional, the Euclidean distance between the corresponding landmarks on the sphere is minimized.

To optimize the conformal parameterization, we propose to find $f_2 : C_2 \rightarrow S^2$ which minimizes the following new energy functional (instead of the harmonic energy functional), $E_{new}(f_2) = E_{harmonic}(f_2)+\lambda E_{landmark}(f_2)$, where λ is a weighting factor (Lagrange multiplier) that balances the two penalty functionals. It controls how much landmark mismatch we want to tolerate. When $\lambda = 0$, the new energy functional is just the harmonic energy. When λ is large, the landmark mismatch energy can be significantly reduced. But more conformality will be lost (here we regard deviations from conformality to be quantified by the harmonic energy).

Now, let K represent the simplicial realization (triangulation) of the brain surface C_2, let u, v denote the vertices, and $[u, v]$ denote the edge spanned by u, v. Our new energy functional can be written as:

$$
\begin{aligned}
E_{new}(f_2) &= \frac{1}{2}\sum_{[u,v]\in K} k_{u,v}||f_2(u) - f_2(v)||^2 + \frac{\lambda}{2}\sum_{i=1}^{n} ||f_2(q_i) - f_1(p_i)||^2 \\
&= \frac{1}{2}\sum_{[u,v]\in K} k_{u,v}||f_2(u) - f_2(v)||^2 + \frac{\lambda}{2}\sum_{u\in K} ||f_2(u) - L(u))||^2 \chi_M(u)
\end{aligned}
$$

where $M = \{q_1, ..., q_n\}$; $L(q_i) = p_i$ if $u = q_i \in M$ and $L(u) = (1, 0, 0)$ otherwise. The first part of the energy functional is defined as in [**?**]. Note that by minimizing this energy, we may give up some conformality but the landmark mismatch energy is progressively reduced.

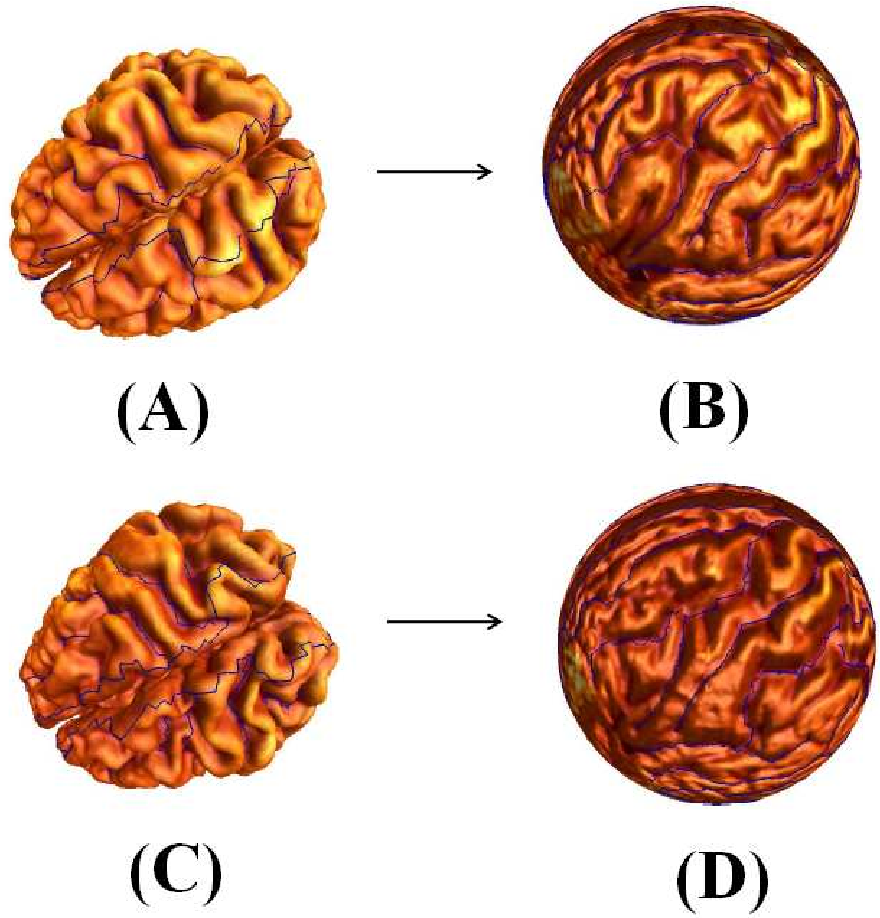

Figure 3.2: Mӧbius transformation to minimize the landmark mismatch error. The blue curve represented the important landmarks. Note that the alignment of sulci landmarks is quite consistent.

3.3.3 Optimization of Combined Energy

We next formulate a technique to optimize our energy functional. Suppose we would like to compute a mapping f_2 that minimizes the energy $E_{new}(f_2)$. This can be solved easily by steepest descent.

Definition 3.2.3.1 : Suppose $f \in C^{PL}$, where C^{PL} represent a vector space consists of all piecewise linear functions defined on K. We define the Laplacian as follows: $\Delta f(u) = \sum_{[u,v]\in K} k_{u,v}(f(u) - f(v)) + \lambda \sum_{u\in K}(f_2(u) - L(u))\chi_M(u)$.

Definition 3.2.3.2 : Suppose $\overrightarrow{f} \in C^{PL}$, $\overrightarrow{f} = (f_0, f_1, f_2)$, where the f_i are piecewise linear. Define the Laplacian of $\overrightarrow{f}$ as $\Delta\overrightarrow{f} = (\Delta f_0(u), \Delta f_1(u), \Delta f_2(u))$.

Now, we know that $f_2 = (f_{20}, f_{21}, f_{22})$ minimizes $E_{new}(f_2)$ if and only if the tangential component of $\Delta f_2(u)$= $(\Delta f_{20}(u), \Delta f_{21}(u), \Delta f_{22}(u))$ vanishes. That is $\Delta(f_2) = \Delta(f_2)^{\perp}$.

In other words, we should have $P_{\overrightarrow{n}}\Delta f_2(u) = \Delta f_2(u) - (\Delta f_2(u) \cdot \overrightarrow{n})\overrightarrow{n} = 0$. We use a steepest descent algorithm to compute $f_2 : C_2 \to S^2$: $\frac{df_2}{dt} = -P_{\overrightarrow{n}}\Delta f_2(t)$.

Algorithm to Optimize the Combined Energy $\mathbf{E_{new}}$

Input : (mesh K, step length δt, energy difference threshold δE),

Output :($f_2 : C_2 \to S^2$), which minimizes E.

1. Given a Gauss map $I : C_2 \to S^2$. Let $f_2 = I$, compute $E_0 = E_{new}(I)$
2. For each vertex $v \in K$, compute $P_{\overrightarrow{n}}\Delta f_2(v)$
3. Update $f_2(v)$ by $\delta f_2(v) = -P_{\overrightarrow{n}}\Delta f_2(v)\delta t$
4. Compute energy E_{new}
5. If $E_{new} - E_0 < \delta E$, return f_2. Otherwise, assign E to E_0. Repeat steps 2 to 5.

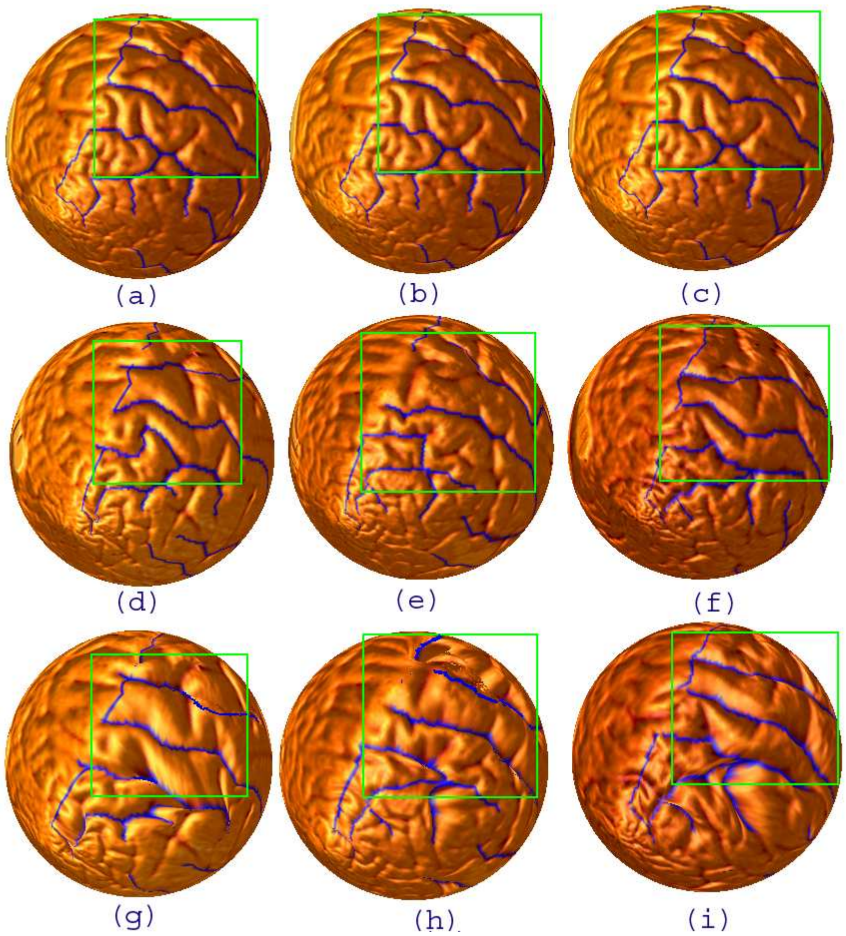

Figure 3.3: In (a), the cortical surface C_1 (the control) is mapped conformally ($\lambda = 0$) to the sphere. In (d), another cortical surface C_2 is mapped conformally to the sphere. Note that the sulcal landmarks appear very different from those in (a) (see landmarks in the green square). In (g), the cortical surface C_2 is mapped to the sphere using our algorithm (with $\lambda = 3$). Note that the landmarks now closely resemble those in (a) (see landmarks in the green square). (b) and (c) shows the same cortical surface (the control) as in (a). In (e) and (f), two other cortical surfaces are mapped to the spheres. The landmarks again appears very differently. In (h) and (i), the cortical surfaces are mapped to the spheres using our algorithm. The landmarks now closely resemble those of the control.

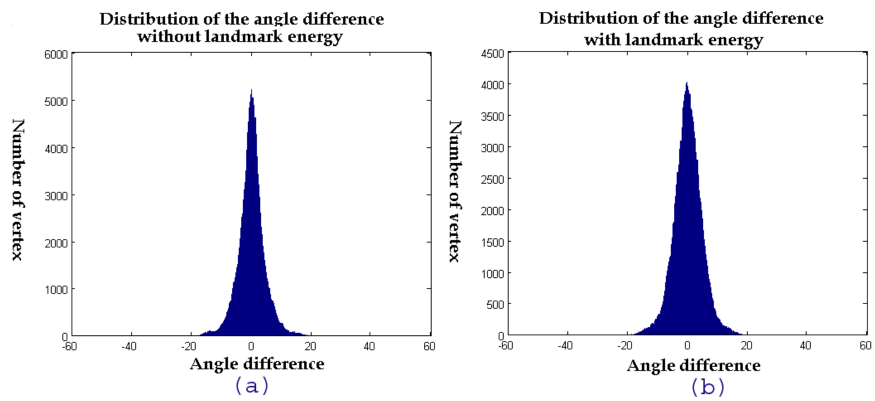

Figure 3.4: Histogram (a) shows the statistics of the angle difference using the conformal mapping. Histogram (b) shows the statistic of the angle difference using our algorithm ($\lambda = 3$). It is observed that the angle is significantly preserved.

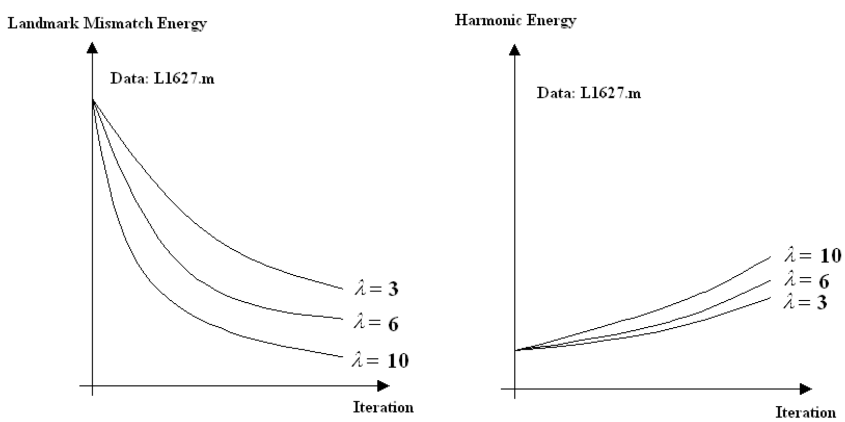

Figure 3.5: Diagram that shows how the harmonic energy and landmark mismatch energy change at each iteration. The left shows how the landmark mismatch energy changes. The right shows how the harmonic energy changes.

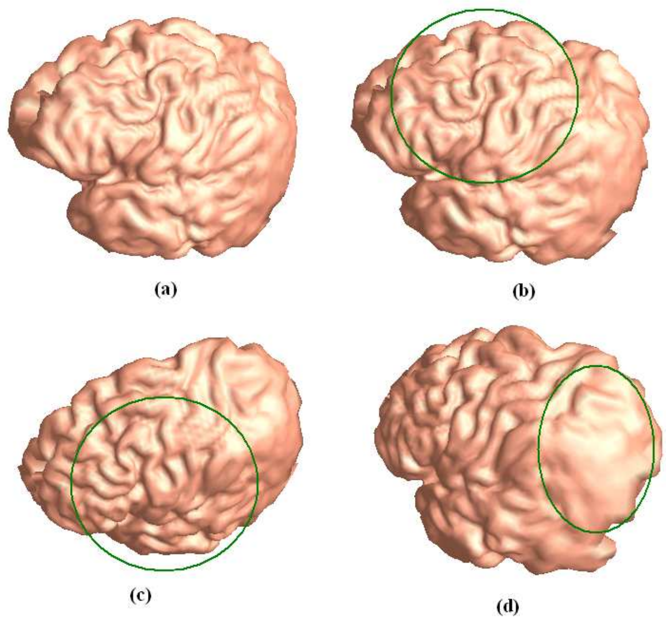

Figure 3.6: The average map of the optimized conformal parametrization using the variational approach. 40 landmarks are manually labelled. Observed that the important sulci landmarks are clearly shown. It means that the landmarks are consistently aligned

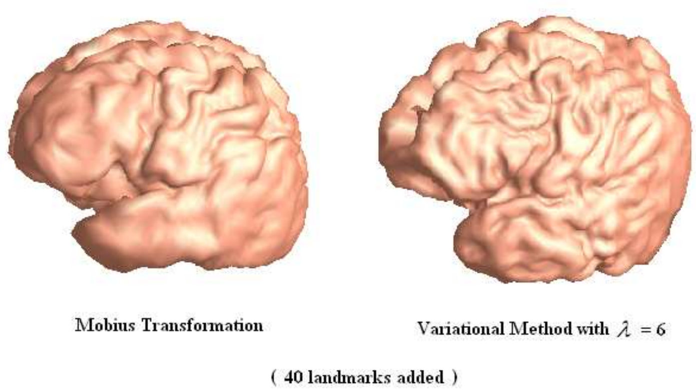

Figure 3.7: The average map of the optimized conformal parametrization by the two different approaches.

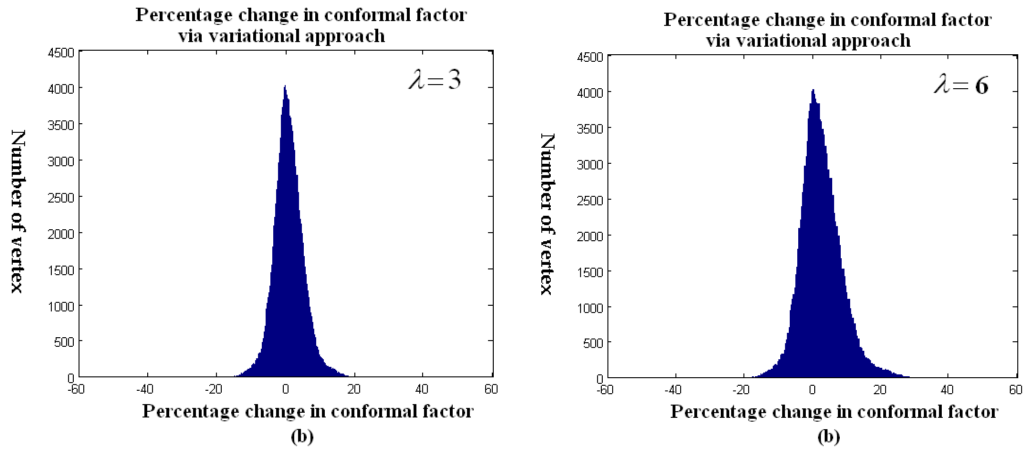

Figure 3.8: Histogram showing the percentage change in the conformal factor with different algorithm. The left shows the percentage change in the conformal factor using the variational approach with $\lambda = 3$. The right shows the percentage change in the conformal factor using the variational approach with $\lambda = 6$. Note that the conformality is well preserved. However, more conformality will be lost with larger λ.

3.4 Experimental Results

In our experiment, we tested our algorithm on a set of left hemisphere cortical surfaces generated from brain MRI scans of 40 healthy adult subjects, aged 27.5+/-7.4SD years (16 males, 24 females), scanned at 1.5 T (on a GE Signa scanner). Data and cortical surface landmarks were those generated in a prior paper, Thompson et al. [52] where the extraction and sulcal landmarking procedures are fully detailed. Using this set of 40 hemispheric surfaces, we mapped all surfaces conformally to the sphere and optimized the conformal map by the two approaches. In our first approach, we optimized the conformal map by composing it with an optimal Möbius transformation, which reduced the landmark mismatch error. Note that the optimized maps we get remains exactly conformal. Figure 3.2 shows some of our experimental result. Note that the alignment of sulci landmarks are quite consistent after optimizing the map with the optimal

Mӧbius transformation.

In our second approach, we mapped the cortical surfaces conformally to the sphere and minimized the compound energy matching all subjects to a randomly selected individual subject (alternatively, the surfaces could have been aligned to an average template of curves on the sphere). An important advantage of this approach is that the local adjustments of the mapping to match landmarks do not greatly affect the conformality of the mapping. In Figure 3.3(a), the cortical surface C_1 (a control subject) is mapped conformally ($\lambda = 0$) to the sphere. In (b), another cortical surface C_2 is mapped conformally to the sphere. Note that the sulcal landmarks appear very different from those in (a) (see landmarks in the green square). This means that the geometric features are not well aligned on the sphere unless a further feature-based deformation is applied. In Figure 3.3(c), we map the cortical surface C_2 to the sphere with our algorithm, while minimizing the compound energy. This time, the landmarks closely resemble those in (a) (see landmarks in the green square).

In Figure 3.4, statistics of the angle difference are illustrated. Note that under a conformal mapping, angles between edges on the initial cortical surface should be preserved when these edges are mapped to the sphere. Any differences in angles can be evaluated to determine departures from conformality. Figure 3.4(a) shows the histogram of the angle difference using the conformal mapping, i.e. after running the algorithm using the conformal energy term only. Figure 3.3(b) shows the histogram of the angle difference using the compound functional that also penalizes landmark mismatch. Despite the fact that inclusion of landmarks requires more complex mappings, the angular relationships between edges on the source surface and their images on the sphere are clearly well preserved even after landmark constraints are enforced.

In Figure 3.8, statistic of the percentage change in the conformal factor are illustrated. The left shows the percentage change in the conformal factor using the variational approach with $\lambda = 3$. The right shows the percentage change in the conformal factor using the variational approach with $\lambda = 6$. Note that the conformality is well preserved. However, more percentage change in conformality is observed with larger λ.

	$\lambda = 3$	$\lambda = 6$	$\lambda = 10$
$E_{harmonic}$ of the initial (conformal) parameterization:	100.6	100.6	100.6
$\lambda E_{landmark}$ of the initial (conformal) parameterization:	81.2	162.4	270.7
Initial compound energy ($E_{harmonic} + \lambda E_{landmark}$) :	181.8	263.0	371.3
Final $E_{harmonic}$	109.1 ($\nearrow$ 8.45%)	111.9 ($\nearrow$ 11.2%)	123.0 ($\nearrow$ 22.2%)
Final $\lambda E_{landmark}$	11.2 ($\searrow$ 86.2%)	13.7 ($\searrow$ 91.6%)	15.6($\searrow$ 95.8%)
Final compound energy ($E_{harmonic} + \lambda E_{landmark}$)	120.3 ($\searrow$ 33.8%)	125.6($\searrow$ 52.2%)	138.6 ($\searrow$ 62.7%)

Table 3.1: Numerical data from our experiment. The landmark mismatch energy is significantly reduced while the harmonic energy is only slightly increased. The table also illustrates how the results differ with different values of λ. The landmark mismatch error can be reduced by increasing λ, but conformality will increasingly be lost.

We also tested with other parameter λ with different values. Table 3.1 shows numerical data from the experiment. From the Table, we observe that the landmark mismatch energy is significantly reduced while the harmonic energy is only slightly increased. The table also illustrates how the results differ with different values of λ. We observe that the landmark mismatch error can be reduced by increasing λ, but conformality is increasingly lost. Figure 3.5 shows how the harmonic energy and landmark energy change in each iterations with different values of λ. Again, more landmark mismatch error can be reduced with larger λ, but more harmonic energy (the conformality) is lost.

To visualize how well the alignment of the important sulci landmarks is, we took average of the 15 optimized maps using the variational method. Figure 3.6 shows average maps at different angles. In (b) and (c), sulci landmarks are clearly preserved inside the green circle where landmarks are manually labelled. In (d), the sulci landmarks are averaged out inside the green circle where no landmarks are manually labelled. It means that our algorithm can significantly improve the alignment of the anatomical features.

Note that our first algorithm is different from the second one in that the first method can generate an optimized map which remains exactly conformal, although the reduction in the landmark mismatch error is not as effective as the second approach. Table 3.2 shows the numerical data of our experiment. From the Table, we observe that the variational method can reduce the landmark mismatch error more effectively than the optimal Mӧbius transformation approach. It is also observed that more landmark mismatch can be reduced by larger value of λ. Figure 3.7 shows the average maps of the optimized conformal maps we got by the two different approaches. Figure 3.7(a) shows the average maps of the optimal Mӧbius transformation approach. Figure 3.7 (b) shows the average map of the variational approach. Note that the sulci landmarks are better preserved using the variational approach.

3.5 Conclusion

In conclusion, we have described two algorithms to compute a map from the cortical surface of the brain to a sphere, which can effectively retain the original geometry by minimizing the landmark mismatch error across different subjects. The first method, which is based on the optimal Mӧbius transformation, can generate an optimal map that is exactly conformal. However, the landmark mis-

	Möbius Transformation	Variational $\lambda = 3$	Variational $\lambda = 6$
$E_{landmark}$ of the initial (conformal) parameterization:	160.33	160.33	160.33
$E_{landmark}$ of the final (optimized) parameterization:	73.75	19.24	9.62

Table 3.2: Numerical data from our experiment of the two different approaches. Although the Möbius transformation approach generate a map which is conformal, the landmark mismatch energy is not reduced as effective as the variational approach. The landmark mismatch energy is significantly reduced with the variational approach. The table also illustrates how the results differ with different values of λ. The landmark mismatch error can be reduced by increasing λ, but conformality will increasingly be lost.

match error is not reduced as significant as the second approach. Our second method is a variational approach which minimizes a compound energy. The development of adjustable landmark weights may be beneficial in computational anatomy. In some applications, such as tracking brain change in an individual over time, in serial images, it makes most sense to place a high priority on landmark correspondence. In other applications, such as the integration of functional brain imaging data across subjects, functional anatomy is not so tightly linked to sulcal landmarks, so it may help to trade landmark error to increase the regularity of the mappings.

3.6 Appendix

Monotonic decrease of energy

Claim : With our algorithm, the energy is strictly decreasing.

Proof : Our energy (in continuous form) can be written as: $E(u) = 1/2 \int ||\nabla u||^2 + \lambda \int \delta_E ||(u - v)||^2$ where v is the conformal mapping from the control cortical sur-

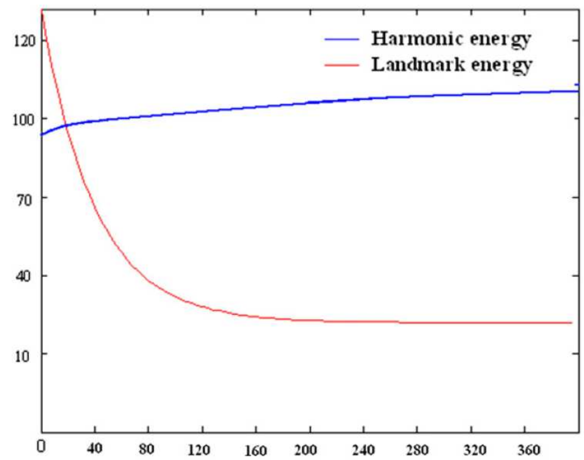

Figure 3.9: This figure shows how the harmonic energy and landmark energy change, as the number of iterations increases, using our steepest descent algorithm. Initially, the rate of change of the harmonic energy is small while the rate of change of landmark energy is comparatively large. Note that a Lagrange multiplier governs the weighting of the two energies, so a compromise can be achieved between errors in landmark correspondence and deviations from conformality.

face to the sphere. Now,

$\frac{d}{dt}|_{t=0}E(u+tw) = \int \nabla u \cdot \nabla w + \lambda \int \delta_E(u-v) \cdot w = \int \Delta u w + \lambda \int \delta_E(u-v) \cdot w$

In our algorithm, the direction w is taken as: $w = -\Delta u - \lambda\delta_E(u-v)$. Substituting this into the above equation, we have $\frac{d}{dt}|_{t=0}E(u+tw) = -\int(\nabla u)^2 - (\lambda)^2 \int \delta_E ||u-v||^2 < 0$. Therefore, the overall energy of the mapping is strictly decreasing, as the iterations proceed.

Rate of changes in $E_{harmonic}$ and $E_{landmark}$

To explain why our algorithm can effectively preserve conformalilty while greatly reducing the landmark mismatch energy, we can look at the rate of change of $E_{harmonic}$ and $E_{landmark}$. Note that the initial map u we get is almost conformal. Thus, initially Δu is very small.

Claim : With our algorithm, the rate of change of $E_{harmonic}(u)$ is $\mathcal{O}(||\Delta u||_\infty)$ and the rate of change of $E_{landmark}$ is $\lambda^2 E_{landmark}(u) + \mathcal{O}(||\Delta u||_\infty)$. Here the norm is the supremum norm over the surface.

Proof : Recall that in our algorithm, the direction w is taken as: $w = -\Delta u - \lambda\delta_E(u-v)$. Now, the rate of changes are

$$
\begin{aligned}
E_{harmonic} &= |\frac{d}{dt}|_{t=0} E_{harmonic}(u+tw)| = |\int \nabla u \cdot \nabla w| = |\int \Delta u \cdot w| \\
&= |\int ||\Delta u||^2 + \int \delta_E \Delta u \cdot (u-v)| \\
&\leq ||\Delta u||_\infty^2 + 8\lambda\pi||\Delta u||_\infty = \mathcal{O}(||\Delta u||_\infty) \\
E_{landmark} &= |\frac{d}{dt}|_{t=0} E_{landmark}(u+tw)| \\
&= |\int (\lambda\delta_E)^2(u-v)\cdot w + \int \delta_E(u-v)\cdot \Delta u| \\
&\leq \lambda^2 E_{landmark}(u) + 8\pi||\Delta u||_\infty = \lambda^2 E_{landmark}(u) + \mathcal{O}(||\Delta u||_\infty)
\end{aligned}
$$

Since initially the map is almost conformal and Δu is very small, the change in harmonic energy is very small. Conversely, initially the landmark energy is comparatively large. Since the rate of change of $E_{landmark}$ is $\lambda^2 E_{landmark}(u) + \mathcal{O}(||\Delta u||_\infty)$, the change in landmark energy is more significant (see Figure 3.9 for an illustration).

CHAPTER 4

Solving Variational Problems on Riemann Surfaces with Conformal Parameterization

4.1 Introduction

Solving variational problem is an important topic in mathematics. A lot of daily life problems can be solved by formulating them as variational problems that minimize certain kind of energy functionals. This type of problem has a very long history and has found various applications in different research areas such as physics, control theory, statistics as well as image processing. For example, a lot of partial differential equations (PDEs) in physics are derived from the Euler-Lagrange equations of the variational problems. In computer vision research, many problems, such as image denoising and image segmentation, can also be solved by variational approaches [53][54][55][56][57].

Solving variational problems in the usual Euclidean domain has been studied extensively [58]. Recently, researchers have been more and more interested in solving variational problems on general surfaces or manifolds. Applications exist in different areas of research, such as computer vision, computer graphics, image processing on the surface, geometry modeling, medical imaging as well as mathematical physics. In medical imaging research, variational methods are often used for surface registration, feature extraction, surface parameterization and so on

[19][45][46]. Besides, a lot of 2D image processing techniques can be extended to the surface by variational methods on the manifolds [59], such as image denoising, image inpainting on the surface, brain mapping, etc [60][61][62][63][36]. Geometry modeling can also be done via variational methods. Examples include surface smoothing, filling missing holes on the surface, etc [64]. In fluid dynamic, researchers are interested in simulating the fluid flow and solidification on the surface, via solving different flow models [65][66].Some other applications include texture synthesis [67][68], vector field visualization [69], weathering [70], interpolation process [71][72] and inverse problem [73]. Therefore, it is of great interest to develop a general and efficient method to solve variational problems on the surface.

In this chapter, we describe an explicit method to solve variational problems on general Riemann surfaces, using the conformal parameterization of the surface [63]. In general, variational problem is usually solved by computing its Euler-Lagrange equation, which is essentially a partial differential equation. Therefore, it is important to understand how to do calculus on general manifolds. On Riemann surfaces, differential operations are done through covariant derivatives [74][2][75]. Essentially, they are a set of coordinate invariant operators for taking directional derivatives of the functions or vector fields defined on the surface. Covariant derivatives are defined locally through the local parameterization of the manifold [2]. With arbitrary parameterization, the formulae for the covariant derivatives are generally very complicated. It results in computational difficulties and numerical inaccuracies. Here, we propose to parameterize the surface conformally with the minimum number of coordinates patches. The Riemannian metric of the conformal parameterization is simple, which is just the scalar multiplication of the conformal factor, λ. The covariant derivatives on the surface can be computed on the 2D domain with simple formula. The corresponding formula for the covariant derivatives on R^2 are similar to the usual Euclidean differential operators, except for a scaling factor λ. Therefore, with the conformal parameterization, the variational problems on general surfaces can be transformed to the 2D problems with much simpler equations. The problem can then be solved by using some well-known numerical schemes.

The key advantages of this method are as follow:

- Firstly, by mapping the surface to the 2D domain, the problem on the surface are transformed into the 2D problem. It can then be solved by efficient 2D numerical methods, instead of solving it on the complicated surface.

- Secondly, the simple Riemannian metric of the conformal parameterization allows us to have a simple formula for the covariant derivatives on the 2D domain. It makes computation much easier and reduces numerical inaccuracy.

- Thirdly, in our algorithm, covariant derivatives are computed via conformal parameterization without the orthogonal projection of the normal. It is different from some other methods, in which orthogonal projection is needed to ensure the approximated covariant derivatives are tangent to the surface. In our algorithm, the surface is identified with the 2D parameter domain with a specific Riemannian metric. Every tangent vector of the surface is represented by a 2D vector in the parameter domain and thus orthogonal projection is unnecessary. It simplifies the problem and avoids possible error arising from the inaccurate approximation of the normal.

- Fourthly, our algorithm allows us to compute the conformal parameterization of the surface with the minimum number of coordinate patches. For most of the classical parameterization methods, the surface is segmented into many portions and each portion is mapped to the 2D parameter domain. In our algorithm, we parameterize the surface with the minimum number of coordinate patches and the parameterization results are consistent along the patch boundaries because of its global parameterization nature. Specifically, the number of coordinate patches is $2g-2$, where g is the genus of the surface. The parameterization is intrinsic and depends on the holomorphic 1-form, which is in a finite dimensional linear space. Since our segmentation is based on the holomorphic 1-form, the segmentation result is finite and purely determined by holomorphic 1-form selection. Thus we could always select the segmentation that is the most appropriate to solve the PDEs.

- Finally, the conformal metric on the 2D parameter domain is induced by the actual metric of the original surface. As a result, by computing the derivatives on the 2D domain with respect to the conformal factor, we are computing the actual covariant derivatives on the surface.

4.2 Previous Works

Solving variational problems or PDEs on surfaces has been studied extensively. A popular method to solve the PDEs on surfaces is to discretize the problem on the surface triangulation [60][76][66][77]. In this approach, the covariant differential operators on the surface are approximated by finite element methods on the triangulation grids.

Another common approach is to solve the PDE on the implicit manifold, which is based on the level set method [78][79][80][81][82][83][84]. In this approach, the surface is the zero set of level set function defined in R^3, in which the surface is embedded in. The PDE on the surface is extended to be defined on a narrow band of the surface. Recently, Ratz et al. [85] proposed to solve the PDEs on the surface implicitly by reformulating the problem on a larger domain in one higher dimension and introduce a diffuse interface region of a phase-field variable, which is defined in the whole domain. The surface of interest is now only implicitly given by the $\frac{1}{2}$-level set of this phase-field variable.

Variational problems or PDEs on surfaces can also be solved by parameterizing the surface onto the 2D parameter domain [86][65][63]. Differential operators on the surface are expressed within the coordinates system. The complexity of the differential operators' expression depends mainly on the parameterization, which may result in more derivative terms and non-constant coefficients. To improve this method, our group have recently reported briefly about using conformal mapping to parameterize the surface. The formula of the covariant derivative under conformal parameterization are comparatively simple [63]. To test the method, we have also reported application of the algorithm to feature extraction in the brain mapping research [46][1].

We have summarized the three common parameterization methods in Table 4.1.

4.3 Theoretical Background

4.3.1 Differential operators on general manifolds

The calculus of variation has found various important applications. Differentiation and integration are the basic tools for solving this kind of problem. In order to extend the calculus of variation on the 2D domain to 3D Riemann surface,

Table 4.1: The list of three common methods that solve variational problems/PDEs on general surfaces.

Method	Principle	Comments
Discretization on surface triangulation [60], [76], [66]	Covariant differential operators on the surface are approximated by finite element methods on the triangulation grids.	Orthogonal projection is needed in some cases to ensure the approximated covariant derivatives to be tangent to the surface.
Level set approach [80], [81]	The surface is represented by the zero set of a level set function and the PDE on the surface is extended to a PDE that is defined on a narrow band of the surface.	Equations can be solved by Cartesian grid methods on the narrow band.
Surface parameterization [86], [65], [63]	The surface is parameterized to a simple domain such as the 2D rectangle. Differential operators on the surface are expressed within the coordinates system.	The complexity of the differential operators' expression depends mainly on the parameterization, which may result in more derivative terms and non-constant coefficients.

we need to define differential operators on functions and vector fields that are coordinate invariant.

In Euclidean space, we conventionally differentiate the vector field $(x_1(t),...,$ $x_n(t))$ on a curve pointwisely to get $(x_1'(t), ..., x_n'(t))$. However, pointwise differentiation does not work for general manifolds because it is not coordinate invariant. For example, consider the parameterized circle in the plane given in Euclidean coordinate $(x(t), y(t)) = (cos\ t, sin\ t)$. Its acceleration at time t is $(-cos\ t, -sin\ t)$. However, in polar coordinates, the same curve is described as $(r(t), \theta(t)) = (1, t)$ and the acceleration is $(0, 0)$.

The problem is this: In order to differentiate a vector field $\overrightarrow{V}(t)$ along a curve, we have to write a difference quotient involving $\overrightarrow{V}(t)$ and $\overrightarrow{V}(t_0)$ which live on two different tangent spaces. Therefore, it doesn't make sense to subtract. Secondly, even if we can differentiate the vector field pointwisely, it is not guaranteed that the 'derivative' is a tangent vector on the manifold.

We therefore need to define a differential operator on the vector field, which is coordinate invariant. This can be done by covariant differentiation $\nabla_X Y$, where X is called the direction of the differentiation. To do so, we need to develop a way to compare tangent vectors at different points. On $\mathbb{R}^2$, we usually parallel translating the vectors and subtract. But on general manifolds, we do not have the concept of parallel translation. So, what is parallel translation on a surface $M \subset \mathbb{R}^3$? We say that a vector field $\overrightarrow{V}(\gamma(t))$ along a curve $\gamma(t)$ is parallel if: $D_t\overrightarrow{V}(\gamma(t)) =$ projection of $\frac{d}{dt}\overrightarrow{V}(\gamma(t))$ onto the tangent space $= 0$. We have the following important fact:

Parallel Translation : Given a curve $\gamma : I \to M$ and a vector $\overrightarrow{V}_0 \in T_{\gamma(t_0)}M$, there exists a unique parallel vector field $\overrightarrow{V}$ along γ with $\overrightarrow{V}(t_0) = V_0$.

With the parallel translation along a curve γ, we can define an operator: $P^{\gamma}_{t_0t_1} : T_{\gamma(t_0)}M \to T_{\gamma(t_1)}M$ by setting $P_{t_0t_1}(\overrightarrow{V}_0) = V(t_1)$ where V is the parallel vector field along γ with $\overrightarrow{V}(0) = \overrightarrow{V}_0$. This is clearly an linear isomorphism.

Now, we can define: $\nabla_X Y|_p$ as follow: Let $\gamma : [0,1] \to M$ be a curve such that $\gamma(0) = p$ and $\gamma'(0) = Y|_p$. We define:

$$\nabla_X Y|_p = lim_{t\to 0}\frac{P^{\gamma}_{0t}{}^{-1}Y(\gamma(t)) - Y(p)}{t} \tag{4.1}$$

It is called the *covariant derivatives.* Essentially, they are a coordinate invariant set of operators for taking directional derivatives of the functions or vector fields defined on the surface S.

Generally, the covariant derivative $\nabla_X F$, where X is a tangent vector on S, F is either a function or a vector field defined on S, satisfies the following properties:

(I) $\nabla_X F$ is linear in X over $C^\infty(S)$: $\nabla_{fX_1+gX_2}F = f\nabla_{X_1}F + g\nabla_{X_2}F$.

(II) $\nabla_X F$ is linear over R in F: $\nabla_X(aF_1 + bF_2) = a\nabla_X F_1 + b\nabla_X F_2$.

(III) ∇ satisfies the product rule: $\nabla_X(fF) = f\nabla_X F + X(f)F$

(Here, we define $X(f) = \frac{d}{dt}|_{t=0} f(\alpha(t))$ where $\alpha : (-1, 1) \to S$ is a curve on S such that $\alpha'(0) = X$.)

This basically defines the covariant derivatives. $\nabla_X F$ is called the covariant derivative of F in the direction X.

Let $\varphi : R^2 \to S$ be a parameterization of S (not necessarily conformal). Define $g = (g_{ij})_{i,j=1,2}$ where $g_{ij} = \varphi_{x_i} \cdot \varphi_{x_j}$ are the Riemannian metric coefficients. Let $F = F_1\varphi_{x_1} + F_2\varphi_{x_2}$ and $X = X_1\varphi_{x_1} + X_2\varphi_{x_2}$ be a vector field and a tangent vector on S respectively. Let $f : S \to R$ be a function defined on S. Then:

$$\begin{aligned} \nabla_X f &= \sum_{i,j,k=1}^{2} (g^{ij}\partial_i f) X_k g_{jk} \\ \nabla_X F &= \sum_{i,j,k=1}^{2} (XF_k + X_i F_j \Gamma^k_{ij})\varphi_{x_k} \end{aligned} \tag{4.2}$$

where $\Gamma^k_{ij} = \Sigma^2_{l=1} \frac{1}{2} g^{kl}(\partial_i g_{jl} + \partial_j g_{il} - \partial_l g_{ij})$ and $(g^{ij})_{i,j=1,2}$ is the inverse of g.

Note that the complexity of the covariant derivative depends solely on the complexity of the Riemannian metric g. An arbitrary parameterization might have a very complicated g. It is thus important for us to look for a parameterization that gives simple Riemannian metric g. It turns out that the conformal mapping is such a map that has simple Rimannian metric.

With covariant derivative, we can define other useful differential operators on S, which are analogous to those on R^2. We are going to list several of them below.

Firstly, the gradient of the function f, $\nabla_S f$, is characterized by the fact that:

$$X(f) =< \nabla_S f, X >_S \tag{4.3}$$

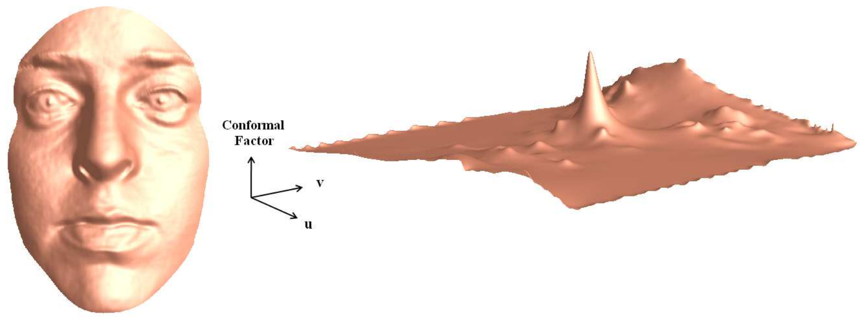

Figure 4.1: The plot of the conformal factor λ of a human face verses u and v of the parameter domain. The conformal factor is a smooth function which describe the stretching effect under the conformal parameterization. Observe that the approximation of the conformal factor function is reasonably smooth.

By simple checking, we get that ∇f has the following coordinate expression:

$$\nabla_S f = \sum_{i,j=1}^{2} g^{ij} \partial_i f \varphi_{x_j} \tag{4.4}$$

Secondly, we can define divergence on S as follow:

$$\nabla_S \cdot F := \frac{1}{\sqrt{det(g)}} \sum_{i=1}^{2} \partial_i (\sqrt{det(g)} F_i) \tag{4.5}$$

With the definition of the gradient and the divergence, we can define the Laplacian operator on S as follow:

$$\begin{aligned} \triangle_S f &:= \nabla_S \cdot (\nabla_S f) = \nabla_S \cdot (\sum_{i,j=1}^{2} g^{ij} \partial_i f) \\ &= \frac{1}{\sqrt{det(g)}} \sum_{i=1}^{2} \partial_i (\sqrt{det(g)} \sum_{j=1}^{2} g^{ji} \partial_j f) \end{aligned} \tag{4.6}$$

A more complete development of various differential operators on the surface can be found at [1].

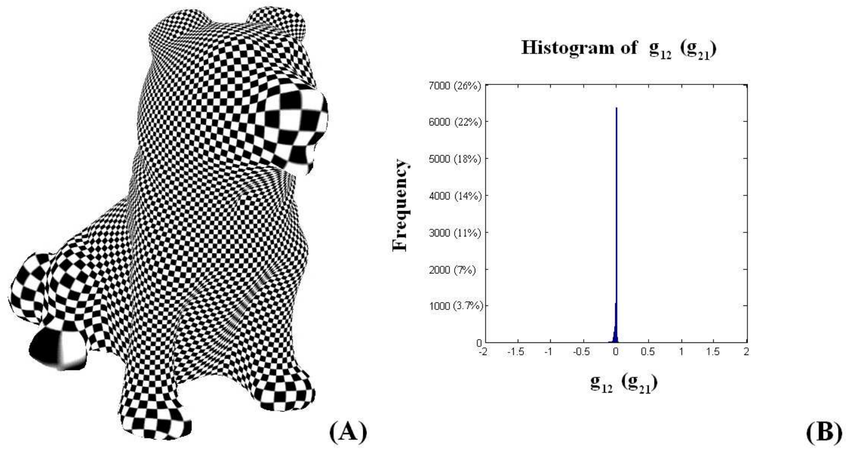

Figure 4.2: (A) shows the conformal coordinates grid on the dog surface introduced using the conformal parameterization. (B) shows the histogram of $g_{12} = g_{21}$ of a Riemann surface under the conformal parameterization. Observe that $g_{12} = g_{21}$ are very close to zero at most vertex. It means the Riemannian metric is a diagonal matrix, which results in simple expression for the covariant derivatives.

4.4 Solving variational problems on Riemann surface with the conformal parameterization

In section III(B), we have described how differential operators are defined on the surface with the given parameterization. With the concept of differentiation and integration on the surface, we can use calculus of variation to solve variational problems on surfaces. In this section, we will describe how covariant derivatives can be easily computed using the conformal parameterization and how it can be applied to solve variational problems.

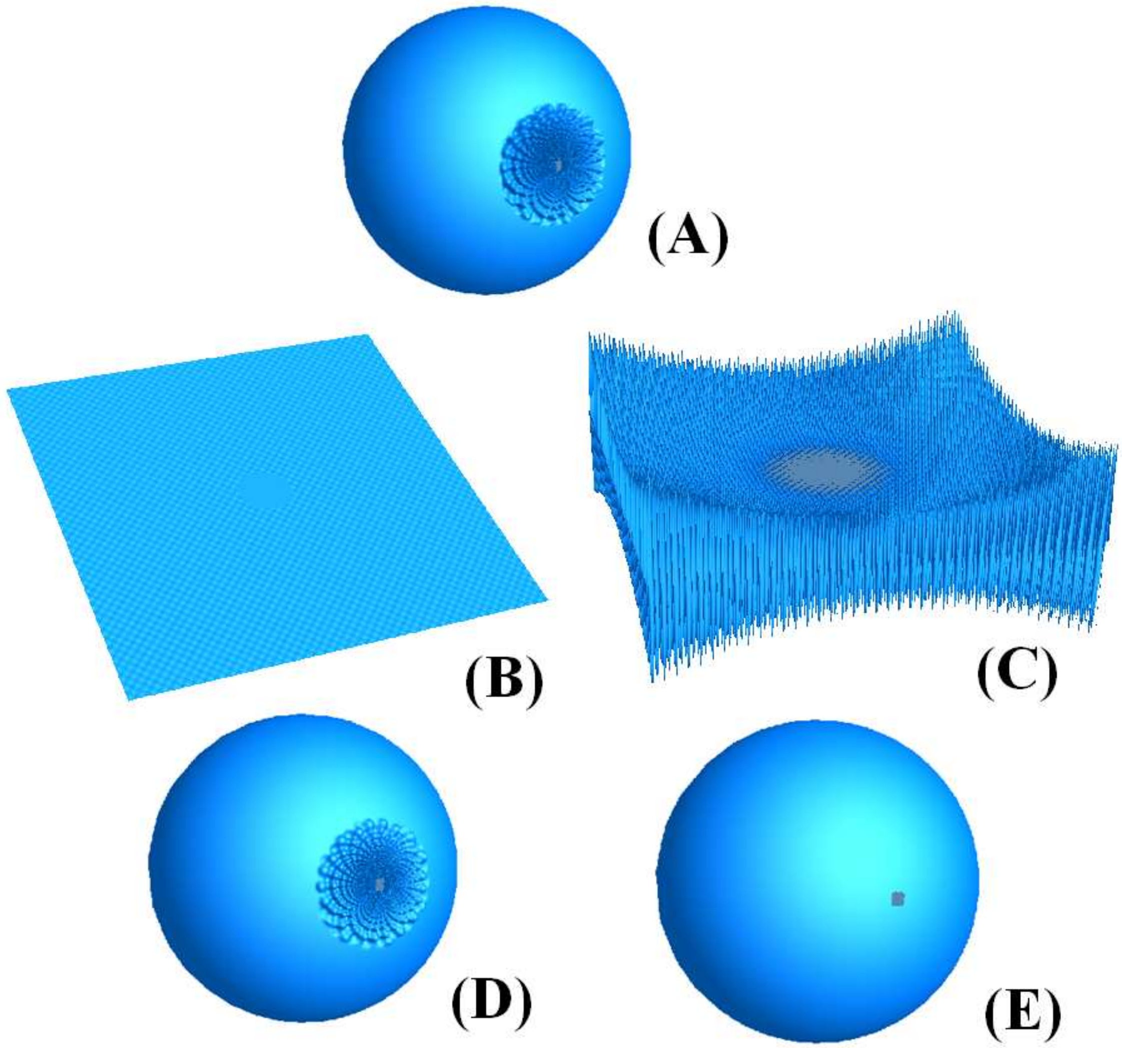

Figure 4.3: This figure demonstrates the importance of including the conformal factor in computing the differential operators on the manifold. (A) shows a unit sphere (minus a hole near the south pole) with noise introduced near the south pole. The surface is parameterized conformally to the 2D parameter domain with large stretching near the south pole. (B) shows the graph of the Eulcidean TV norm of the noise: $TV_{eucl.}(g) = |\nabla g|$. (C) shows the manifold version of the TV norm (with conformal factor included): $TV_{manifold}(g) = \frac{1}{\lambda}|\nabla g|$. (D) shows the denoising result which minimize the Eulcidean TV energy. The noise cannot be removed. (D) shows the denoising result which minimizes the manifold TV norm. The noise is successfully removed.

4.4.1 Computation of convariant derivatives using conformal parameterization

Given a parameterization of the surface S, we can express the surface differential operators within its coordinates. In section III(B), we have discussed how covariant derivatives can be computed with the various formulae defined on R^2. The formulae consists of the Riemannian metric coefficients g_{ij}, which are functions defined on S. With an arbitrary parameterization, the Riemannian metric can be complicated. As a result, the equation of the surface differential operators can become substantially complex when written in the coordinate system, involving non-constant coefficients and more derivative terms. Therefore, it is important to look for a parameterization with simple Riemanninan metric.

As described in section III(A), the conformal parameterization has a simple Riemannian metric, namely, $g_{ij} = \begin{cases} \lambda & \text{if } i = j; \\ 0 & \text{if } i \neq j. \end{cases}$ In other words, the four metric coefficients are reduced to one coefficient metric λ, called the conformal factor. With this property, surface differential operators can be expressed within the conformal coordinates with simple formulae. The expressions are similar to the usual Euclidean differential operators, except for a scalar multiplication of the conformal factor. The conformal factor at a point p on the surface S can be determined by computing the scaling factor of a small area around p under the parameterization $\phi : R^2 \to S$. Mathematically, $\lambda(p) = \frac{\mathbf{Area}(B_\epsilon(p))}{\mathbf{Area}(\phi^{-1}(\mathbf{B}_\epsilon(\mathbf{p})))}$, where $B_\epsilon(p)$ is an open ball around p of radius p. Figure 4.1 shows the plot of conformal factor λ verses u and v of the parameter domain. The conformal factor is a smooth function which describe the stretching effect under the conformal parameterization. Observe that the approximation of the conformal factor function is reasonably smooth. Figure 4.2(B) shows the histogram of g_{12} of the Riemann surface under the conformal

Table 4.2: Illustrates a list of formulas for some standard differential operators on a general manifold.

1.	$\nabla_M f = \sum_{i,j} g^{ij}\partial_j f \partial_i$, where (g^{ij}) is the inverse of the Riemannian metric (g_{ij}). With the conformal parametrization ϕ, the conformal factor λ, $\nabla_M f = D_x f\mathbf{i} + D_y f\mathbf{j}$, where $(\mathbf{i},\mathbf{j}) = (\frac{\partial}{\partial x}/\sqrt{< \frac{\partial}{\partial x}, \frac{\partial}{\partial x} >}, \frac{\partial}{\partial y}/\sqrt{< \frac{\partial}{\partial y}, \frac{\partial}{\partial y} >})$ $= \frac{1}{\sqrt{\lambda}}(\frac{\partial}{\partial x}, \frac{\partial}{\partial y})$.
2.	Suppose $h : M \to \mathbb{R}$ is a smooth function, Length of $h^{-1}(0) = \int_M \delta(h)\sqrt{< \nabla_M h, \nabla_M h >}dS$ $= \int_M \sqrt{< \nabla_M H(h), \nabla_M H(h) >}dS$ $= \int_{\mathbb{C}} \delta(h \circ \phi)\sqrt{\lambda}\ \lVert\nabla h \circ \phi\rVert dxdy$ $= \int_{\mathbb{C}} \sqrt{\lambda}\ \lVert\nabla H(h \circ \phi)\rVert dxdy$ where H is the Heaviside function.
3.	For a differential operator on vector field, the covariant derivative satisfies the following properties: (P1) $\nabla_{fX_1+gX_2}Y = f\nabla_{X_1}Y + g\nabla_{X_2}Y$ for $f, g \in C^\infty(M)$; (P2) $\nabla_X(aY_1 + bY_2) = a\nabla_X Y_1 + b\nabla_X Y_2$, $a, b \in \mathbb{R}$; (P3) $\nabla_X(fY) = f\nabla_X Y + (Xf)Y$ for $f \in C^\infty(M)$. Suppose $\{\partial_i\}$ is the coordinate basis of the vector field, then $< \nabla_{\partial_i}\partial_j, \partial_l >= 1/2(\partial_i g_{jl} + \partial_j g_{li} - \partial_l g_{ij})$, $\nabla_{\partial_i}\partial_j = \Gamma^m_{ij}\partial_m$, where $\Gamma^m_{ij} = \frac{1}{2\lambda}(\partial_i g_{jm} + \partial_j g_{mi} - \partial_m g_{ij})$.
4.	For the divergence and Laplacian, we have $div_M(\Sigma^2_{i=1} X_i \frac{\partial}{\partial x_i}) = \sum^2_{i=1} \frac{1}{\lambda}\partial_i(X_i\lambda)$, $\triangle_M f = \sum^2_{j=1}(1/\lambda)\ \partial_j\partial_j f$.
5.	Suppose C is a curve represented by the zero level set of $\phi : M \to \mathbb{R}$, **Geodesic curvature of** $C = div_M(\frac{\nabla_M\phi}{\lVert\nabla_M\phi\rVert})$.

parameterization. Note that by definition, $g_{12} = g_{21} = \phi_u \cdot \phi_v$, where $\phi(u, v)$ is the conformal parameterization of the surface. Observe that $g_{12}(= g_{21})$ are very close to zero at most vertex. It means the Riemannian metric is a diagonal matrix, which results in simple formulae for the covariant derivatives. It turns out that the manifold differential operators expressed on the conformal parameter domain is very similar to the 2D Euclidean version 4.3.

Table 4.3: Comparison between 2D Euclidean differential operators and manifold differential operators under conformal parameterization.

	2D Euclidean	Manifold
Gradient	$\nabla f = (\frac{\partial f}{\partial u}, \frac{\partial f}{\partial v})$	$\nabla_S f = (\frac{1}{\lambda}\frac{\partial f}{\partial u}, \frac{1}{\lambda}\frac{\partial f}{\partial v})$
Laplacian	$\Delta f = \frac{\partial^2 f}{\partial u^2} + \frac{\partial^2 f}{\partial v^2}$	$\Delta_S f = \frac{1}{\lambda}\frac{\partial^2 f}{\partial u^2} + \frac{1}{\lambda}\frac{\partial^2 f}{\partial v^2}$
Divergence	$\nabla \cdot (X, Y) = \frac{\partial X}{\partial u} + \frac{\partial Y}{\partial v}$	$\nabla_S \cdot (X, Y) = \frac{1}{\lambda}\frac{\partial(\lambda X)}{\partial u} + \frac{1}{\lambda}\frac{\partial(\lambda Y)}{\partial v}$

We will now express some of the most important surface differential operators under the conformal parameterization ϕ of the surface. From section III(B), we have discussed the expression of $\nabla_S f$, $\triangle_S f$, Γ^k_{ij} and $\nabla_X Y$ under general parameterization of the surface, where $f : S \to R$, X, Y are vector fields defined on S. Substituting $g_{11} = g_{22} = \lambda$; $g_{12} = g_{21} = 0$ into the equations (3)(4)(5), we obtained simple formulae for these important surface differential operators within the conformal parameter domain:

$$\begin{aligned} \nabla_S f &= D_x f\vec{\mathbf{i}} + D_y f\vec{\mathbf{j}} \\ div_S\vec{X} &= \frac{1}{\lambda}\frac{\partial}{\partial x}(\lambda X_1) + \frac{1}{\lambda}\frac{\partial}{\partial y}(\lambda X_2) \\ \triangle_S f &= \frac{1}{\lambda}\frac{\partial^2}{\partial x^2}(f \circ \phi) + \frac{1}{\lambda}\frac{\partial^2}{\partial y^2}(f \circ \phi) \end{aligned} \tag{4.7}$$

where $D_x f = \frac{1}{\sqrt{\lambda}}\frac{\partial}{\partial x} f \circ \phi; D_y f = \frac{1}{\sqrt{\lambda}}\frac{\partial}{\partial y} f \circ \phi$;

$(\vec{\mathbf{i}}, \vec{\mathbf{j}}) = (\frac{\partial}{\partial x}/\sqrt{< \frac{\partial}{\partial x}, \frac{\partial}{\partial x} >_S}, \frac{\partial}{\partial y}/\sqrt{< \frac{\partial}{\partial y}, \frac{\partial}{\partial y} >_S})$; $\frac{\partial}{\partial x} := \frac{\partial \phi}{\partial x}$ and $\frac{\partial}{\partial y} := \frac{\partial \phi}{\partial y}$ are the projected tangent vectors of $e_1 = (1, 0)$ and $e_2 = (0, 1)$ onto the surface under the conformal parameterization ϕ respectively; $\vec{X} = (X_1, X_2) = X_1\frac{\partial}{\partial x} + X_2\frac{\partial}{\partial y}$; $f : S \to R$ is a smooth function on S.

As shown above, the expressions for the surface differential operators are very similar to the usual Euclidean differential operators, except for a scalar multiplication of the conformal factor λ. It means the conformal parameterization provides a natural coordinates grid on the surface. Intuitively, the conformal parameterization preserves the inner product up to a scaling factor and so the local geometry is preserved up to a scaling of λ. As a result, the differentials on S are well-preserved, except for a multiplication of $\sqrt{\lambda}$, to adjust for the length stretching and λ for area distortion. With this conformal grid on the surface, we can consider $D_x f$ and $D_y f$ as the analogous partial derivatives on S. For example,

$$\begin{aligned} D_x f &= \lim_{\triangle x \to 0} \frac{f \circ \phi(x + \triangle x, y) - f \circ \phi(x, y)}{dist(\phi(x + \triangle x), \phi(x))} \\ &= \lim_{\triangle x \to 0} \frac{f \circ \phi(x + \triangle x, y) - f \circ \phi(x, y)}{\sqrt{\lambda} \triangle x} \\ &= \frac{1}{\sqrt{\lambda}} \frac{\partial f \circ \phi}{\partial x} \end{aligned}$$

Several important equations that are useful for the calculus of variation on R^2 are also valid on general surfaces. For example, we have the integration by part formula on surface:

$$\int_S (u \triangle_S v - v \triangle_S u) dV = \int_{\partial S} (u \nabla_S v \cdot \overrightarrow{N} - v \nabla_S u \cdot \overrightarrow{N}) d\widetilde{V} \tag{4.8}$$

The analogous Green's formula on the surface is:

$$\int_S < \nabla_S u, \vec{X} >_S dV = - \int_S u div_M \vec{S} dV + \int_{\partial S} u < \vec{X}, \vec{N} > d\widetilde{V} \tag{4.9}$$

where $\vec{N}$ is the unit normal vector.

Furthermore, given a smooth function $h : S \to R$, the length L of the zero level set $h^{-1}(0)$ of h, which is a curve on the surface, can be computed similarly as in R^2:

$$
\begin{aligned}
L &= \int_S \delta(h)\sqrt{< \nabla_S h, \nabla_S h >} dA \\
&= \int_S \sqrt{< \nabla_S H(h), \nabla_S H(h) >} dA \\
&= \int_{R^2} \delta(h \circ \phi)\sqrt{\lambda}\ ||\nabla h \circ \phi|| dxdy \\
&= \int_{R^2} \sqrt{\lambda}\ ||\nabla H(h \circ \phi)|| dxdy
\end{aligned}
\tag{4.10}
$$

where H is the Heaviside function.

Proof :

Recall that the Co-area formula reads:

$$
\int_{\Omega \subset \mathbb{R}^2} f(x,y)|\nabla u| dxdy = \int_{\mathbb{R}} \int_{\{u(x,y)=r\}} f(x,y) d\mathcal{H} dr \tag{4.11}
$$

where $\mathcal{H}$ is the Hausdorff measure.

Let ϕ be the conformal parametrization of the surface M and $\zeta = u \circ \phi$. Then,

$$
\begin{aligned}
\int_M |\nabla_M H(u)|_M dS &= \int_{\mathbb{R}^2} \delta(\zeta)|\nabla\zeta|)\sqrt{\lambda}dxdy \\
&= \int_{\mathbb{R}} \int_{\{\zeta(x,y)=r\}} \sqrt{\lambda}\delta(\zeta)dsdr \\
&= \int_{\{\zeta(x,y)=0\}} ds \\
&= \int_0^1 \sqrt{\lambda}|\mathbf{c}'(t)|dt \\
&= \int_0^1 \sqrt{\lambda}|\phi \circ \mathbf{c}'(t)|dt \\
&= length\ of\ \{u=0\}
\end{aligned}
$$

where $\mathbf{c}(t)$ is the parametrization of $\zeta(x,y) = 0$

Q.E.D.

The geodesic curvature G of $h^{-1}(0)$ can also be computed as:

$$
G = div_S(\frac{\nabla_S h}{||\nabla_S h||}) \tag{4.12}
$$

similar to the case in R^2.

Proof :

Recall that the geodesic curvature of of a curve:

$$
\begin{aligned}
\vec{\gamma} &= \frac{\sqrt{< D_t\dot{\vec{\gamma}}, D_t\dot{\vec{\gamma}} >}}{< \dot{\vec{\gamma}}, \dot{\vec{\gamma}} >} - \frac{< D_t\dot{\vec{\gamma}}, \dot{\vec{\gamma}} >}{< \dot{\vec{\gamma}}, \dot{\vec{\gamma}} >^{3/2}} = \frac{< \dot{\vec{\gamma}}, D_t\dot{\vec{\gamma}}^{\perp} >}{< \dot{\vec{\gamma}}, \dot{\vec{\gamma}} >^{3/2}} \\
&= \frac{\sqrt{< D_t\dot{\vec{\gamma}}, D_t\dot{\vec{\gamma}} >}}{< \dot{\vec{\gamma}}, \dot{\vec{\gamma}} >} - \frac{< D_t\dot{\vec{\gamma}}, \dot{\vec{\gamma}} >}{< \dot{\vec{\gamma}}, \dot{\vec{\gamma}} >^{3/2}} = \frac{< \dot{\vec{\gamma}}, D_t\dot{\vec{\gamma}}^{\perp} >}{< \dot{\vec{\gamma}}, \dot{\vec{\gamma}} >^{3/2}} \\
&= \frac{\sqrt{< D_t\dot{\vec{\gamma}}, D_t\dot{\vec{\gamma}} >}}{< \dot{\vec{\gamma}}, \dot{\vec{\gamma}} >} - \frac{< D_t\dot{\vec{\gamma}}, \dot{\vec{\gamma}} >}{< \dot{\vec{\gamma}}, \dot{\vec{\gamma}} >^{3/2}} = \frac{< \dot{\vec{\gamma}}, D_t\dot{\vec{\gamma}}^{\perp} >}{< \dot{\vec{\gamma}}, \dot{\vec{\gamma}} >^{3/2}} \\
&= \frac{\sqrt{< D_t\dot{\vec{\gamma}}, D_t\dot{\vec{\gamma}} >}}{< \dot{\vec{\gamma}}, \dot{\vec{\gamma}} >} - \frac{< D_t\dot{\vec{\gamma}}, \dot{\vec{\gamma}} >}{< \dot{\vec{\gamma}}, \dot{\vec{\gamma}} >^{3/2}} = \frac{< \dot{\vec{\gamma}}, D_t\dot{\vec{\gamma}}^{\perp} >}{< \dot{\vec{\gamma}}, \dot{\vec{\gamma}} >^{3/2}}
\end{aligned} \tag{4.13}
$$

Let the parametrization of the zero level set of ϕ be $\vec{\gamma} = (X(t), Y(t))$. Then $\phi(X(t), Y(t)) = 0$.

This implies (1):

$$< \nabla_M \phi, \dot{\vec{\gamma}} >= 0 \tag{4.14}$$

and (2):

$$< D_t(\nabla_M \phi), \dot{\vec{\gamma}} > + < D_t\dot{\vec{\gamma}}, \nabla_M \phi >= 0 \tag{4.15}$$

Now, $D_t\vec{V}(t) = \sum_{i=1}^{2}(\dot{V}_k + \Gamma_{ij}^k \gamma_i V_j)\partial_k$

Thus, for conformal parametrization we have (3):

$$
\begin{aligned}
D_t\dot{\vec{\gamma}} = (\ddot{X} + (\frac{1}{2\lambda}\frac{\partial\lambda}{\partial x})(\dot{X}^2 - \dot{Y}^2) - (\frac{1}{\lambda}\frac{\partial\lambda}{\partial y}\dot{X}\dot{Y})\ , \\
\ddot{Y} - (\frac{1}{2\lambda}\frac{\partial\lambda}{\partial y})(\dot{X}^2 - \dot{Y}^2) - (\frac{1}{\lambda}\frac{\partial\lambda}{\partial x})\dot{X}\dot{Y})
\end{aligned}
$$

and (4):

$$D_t(\nabla_M \phi) = (\dot{\phi_x} + (\frac{1}{2\lambda}\frac{\partial\lambda}{\partial x})({\phi_x}^2 - {\phi_y}^2) - (\frac{1}{\lambda}\frac{\partial\lambda}{\partial y}\phi_x\phi_y)\ ,$$
$$\dot{\phi_y} - (\frac{1}{2\lambda}\frac{\partial\lambda}{\partial y})({\phi_x}^2 - {\phi_y}^2) - (\frac{1}{\lambda}\frac{\partial\lambda}{\partial x})\phi_x\phi_y\ )$$

$$D_t(\nabla_M \phi) = (\dot{\phi_x} + (\frac{1}{2\lambda}\frac{\partial\lambda}{\partial x})({\phi_x}^2 - {\phi_y}^2) - (\frac{1}{\lambda}\frac{\partial\lambda}{\partial y}\phi_x\phi_y)\ ,$$
$$\dot{\phi_y} - (\frac{1}{2\lambda}\frac{\partial\lambda}{\partial y})({\phi_x}^2 - {\phi_y}^2) -$$
$$(\frac{1}{\lambda}\frac{\partial\lambda}{\partial x})\phi_x\phi_y\ )$$

Combining (1), (2), (3), (4), we have: $\dot{X}^2 + \dot{Y}^2 = (1 + (\phi_x/\phi_y)^2)\dot{X}^2$ and

$$\begin{aligned}\frac{< D_t\dot{\vec{\gamma}}^{\perp}, \dot{\vec{\gamma}} >}{< \dot{\vec{\gamma}}, \dot{\vec{\gamma}} >^{3/2}} &= \lambda(\dot{X}\ddot{Y} - \dot{Y}\ddot{X}) \\ &= -\frac{\lambda}{\phi_y}[\phi_{xx}\dot{X}^2 + 2\phi_{xy}\dot{X}\dot{Y} + \phi_{yy}\dot{Y}^2]\dot{X} - \dot{X}(\dot{X}^2 + \dot{Y}^2)(\frac{1}{2\lambda}\frac{\partial\lambda}{\partial y}) \\ &+ \dot{Y}(\dot{X}^2 + \dot{Y}^2)(\frac{1}{2\lambda}\frac{\partial\lambda}{\partial x})\end{aligned}$$

So,

$$
\begin{aligned}
\kappa &= \frac{<\dot{\vec{\gamma}}, D_t\dot{\vec{\gamma}}^{\perp}>}{<\dot{\vec{\gamma}}, \dot{\vec{\gamma}}>^{3/2}} = \frac{\lambda(\dot{X}\ddot{Y} - \dot{Y}\ddot{X})}{\lambda^{3/2}(\dot{X}^2 + \dot{Y}^2)^{3/2}} \\
&= \frac{1}{\sqrt{\lambda}}(\frac{\phi_{xx}\phi_y^2 - 2\phi_{xy}\phi_x\phi_y + \phi_{yy}\phi_x^2}{(\phi_x^2 + \phi_y^2)^{3/2}}) + \frac{1}{2\lambda^{3/2}}(\phi_x\frac{\partial\lambda}{\partial x} + \phi_y\frac{\partial\lambda}{\partial x}) \\
&= \frac{1}{\sqrt{\lambda}}(\frac{\phi_{xx}\phi_y^2 - 2\phi_{xy}\phi_x\phi_y + \phi_{yy}\phi_x^2}{(\phi_x^2 + \phi_y^2)^{3/2}}) + \frac{1}{2\lambda^{3/2}}(\phi_x\frac{\partial\lambda}{\partial x} + \phi_y\frac{\partial\lambda}{\partial x}) \\
&= \frac{1}{\sqrt{\lambda}}\nabla\cdot(\frac{\nabla\phi}{|\nabla\phi|}) + \frac{1}{\lambda^{3/2}}\nabla\phi\cdot\nabla\lambda \\
&= \frac{1}{\lambda}\nabla\cdot(\lambda(\frac{1/\lambda\nabla\phi}{\sqrt{\lambda|\nabla\phi|^2}})) \\
&= \frac{1}{\lambda}\nabla\cdot(\lambda(\frac{\nabla_M\phi}{\sqrt{<\nabla_M\phi, \nabla_M\phi>}})) \\
&= div_M(\frac{\nabla_M\phi}{\sqrt{<\nabla_M\phi, \nabla_M\phi>}})
\end{aligned}
$$

Q.**E**.**D**.

4.4.2 Examples

Since the important equations useful for the calculus of variation on R^2 can be extended to general surfaces, we can solve the variational problems on the surface easily using the differential operators defined in III(B). In this section, we will demonstrate the theoretical concept by considering two examples.

Example 1 : (**Harmonic Energy**)

Suppose S is a Riemann surface with boundary ∂S. Let $\phi : R^2 \to S$ be its conformal parameterization. We are interested in looking for a smooth function $f : S \to R$ that minimizes: $E(f) = \int_S ||\nabla_S f||_S^2 dS$ and $f = 0$ on ∂S.

Consider:

$$
\begin{aligned}
\frac{d}{dt}|_{t=0}E(f+tg) &= \int_S ||\nabla_S(f+tg)||_S^2 dS \\
&= \int_S < (\nabla_S f + t\nabla_S g), (\nabla_S f + t\nabla_S g) >_S dS \\
&= 2\int_S < \nabla_S f, \nabla_S g >_S dS \\
&= 2\int_S (\triangle_S f) g dS.
\end{aligned}
\tag{4.16}
$$

So, the Euler-Lagrange equation is:

$$
\frac{df^t}{dt} = -2\triangle_S f^t \text{ or } \frac{df^t \circ \phi}{dt} = -\frac{2}{\sqrt{\lambda}}\triangle f^t \circ \phi \tag{4.17}
$$

on the parameter domain.

It is observed that the Euler Lagrange equation of the harmonic energy on the surface is the same as its 2D version, except that the differential operators in the equation have to be replaced by the manifold operators. The corresponding equation on the parameter domain is similar to its 2D version on R^2, except for a scaler multiplication of the conformal factor. When $\lambda = 1$, the Riemann surface is flat and so it becomes identical to its 2D version.

Example 2 : (**Total Variation**)

Suppose now we are interested in looking for a minimizer $f : S \to R$ of $E(f) = \int_S ||\nabla_S f||_S dS$ where $f = 0$ on ∂S. Consider:

$$
\begin{aligned}
\frac{d}{dt}|_{t=0}E(f+tg) &= \int_S ||\nabla_S(f+tg)||_S dS \\
&= \int_S \sqrt{<(\nabla_S f + t\nabla_S g),(\nabla_S f + t\nabla_S g)>_S} dS \\
&= 2\int_S < \frac{\nabla_S f}{||\nabla_S f||_S}, \nabla_S g >_S dS \\
&= 2\int_S div_S(\frac{\nabla_S f}{||\nabla_S f||_S}) g dS.
\end{aligned}
\tag{4.18}
$$

So, the Euler Lagrange equation becomes:

$$
\frac{df^t}{dt} = -2div_S(\frac{\nabla_S f^t}{||\nabla_S f^t||_S}) \text{ or } \frac{df^t \circ \phi}{dt} = -\frac{2}{\lambda} div_S(\frac{\nabla_S f^t \circ \phi}{||\nabla_S f^t \circ \phi||_S}) \tag{4.19}
$$

on the parameter domain.

Again, the Euler Lagrange equation of the Total Variation energy is the same as its 2D version, except for the replacement of the 2D differential operators by the manifold differential operators. The corresponding equation on the parameter domain is also similar to its 2D version on R^2, except for the scaling of the conformal factor.

In general, the Euler Lagrange equation can be obtained easily from its 2D version by replacing the 2D differential operators by the manifold differential operators. The corresponding equation on the 2D parameter domain is similar to its 2D version, except for a scaling of the conformal factor.

4.4.3 The meaning of including the conformal factor

Intuitively, the meaning of scaling the differential operators by the conformal factor λ is to adjust the length and area distortion. With the angle preserving property of the conformal parameterization ϕ, a natural coordinates grid can be introduced on the surface by mapping a regular grid on R^2 onto the surface (See Figure 4.2(A)). However, the grid sizes are different at different points because of the stretching effect of the parameterization. The conformal factor λ is defined as the stretching factor of the inner product on the tangent plane of the surface under ϕ. We can therefore adjust the length and area distortion by $\sqrt{\lambda}$ or λ. Specifically, the stretching factors of the length and area under ϕ are $\sqrt{\lambda}$ and λ respectively. In order to have a more accurate approximation of the surface differential operators, we need to scale the usual Euclidean differential operators by λ. For example, the partial derivative $D_x f$ on the surface at the point $\phi(p)$ is: $D_x f(\phi(p)) = \lim_{\Delta x \to 0} \frac{\Delta f \circ \phi}{\sqrt{\lambda} \Delta x} = \frac{1}{\sqrt{\lambda}} \frac{\partial f \circ \phi}{\partial x}(p)$. Here, the grid size Δx is scaled by $\sqrt{\lambda}$ to adjust the length distortion. Similarly, $\Delta_S f(\phi(p)) = \lim_{\Delta x, \Delta y \to 0} \frac{\Delta_x(\Delta_x f \circ \phi)}{\lambda \Delta x^2} + \frac{\Delta_y(\Delta_y f \circ \phi)}{\lambda \Delta y^2}$.

Also, the surface area differential dS is equal to $\lambda dxdy$, so as to adjust for the area distortion.

To demonstrate the importance of including the conformal factor in the formula of the covariant derivatives, we consider a simple example on the unit sphere. 4.3(A) shows a unit sphere (minus a hole near the south pole) with noise introduced near the south pole. It is conformally parameterized onto the 2D parameter domain, with large stretching near the south pole. 4.3(B) shows the graph of the Eulcidean TV norm of the noise: $TV_{eucl.}(g) = |\nabla g|$. Observe that it does not reflect the noise on the surface due to the stretching effect near the south pole. 4.3(C) shows the manifold version of the TV norm (with conformal factor included): $TV_{manifold}(g) = \frac{1}{\lambda}|\nabla g|$. It effectively reflects the noise on the surface. (D) shows the denoising result which minimize the Eulcidean TV energy: $E_{eucl.}(g) = \int TV_{eucl.}(g)$. The noise cannot be removed. (D) shows the denoising result which minimizes the manifold TV norm: $E_{manifold}(g) = \int TV_{eucl.}(g)$. The noise is successfully removed. This example illustrates the importance of the conformal factor for adjusting the length and area distortion introduced through the conformal parameterization.

4.4.4 Numerical Analysis

An important question one may ask is the numerical accuracy of the algorithm. Since the conformal parameterization is only an approximation, it is of interest to examine how the numerical accuracy of the algorithm will be affected by the conformality of the parameterization. The accuracy in apprroximating the solution of the variational problem depends on the accuracy of the approximated covariant derivatives. Generally speaking, the accuracy of the approximated covariant derivatives depends on two factors:

(1) Given a Riemann surface M, the accuracy in the approximation of the conformal parameterizaton $\widetilde{\phi} : R^2 \to M$.

(2) The accuracy in the approximation of the partial derivatives in R^2.

In this section, we will examine the accuracy in the approximation of several important covariant derivatives with respect to the above two factors. This can be summarized by the following three theorems.

THEOREM 4.4.4.1 :

Given a compact Riemann surface M and its approximated conformal parameterization $\widetilde{\phi} : D \subseteq R^2 \to M$. Let $(\widetilde{g}^{ij})$ be its approximated inverse Riemannian metric of $\widetilde{\phi}$, where $\widetilde{g}^{11} = \widetilde{g}^{22} = \lambda^{inv}$ and $\widetilde{g}^{12} = \widetilde{g}^{21} = 0$. Let (g^{ij}) be its actual inverse Riemannian metric. Assume that $|\widetilde{g}^{ij} - g^{ij}|$ are bounded by the error ϵ. Given $f : M \to R$. Suppose that the error in approximating the partial derivatives of $f \circ \widetilde{\phi}$ are bounded by h. We have:

$$||\nabla_M^{appro.} f - \nabla_M^{real} f||_M \leq (\frac{4C\sqrt{2(\lambda+2\epsilon)}}{\lambda(\lambda-2\epsilon)})\epsilon + \sqrt{2(\lambda+2\epsilon)}\frac{h}{\lambda}$$

where C is some real constant. $\nabla_M^{appro.} f$ and $\nabla_M^{real} f$ are the approximated gradient and the actual gradient of f respectively.

PROOF :

The actual gradient of f is given by:

$$\nabla_M^{real} f = ((\frac{g_{22}}{D})\frac{\partial f}{\partial x} - (\frac{g_{21}}{D})\frac{\partial f}{\partial y})\frac{\partial}{\partial x} + ((\frac{g_{11}}{D})\frac{\partial f}{\partial y} - (\frac{g_{12}}{D})\frac{\partial f}{\partial x})\frac{\partial}{\partial y} \tag{4.20}$$

where $D = g_{11}g_{22} - g_{12}g_{21}$ is the determinant of the Riemannian metric. The approximated gradient of f is given by:

$$\nabla_M^{appro.} f = (\frac{1}{\lambda}\widetilde{\frac{\partial f}{\partial x}})\frac{\partial}{\partial x} + (\frac{1}{\lambda}\widetilde{\frac{\partial f}{\partial y}})\frac{\partial}{\partial y} \tag{4.21}$$

where $\widetilde{\frac{\partial f}{\partial x}}$ and $\widetilde{\frac{\partial f}{\partial y}}$ are the approximation of $\frac{\partial f \circ \widetilde{\phi}}{\partial x}$ and $\frac{\partial f \circ \widetilde{\phi}}{\partial x}$ respectively. So,

$$\begin{aligned}
&||\nabla_M^{appro.} f - \nabla_M^{real} f||_M \\
&\leq ||\nabla_M^{appro.} f - (\frac{1}{\lambda}\frac{\partial f}{\partial x})\frac{\partial}{\partial x} + (\frac{1}{\lambda}\frac{\partial f}{\partial y})\frac{\partial}{\partial y}||_M + ||(\frac{1}{\lambda}\widetilde{\frac{\partial f}{\partial x}})\frac{\partial}{\partial x} + (\frac{1}{\lambda}\widetilde{\frac{\partial f}{\partial y}})\frac{\partial}{\partial y} - \nabla_M^{real} f||_M \\
&\leq \sqrt{2(\lambda+\epsilon)(\frac{4C\epsilon}{\lambda(\lambda-2\epsilon)})^2 + 2\epsilon(\frac{4C\epsilon}{\lambda(\lambda-2\epsilon)})^2} + \sqrt{2\frac{h^2}{\lambda^2}(\lambda+\epsilon) + 2\frac{h^2}{\lambda^2}\epsilon} \\
&= (\frac{4C\sqrt{2(\lambda+2\epsilon)}}{\lambda(\lambda-2\epsilon)})\epsilon + \sqrt{2(\lambda+2\epsilon)}\frac{h}{\lambda}
\end{aligned}$$

since $D \geq (\lambda-\epsilon)^2 - \epsilon^2$. Here, C is the upper bound of $\widetilde{\frac{\partial f}{\partial x}}$ and $\widetilde{\frac{\partial f}{\partial y}}$. Also, M is compact and so the function $|\frac{1}{\lambda}|$ is bounded. **Q.E.D.**

Therefore, the accuracy in the approximation of the surface gradient depends on the accuracy in the computation of the conformal parameterization and also the accuracy in the approximation of the partial derivatives. Specifically, it depends on how accurate the partial derivatives on R^2 are approximated and how closely the conformal factor λ could approximate the Riemannian metric (g_{ij}). Suppose the surface is a compact surface, the function $|\frac{1}{\lambda}|$ is bounded. So if the errors in both approximations are small, the error in approximating the surface gradient will also be small.

THEOREM 4.4.4.2 :

Let $D = g_{11}g_{22} - g_{12}g_{21}$. Assume that $|\widetilde{g}_{ij} - g_{ij}|$, $|\frac{\partial}{\partial x}(\frac{g_{ij}}{\sqrt{D}})|$ and $|\frac{\partial}{\partial y}(\frac{g_{ij}}{\sqrt{D}})|$ are all bounded by ϵ. Given $f : M \to R$. Suppose that the error in approximating the partial derivatives of $f \circ \widetilde{\phi}$ are bounded by h. We have:

$$|\Delta_M^{appro.} f - \Delta_M^{real} f| \leq 4C(\frac{1}{\sqrt{\lambda(\lambda - 2\epsilon)}} + \frac{2}{\lambda(\lambda - 2\epsilon)})\epsilon + \frac{h}{\lambda} \tag{4.22}$$

where C is some real constant. $\Delta_M^{appro.} f$ and $\Delta_M^{real} f$ are the approximated Laplacian and the actual Laplacian of f, respectively.

PROOF :

The actual Laplacian of f is given by: $\Delta_M^{real} f = \frac{1}{\sqrt{D}}\frac{\partial}{\partial x}(\frac{g_{22}}{\sqrt{D}})\frac{\partial f}{\partial x} - \frac{1}{\sqrt{D}}\frac{\partial}{\partial x}(\frac{g_{12}}{\sqrt{D}})\frac{\partial f}{\partial y} - \frac{1}{\sqrt{D}}\frac{\partial}{\partial y}(\frac{g_{21}}{\sqrt{D}})\frac{\partial f}{\partial x} + \frac{1}{\sqrt{D}}\frac{\partial}{\partial y}(\frac{g_{11}}{\sqrt{D}})\frac{\partial f}{\partial y} + \frac{g_{22}}{D}\frac{\partial^2 f}{\partial x^2} - \frac{2g_{12}}{D}\frac{\partial^2 f}{\partial x \partial y} + \frac{g_{11}}{D}\frac{\partial^2 f}{\partial y^2}$. The approximated Laplacian of f is given by: $\Delta_M^{appro.} f = \frac{1}{\lambda}\frac{\partial^2 f}{\partial x^2} + \frac{1}{\lambda}\frac{\partial^2 f}{\partial y^2}$. So,

$$
\begin{aligned}
&|\Delta_M^{appro.} f - \Delta_M^{real} f| \\
&\le |\Delta_M^{real} f - (\frac{1}{\lambda}\frac{\partial^2 f}{\partial x^2} + \frac{1}{\lambda}\frac{\partial^2 f}{\partial y^2})| + |(\frac{1}{\lambda}\frac{\partial^2 f}{\partial x^2} + \frac{1}{\lambda}\frac{\partial^2 f}{\partial y^2}) - \Delta_M^{appro.} f| \\
&\le (C|\frac{g_{11}}{D} - \frac{1}{\lambda}| + C|\frac{g_{22}}{D} - \frac{1}{\lambda}| + \frac{2C\epsilon}{D} + \frac{4C\epsilon}{\sqrt{D}}) + \frac{2h}{\lambda} \\
&\le 2C\frac{\lambda(\lambda+\epsilon) - \lambda(\lambda - 2\epsilon)}{\lambda^2(\lambda - 2\epsilon)} + \frac{2C\epsilon}{\lambda(\lambda - 2\epsilon)} + \frac{4C\epsilon}{\sqrt{\lambda(\lambda-\epsilon)}} + \frac{2h}{\lambda} \\
&\le C(\frac{4}{\sqrt{\lambda(\lambda - 2\epsilon)}} + \frac{8}{\lambda(\lambda - 2\epsilon)})\epsilon + \frac{h}{\lambda} \\
&= 4C(\frac{1}{\sqrt{\lambda(\lambda - 2\epsilon)}} + \frac{2}{\lambda(\lambda - 2\epsilon)})\epsilon + \frac{h}{\lambda}
\end{aligned}
$$

since $D \ge (\lambda - \epsilon)^2 - \epsilon^2$.

Here, C is the upper bound of $\widetilde{\frac{\partial f}{\partial x}}$, $\widetilde{\frac{\partial f}{\partial y}}$, $\widetilde{\frac{\partial^2 f}{\partial x^2}}$ and $\widetilde{\frac{\partial^2 f}{\partial y^2}}$. **Q.E.D.**

We see that the accuracy in the approximation of the Laplacian depends on the accuracy in the computation of the conformal parameterization and the upper bound of the partial derivatives of $\frac{g_{ij}}{\sqrt{D}}$. These conditions are well satisfied if the approximation of the conformal parameterization is accurate enough. $\frac{g_{ij}}{\sqrt{D}}$ is close to 1 when $i = j$ and is close to 0 if $i \neq j$. The conformal parameterization is computed as the integral of the holomorphic one form $\omega + i\omega^*$ that preserves the harmonicity. Therefore, $\frac{g_{ij}}{\sqrt{D}}$ are smooth and its partial derivatives are close to 0.

In general, one can easily show that the approximated covariant derivatives converges to the actual ones when the approximation of the conformal parameterization and the approximation of the partial derivatives are accurate enough. It can be explained by the following claim:

THEOREM 4.4.4.3 :

Let $X = X_1\frac{\partial}{\partial x} + X_2\frac{\partial}{\partial y}$ and $Y = Y_1\frac{\partial}{\partial x} + Y_2\frac{\partial}{\partial y}$ be two vector fields on the surface M. Suppose that X_i and Y_i are bounded by C. Suppose that the errors in approximating the partial derivatives of $X_i \circ \widetilde{\phi}$ and $Y_i \circ \widetilde{\phi}$ are bounded by h. We have:

$$||\nabla_X^{appro.}Y - \nabla_X^{real}Y||_M \leq [8C^2 A\sqrt{2(\lambda + 2\epsilon)}]\epsilon + 2C\sqrt{2(\lambda + 2\epsilon)}h$$

where A is a real constant. $\nabla_X^{appro.}Y$ and $\nabla_X^{real}Y$ are the approximated covariant derivative and the actual covariant derivative of Y in the direction X respectively.

PROOF :

The actual covariant derivative is: $\nabla_X^{real}Y = (X_1\frac{\partial Y_1}{\partial x} + X_2\frac{\partial Y_1}{\partial y} + X_1Y_1\Gamma_{11}^1 + X_1Y_2\Gamma_{12}^1 + X_2Y_1\Gamma_{21}^1 + X_2Y_2\Gamma_{22}^1)\frac{\partial}{\partial x} + (X_1\frac{\partial Y_2}{\partial x} + X_2\frac{\partial Y_2}{\partial y} + X_1Y_1\Gamma_{11}^2 + X_1Y_2\Gamma_{12}^2 + X_2Y_1\Gamma_{21}^2 + X_2Y_2\Gamma_{22}^2)\frac{\partial}{\partial y}$. We write he approximated covariant derivative as: $\nabla_X^{appro.}Y = (X_1\widetilde{\frac{\partial Y_1}{\partial x}} + X_2\widetilde{\frac{\partial Y_1}{\partial y}} + X_1Y_1\widetilde{\Gamma_{11}}^1 + X_1Y_2\widetilde{\Gamma_{12}}^1 + X_2Y_1\widetilde{\Gamma_{21}}^1 + X_2Y_2\widetilde{\Gamma}_{22}^1)\frac{\partial}{\partial x} + (X_1\widetilde{\frac{\partial Y_2}{\partial x}} + X_2\widetilde{\frac{\partial Y_2}{\partial y}} + X_1Y_1\widetilde{\Gamma}_{11}^2 + X_1Y_2\widetilde{\Gamma}_{12}^2 + X_2Y_1\widetilde{\Gamma}_{21}^2 + X_2Y_2\widetilde{\Gamma}_{22}^2)\frac{\partial}{\partial y}$, where $\widetilde{\Gamma}_{ij}^k$ and $\widetilde{\frac{\partial Y_i}{\partial x_i}}$ are the approximations of Γ_{ij}^k and $\frac{\partial Y_i}{\partial x_i}$. It can be shown easily that $|\widetilde{\Gamma}_{ij}^k - \Gamma_{ij}^k| < A\epsilon$ for some fixed positive constant A. Therefore,

$$
\begin{aligned}
& ||\nabla_X^{appro.} Y - \nabla_X^{real} Y||_M \\
& \leq ||\nabla_X^{real} Y - (X_1 \frac{\partial Y_1}{\partial x} + X_2 \widetilde{\frac{\partial Y_1}{\partial y}} + X_1 Y_1 {\Gamma_{11}}^1 + X_1 Y_2 {\Gamma_{12}}^1 \\
& + X_2 Y_1 {\Gamma_{21}}^1 + X_2 Y_2 \Gamma_{22}^1) \frac{\partial}{\partial x} \\
& - (X_1 \widetilde{\frac{\partial Y_2}{\partial x}} + X_2 \widetilde{\frac{\partial Y_2}{\partial y}} + X_1 Y_1 \Gamma_{11}^2 + X_1 Y_2 \Gamma_{12}^2 + X_2 Y_1 \Gamma_{21}^2 + X_2 Y_2 \Gamma_{22}^2) \frac{\partial}{\partial y} ||_M \\
& + ||(X_1 \widetilde{\frac{\partial Y_1}{\partial x}} + X_2 \widetilde{\frac{\partial Y_1}{\partial y}} + X_1 Y_1 {\Gamma_{11}}^1 + X_1 Y_2 {\Gamma_{12}}^1 + X_2 Y_1 {\Gamma_{21}}^1 + X_2 Y_2 \Gamma_{22}^1) \frac{\partial}{\partial x} \\
& + (X_1 \widetilde{\frac{\partial Y_2}{\partial x}} + X_2 \widetilde{\frac{\partial Y_2}{\partial y}} + X_1 Y_1 \Gamma_{11}^2 + X_1 Y_2 \Gamma_{12}^2 + X_2 Y_1 \Gamma_{21}^2 \\
& + X_2 Y_2 \Gamma_{22}^2) \frac{\partial}{\partial y} - \nabla_X^{appro.} Y||_M \\
& \leq ||(X_1 (\widetilde{\frac{\partial Y_1}{\partial x}} - \frac{\partial Y_1}{\partial x}) + X_2 (\widetilde{\frac{\partial Y_1}{\partial y}} - \frac{\partial Y_1}{\partial y})) \frac{\partial}{\partial x} \\
& + (X_1 (\widetilde{\frac{\partial Y_2}{\partial x}} - \frac{\partial Y_2}{\partial x}) + X_2 (\widetilde{\frac{\partial Y_2}{\partial y}} - \frac{\partial Y_2}{\partial y})) \frac{\partial}{\partial y} ||_M \\
& + ||(X_1 Y_1 (\widetilde{\Gamma_{11}}^1 - {\Gamma_{11}}^1) + X_1 Y_2 (\widetilde{\Gamma_{12}}^1 - {\Gamma_{12}}^1) \\
& + X_2 Y_1 (\widetilde{\Gamma_{21}}^1 - {\Gamma_{21}}^1) + X_2 Y_2 ((\widetilde{\Gamma_{22}}^1 - {\Gamma_{22}}^1))) \frac{\partial}{\partial x} \\
& + (X_1 Y_1 (\widetilde{\Gamma_{11}}^2 - {\Gamma_{11}}^2) + X_1 Y_2 (\widetilde{\Gamma_{12}}^2 - {\Gamma_{12}}^2) \\
& + X_2 Y_1 (\widetilde{\Gamma_{21}}^2 - {\Gamma_{21}}^2) + X_2 Y_2 ((\widetilde{\Gamma_{22}}^2 - {\Gamma_{22}}^2))) \frac{\partial}{\partial y} ||_M \\
& \leq [8C^2 A \sqrt{2(\lambda + 2\epsilon)}]\epsilon + 2C\sqrt{2(\lambda + 2\epsilon)} h
\end{aligned}
$$

Here, C is the upper bound of X_i and Y_i. **Q.E.D.**

Again, the numerical accuracy of the covariant derivatives in general depends on the accuracy in the computation of the conformal parameterization and also the accuracy in the approximation of the partial derivatives. For detailed proof of the theorems, please refer to [87].

4.5 Experimental Examples

4.5.1 Image denoising on the surface

With the advance of the 3D acquisition systems, images on the surface can be effectively captured and stored as digital data. Nevertheless, noise is inevitably introduced during the transmission process. Therefore, it is of interest to look for an efficient algorithm to denoise the digital image defined on the surface. It has also been widely studied by different research groups [88][89][90][91]. On R^2, total variation (TV) denoising has been extensively used for image restoration that well-preserves edges [55]. It is then natural to extend the 2D TV denoising model to surfaces. With the conformal parameterization, the TV image denoising model can be easily extended.

On R^2, the TV model reads:

$$E_{TV}(u) = \int_D [|\nabla u| + (u-f)^2] dxdy, \tag{4.23}$$

where $f : D \subseteq R^2 \to R$ is the noisy gray-level image in R^2. We will look for a minimizer $u : D \to R$ of E_{TV} to approximate the original clean image. The Euler-Lagrange equation of it is:

$$\frac{du}{dt} = div(\frac{\nabla u}{|\nabla u|}) - 2(u-f). \tag{4.24}$$

The TV model can also be modified to denoise the color image on R^2 [56]:

$$E_{TVcolor}(\vec{u}) = \int_D [\sqrt{\sum_{i=1}^{3} |\nabla u_i|^2 + |\vec{u} - \vec{f}|^2}] dxdy \tag{4.25}$$

where $\vec{f} = (f_1, f_2, f_3) : D \to R^2$ is the noisy color image; $\vec{u} = (u_1, u_2, u_3) : D \to R^2$ is the approximation of the original clean color image. The minimizer of $E_{TVcolor}$ can be found via its Euler-Lagrange equation:

$$\frac{du_i}{dt} = div(\frac{\nabla u_i}{\sqrt{\sum_{i=1}^{3} |\nabla u_i|^2}}) - 2(u_i - f_i) \text{ for } i = 1, 2, 3. \tag{4.26}$$

These two models can be extended easily to the surfaces. On the surface, the gray-level TV image denoising model reads:

$$E_{TV}^S(u) = \int_S [||\nabla_S u||_S + |u - f|^2] dS, \tag{4.27}$$

where $f : S \to R$ is a gray-level image defined on the surface. Replacing the Eulcidean differential operators by the modified differential operators in (20), we get the Euler-Lagrange equation of E_{TV}^S:

$$\begin{aligned} \frac{du}{dt} &= div_S(\frac{\nabla_S u}{||\nabla_S u||_S}) - 2(u - f) \text{ or} \\ \frac{du \circ \phi}{dt} &= \frac{1}{\lambda} div(\sqrt{\lambda}\frac{\nabla u}{|\nabla u|}) - 2(u \circ \phi - f) \text{ on the parameter domain,} \end{aligned} \tag{4.28}$$

where ϕ is the conformal parameterization of S.

The color TV image denoising model can also be extended to the surface:

$$E_{TVcolor}^S = \int_S [\sqrt{\sum_{i=1}^{3} ||\nabla_S u_i||_S^2} + ||\vec{u} - \vec{f}||_S^2] dS \tag{4.29}$$

where $\vec{f} = (f_1, f_2, f_3) : S \to R$ is a color image defined on the surface. By replacing the Euclidean differential operator by the manifold differential operator, we get the Euler-Lagrange equation of $E^S_{TVcolor}$:

$$\frac{du_i}{dt} = div_S\left(\frac{\nabla_S u_i}{\sqrt{\sum_{i=1}^3 ||\nabla_S u_i||_S^2}}\right) - 2(u_i - f_i) \text{ for } i = 1,2,3 \text{ or}$$

$$\frac{du_i \circ \phi}{dt} = \frac{1}{\lambda} div\left(\sqrt{\lambda}\frac{\nabla u_i \circ \phi}{\sqrt{\sum_{i=1}^3 |\nabla u_i \circ \phi|^2}}\right) - 2\lambda(u_i \circ \phi - f_i \circ \phi) \text{ for } i = 1,2,3. \tag{4.30}$$

on the parameter domain.

The two energy functions of the denoising models can be minimized by steepest descent algorithm. Notice that the corresponding Euler-Lagrange equation on the parameter domain is very similar to the 2D version, except for a scaler multiplication of the conformal factor. These two denoising models can effectively denoise the gray-level and color image defined on the surface, which well-preserves the edges. Figure 4.4 illustrates the TV color image denoising on a dog surface. The top shows the noisy color image on the dog surface. The denoised color image is shown at the bottom. As shown in the figure, the noise are mostly removed and the reconstructed surface is significantly improved.

4.5.2 Denoising/Smoothing of Riemann surface

Riemann surfaces are usually obtained by laser scanning or other medical image generation methods such as MRI devices, CT and so on. The surfaces are usually represented as triangular meshes. During the construction process, geometric noise is inevitably introduced. Therefore, surface denoising/smoothing, which adjusts the vertices positions so that a smoother surface can be obtained, has become a very important research topic.

Here, we applied the TV denoising technique on the Riemann surface to de-

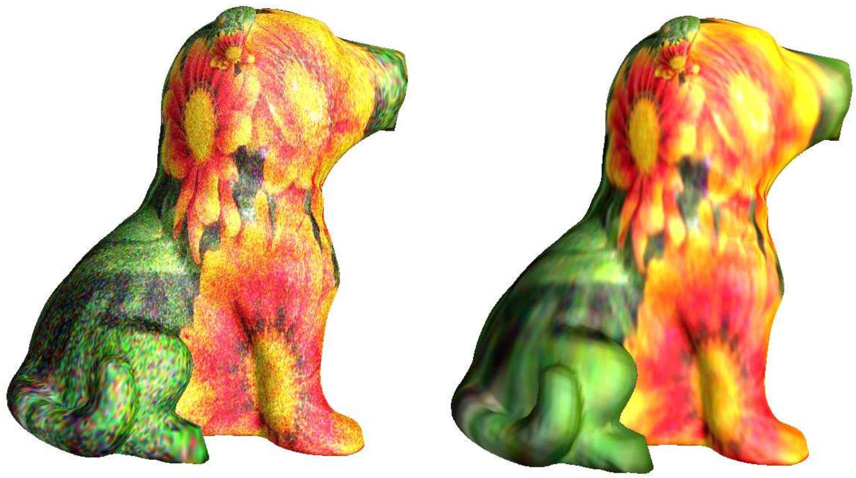

(A) (B)

Figure 4.4: Illustration of the TV image denoising on a dog surface. With covariant derivatives, the 2D TV color image denoising model is extended to the 3D Riemann surface. (A) shows the noisy image on the dog surface. (B) shows the denoised image on the surface. As shown in the figure, the noise are mostly removed and the reconstructed surface is significantly improved.

noise the noisy surface S. Given a conformal parameterization $\phi : R^2 \to S$. Let $\overrightarrow{\phi}(x,y) = (X(x,y), Y(x,y), Z(x,y))$. The functions X, Y and Z can be regarded as functions defined on the surface S. If S is a smooth surface, X, Y and Z are also smooth. By extending the TV denoising technique to the 3D Riemann surface, we can smooth the surface by minimizing the following energy functionals:

$$E(\overrightarrow{\Psi}) = \int_S ||\nabla_S \overrightarrow{\Psi}||_S dS + \mu|\overrightarrow{\Psi} - \overrightarrow{\phi}|^2$$

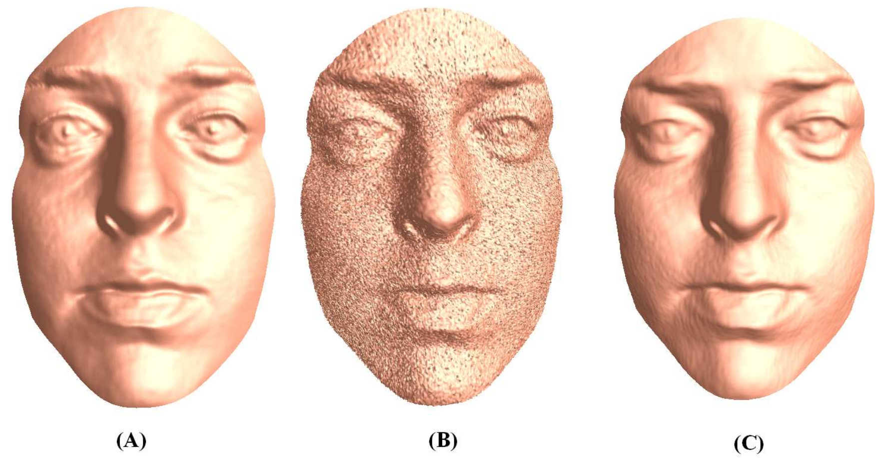

Figure 4.5: Illustration of the TV surface denoising on a human face. With covariant derivatives, the 2D TV image denoising model is extended to 3D Riemann surfaces. (A) shows the original surface of a human face. In (B), the random gaussian noise is added to the face. (C) shows the denoised/smoothed surface. As shown in (C), the reconstructed surface approximates the original surface very well, except for a little bit smoothing.

Or equivalently, we are minimizing the following three energy functionals:

$$
\begin{aligned}
E(\widetilde{X}) &= \int_S ||\nabla_S \widetilde{X}||_S dS + \mu(\widetilde{X} - X)^2; \\
E(\widetilde{Y}) &= \int_S ||\nabla_S \widetilde{Y}||_S dS + \mu(\widetilde{Y} - Y)^2; \\
E(\widetilde{Z}) &= \int_S ||\nabla_S \widetilde{Z}||_S dS + \mu(\widetilde{Z} - Z)^2
\end{aligned}
$$

The Euler Lagrange equations of them are:

$$
\begin{aligned}
\frac{\partial \widetilde{X}}{\partial t} &= \nabla_S \cdot (\frac{\nabla_S \widetilde{X}}{||\nabla_S \widetilde{X}||_S}) + 2\mu(\widetilde{X} - X); \\
\frac{\partial \widetilde{Y}}{\partial t} &= \nabla_S \cdot (\frac{\nabla_S \widetilde{Y}}{||\nabla_S \widetilde{Y}||_S}) + 2\mu(\widetilde{Y} - Y); \\
\frac{\partial \widetilde{Z}}{\partial t} &= \nabla_S \cdot (\frac{\nabla_S \widetilde{Z}}{||\nabla_S \widetilde{Z}||_S}) + 2\mu(\widetilde{Z} - Z)
\end{aligned}
$$

With the conformal parameterization ϕ, we can solve these partial differential equations on the 2D domain with the following three equations:

$$\begin{aligned}
\frac{\partial \widetilde{X} \circ \phi}{\partial t} &= \frac{1}{\lambda} \nabla \cdot (\sqrt{\lambda} \frac{\nabla \widetilde{X} \circ \phi}{||\nabla \widetilde{X} \circ \phi + \epsilon||}) + 2\mu(\widetilde{X} \circ \phi - X \circ \phi); \\
\frac{\partial \widetilde{Y} \circ \phi}{\partial t} &= \frac{1}{\lambda} \nabla \cdot (\sqrt{\lambda} \frac{\nabla \widetilde{Y} \circ \phi}{||\nabla \widetilde{Y} \circ \phi + \epsilon||}) + 2\mu(\widetilde{Y} \circ \phi - Y \circ \phi); \\
\frac{\partial \widetilde{Z} \circ \phi}{\partial t} &= \frac{1}{\lambda} \nabla \cdot (\sqrt{\lambda} \frac{\nabla \widetilde{Z} \circ \phi}{||\nabla \widetilde{Z} \circ \phi + \epsilon||}) + 2\mu(\widetilde{Z} \circ \phi - Z \circ \phi)
\end{aligned}$$

where λ is the conformal factor of ϕ. ϵ is a small regularization constant to handle with the case when $||\nabla X \circ \phi|| = 0$, $||\nabla Y \circ \phi|| = 0$ or $||\nabla Z \circ \phi|| = 0$. In practice, we usually take $\epsilon = 0.01$. We note that the Euler Lagrange equations are very similar to well-known 2D TV denoising equation, except for the scalar multiplication of the conformal factor λ. Therefore, we can solve the problem by simple modification of the existing 2D TV denoising solver.

Figure 4.5 illustrates the idea of surface denoising/smoothing on a human face with our method. Figure 4.5(A) shows the original human face surface. In Figure 4.5(B), the random gaussian noise is added to the surface of the human face. In Figure 4.5(C), we applied the method we described to denoise the surface. The parameter chosen are: $\mu = 5$, $\epsilon = 0.01$ and the number of iterations is 50. Note that the denoised surface approximates the original surface well, except for a little bit smoothing.

The intuitive meaning of including the conformal factor λ into the TV model is that it fixes the distortion caused by the stretching. Basically, the TV model denoises the data by smoothing out the high frequency (rapid jump) region. Due the the stretching of the conformal parameterization, the low frequency regions might become the high frequency region in the parameter domain, whereas the high frequency regions become the low frequency region in the parameter domain. As a result, the low frequency regions will be smoothed out and a wrong denoising result will be obtained.

4.5.3 Texture extraction on the surface

The extraction of features on surfaces has been studied widely [92] and has found various applications in different areas of research. For example, texture extraction is an important process in texture synthesis to transfer textures from one surface to another. In human brain mapping, the feature extraction technique is used to detect important anatomical features on the brain surface to study brain diseases. In this section, we will describe an effective variational method for feature extraction, using the Chan-Vese segmentation model on the surface.

The algorithm consists of two steps. Firstly, we compute the feature intensity on the surface, which encodes the feature information. The feature intensity $I_f : S \to R$ is a function on S defined as:

$$I_f(\phi(p)) = |\phi(p) - \phi_{smooth}(p)|^2, \tag{4.31}$$

where $\phi_{smooth} : R^2 \to S$ represents the smoothed surface of S, using the TV surface smoothing algorithm introduced in VI(B). Specifically, ϕ_{smooth} is obtained iteratively using the gradient descent algorithm to minimize the energy functional in the TV surface smoothing model (See equation). The feature intensity I_f effectively represents the feature information on the surface.

After computing the feature intensity I_f, the second step is to extract the feature with the Chan-Vese segmentation model on the surface, using I_f as the intensity. We proceed to look for $\psi : S \to R$ that minimizes the following energy functional:

$$F(c_1, c_2, \psi) = \int_S (I_f - c_1)^2 H(\psi) dS + \int_S (I_f - c_2)^2 (1 - H(\psi)) dS + \nu \int_S |\nabla_S H(\psi)| dS \tag{4.32}$$

The Euler Lagrange equation is:

$$\begin{aligned} \frac{\partial \psi}{\partial t} &= \lambda \delta(\psi)[\ \nu div_S(\frac{\nabla_S \psi}{||\nabla_S \psi||_S}) - (I_f - c_1)^2 - (I_f - c_2)^2] \text{ or} \\ \frac{\partial \psi \circ \phi}{\partial t} &= \lambda \delta(\psi \circ \phi)[\nu \frac{1}{\lambda} div(\sqrt{\lambda} \frac{\nabla \psi \circ \phi}{|\nabla \psi \circ \phi|}) - (I_f \circ \phi - c_1)^2 - (I_f \circ \phi - c_2)^2], \end{aligned} \tag{4.33}$$

on the parameter domain, where:

$$\begin{aligned} c_1 &= \frac{\int_D I_f \circ \phi(x,y) H(\psi \circ \phi(x,y)) \lambda(x,y) dxdy}{\int_D H(\psi \circ \phi(x,y)) \lambda(x,y) dxdy} \\ c_1 &= \frac{\int_D I_f \circ \phi(x,y)(1 - H(\psi \circ \phi(x,y))) \lambda(x,y) dxdy}{\int_D (1 - H(\psi \circ \phi(x,y))) \lambda(x,y) dxdy} \end{aligned} \tag{4.34}$$

The zero level set of the minimizer $\psi : S \to R$ encloses the boundary of the feature on the surface effectively. To illustrate the idea, we apply the algorithm to extract the Chinese character on the cylinder. Figure 4.6(left) shows the a surface with some texture (chinese character) on it. In Figure 4.6(right), we applied our proposed algorithm to extract the feature. The intensity is defined as the distance between the original surface and the smoothed out surface. As shown in the figure, the initial contour (green) evolves to the final contour (blue) that encloses the texture in few iterations.

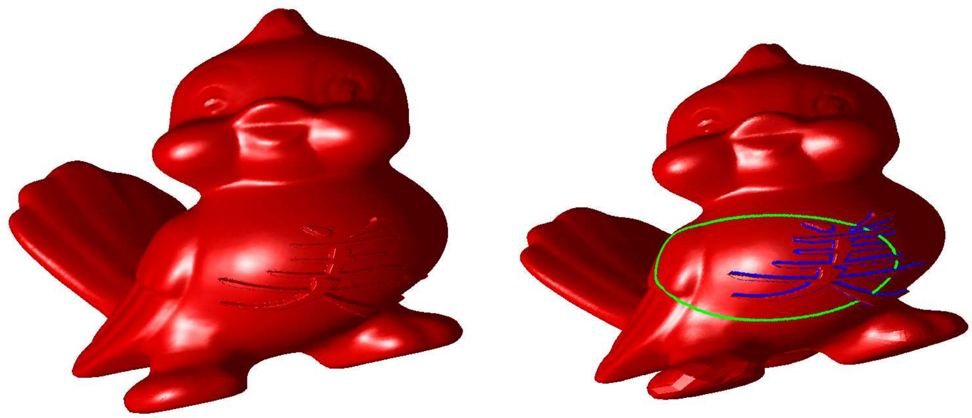

Figure 4.6: Illustration of the extraction of texture on the surface. With covariant derivatives, the 2D Chan Vese (CV) segmentation model is extended to 3D Riemann surfaces. The left shows the a bird surface with some texture (chinese character) on it. On the right, we applied the CV segmentation model to extract the texture. The intensity is defined as the distance between the original surface and the smoothed out surface. As shown in the figure, the initial contour (green) evolves to the final contour (blue) that encloses the texture in few iterations.

4.5.4 Inpainting surface holes

3D surface model are usually obtained from range scanners. Very often, surfaces obtained from range scanner have holes and so resulting in incomplete surface meshes. This may be due to low reflectance, occlusion, scanner placement, inadequate coverage of the object and so on. Recently, reseachers have been interested in inpainting surface holes to reconstruct the incomplete surface and it has become an important research topic [64][93]. In this section, we present an algorithm to solve this problem which involves solving PDEs on the surface. Inpainting can be regarded as a process of interpolating data on the occluded region from the known data on its neighborhood. Our algorithm is an extension of 2D image inpainting. To inpaint an occlude 2D digital image, we can fill in the missing

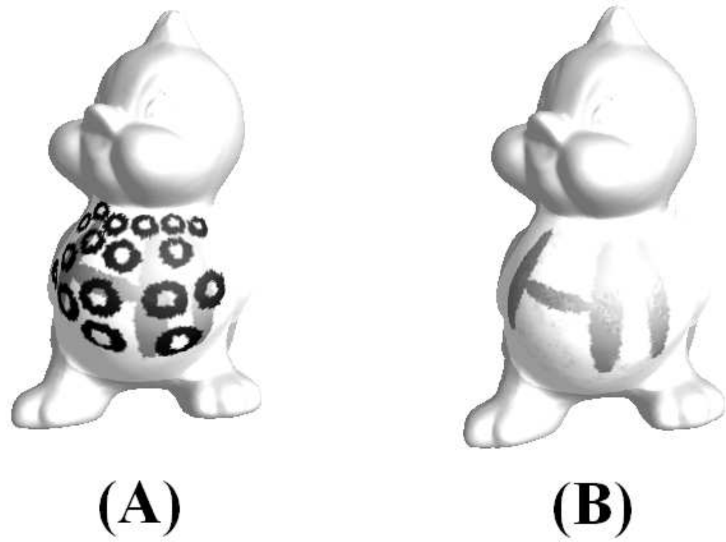

Figure 4.7: A simple example that illustrates image inpainting on the bird surface. We extend the 2D image inpainting model to 3D surface (A) shows some simple textures on the bird surface with occlusion. We applied the image inpainting model to inpaint the image. The black region is the inpainting domain. (B) shows the inpainted result.

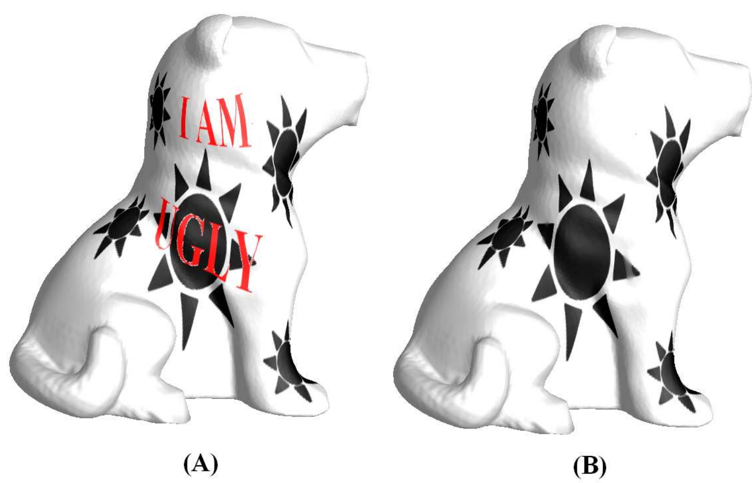

Figure 4.8: "I am not ugly! Please remove the bad words on my body." Illustration of image inpainting on the dog surface. We extend the 2D image inpainting model to 3D surface to remove unwanted words on the dog surface. (A) shows a dog surface with some unwanted words on it. We applied the image inpainting model to inpaint the image. (B) shows the inpainted result. As shown in the figure, the words are successfully removed.

region by solving the Perona-Malik diffusion model that reads:

$$\begin{cases} \frac{\partial u}{\partial t} = div(g(|\nabla u|)\nabla u) & \text{on } D; \\ u^0 = v & \text{on } D^c. \end{cases}$$

where D is the occluded region; $v : D^c \to R$ is the original image with occlusion; u is the approximated (inpainted) image; $g : R \to R$ is an increasing function such that $g(0) = 0$ and $g(\infty) = \infty$. Note that if we replace g by $\frac{1}{\nabla u}$, we get the familiar TV smoothing model. The TV smoothing model is well-known to be preserving edges. The major drawback of it is that it does not restore well a single object when its disconnected remaining parts are separated far apart by the inpainting domain. In order to solve this problem, we add the function g into the diffusion model which enhances the diffusion across the boundary of the inpainting domain. Sometimes, it may be more beneficial to let g depend on the curvature $\kappa = div(\frac{\nabla u}{|\nabla u|})$ and so the model depends on the geometry of the image. Here in our application to inpaint surface holes, we have found that letting g depend on the isophote $|\nabla u|$ is already good enough to get a reasonably good result.

The 2D inpainting model can be easily extended to surfaces by using our algorithm. Figure 4.7 shows a simple example that illustrates image inpainting on the bird surface. We extend the 2D image inpainting model to 3D surface (A) shows some simple textures on the bird surface with occlusion. We applied the image inpainting model to inpaint the image. The black region is the inpainting domain. (B) shows the inpainted result. Figure 4.8 shows the image inpainiting result on the dog surface. To inpaint surface holes, we apply the image inpainting model on the surface S. Again, we can regard $X : S \to R$, $Y : S \to R$ and $Z : S \to R$ as three smooth functions defined on S. Given the conformal parameterization

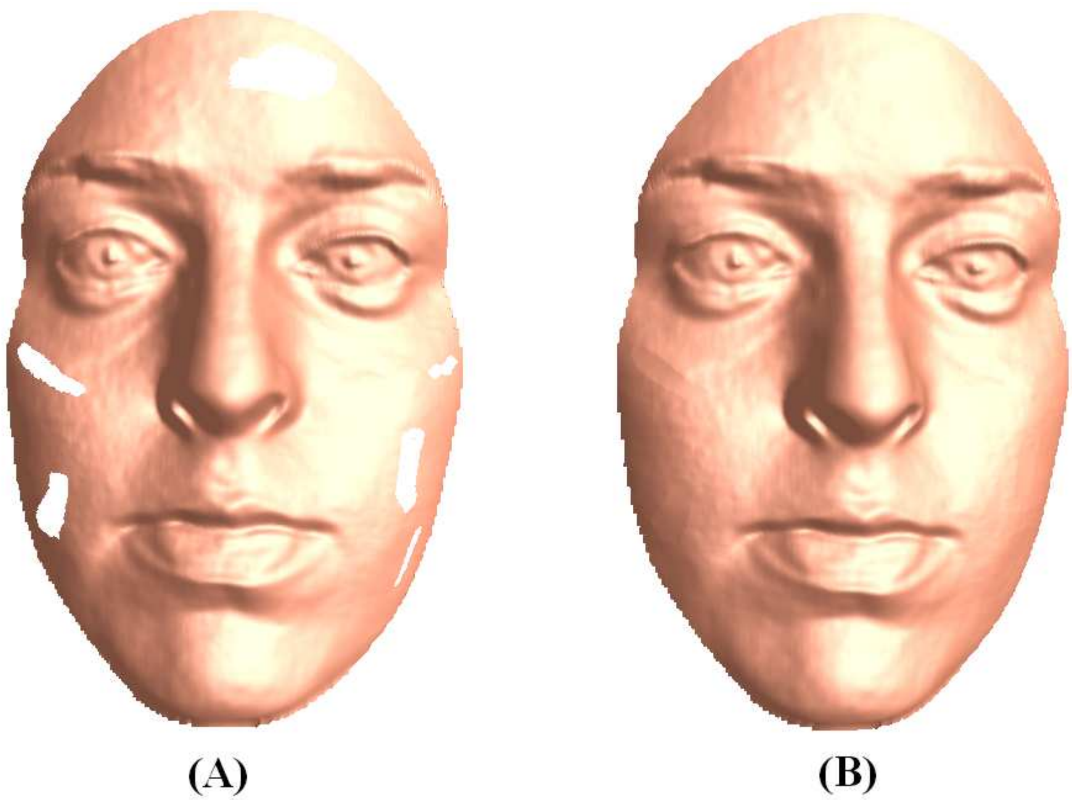

Figure 4.9: Illustration of the algorithm for inpainting surface holes. We extend the 2D image inpainting model to 3D surface to fill in surface holes. (A) shows a human face with several holes on it. We applied the surface holes inpainting model to inpaint the occlusion region on the surface. (B) shows the inpainted result. As shown in the figure, the occlusion can be filled reasonably well, which results in a smooth surface.

$\phi : R^2 \to S$ of S, we can have the following surface holes inpainting model:

$$\begin{cases} \frac{\partial X^t}{\partial t} = div_S(g(||\nabla X||_S)\nabla_S X) & \text{on } D_S; \\ \frac{\partial Y^t}{\partial t} = div_S(g(||\nabla Y||_S)\nabla_S Y) & \text{on } D_S; \\ \frac{\partial Z^t}{\partial t} = div_S(g(||\nabla Z||_S)\nabla_S Z) & \text{on } D_S; \\ X^0 = X_v & \text{on } D_S^c; \\ Y^0 = Y_v & \text{on } D_S^c; \\ Z^0 = Z_v & \text{on } D_S^c; \end{cases}$$

where D_S is the occluded region on the surface; X_v, Y_v, Z_v are the X, Y, Z coordinates of the original surface mesh with occlusion. We can solve this system of partial differential equations iteratively on the parameter domain:

$$\begin{cases} \frac{\partial X^t \circ \phi}{\partial t} = \frac{1}{\lambda} div(g(\sqrt{\lambda}|\nabla X \circ \phi|)\nabla X \circ \phi) & \text{on } \phi^{-1}(D_S); \\ \frac{\partial Y^t \circ \phi}{\partial t} = \frac{1}{\lambda} div(g(\sqrt{\lambda}|\nabla Y \circ \phi|)\nabla Y \circ \phi) & \text{on } \phi^{-1}(D_S); \\ \frac{\partial Z^t \circ \phi}{\partial t} = \frac{1}{\lambda} div(g(\sqrt{\lambda}|\nabla Z \circ \phi|)\nabla Z \circ \phi) & \text{on } \phi^{-1}(D_S); \\ X^0 \circ \phi = X_v \circ \phi & \text{on } \phi^{-1}(D_S^c); \\ Y^0 \circ \phi = Y_v \circ \phi & \text{on } \phi^{-1}(D_S^c); \\ Z^0 \circ \phi = Z_v \circ \phi & \text{on } \phi^{-1}(D_S^c); \end{cases}$$

To illustrate the idea, we test our algorithm to fill in the holes on a human face. Figure 4.9(A) shows a human face with several holes on it. We applied the surface holes inpainting model to inpaint the occlusion region on the surface. Figure 4.9(B) shows the inpainted result. As shown in the figure, the occlusion can be filled reasonably well, which results in a smooth surface.

4.5.5 Fluid Flow on Surfaces

In this subsection, we illustrate how we can apply the algorithm to simulate fluid flow on surfaces with arbitrary topologies. This is done by projecting the Navier-Stokes equation on the surface onto the 2D parameter domain using the conformal parameterization. We then use the stable fluid solver [65, **?**] on the 2-D domain to solve the problem.

On $\mathbb{R}^2$, fluid flow is governed by the Navier-Stokes equation. For incompressible fluid flow, we have the following (*):

$$\frac{\partial \mathbf{u}}{\partial t} = -(\mathbf{u} \cdot \bigtriangledown)\mathbf{u} + v\nabla^2\mathbf{u} + \mathbf{f} \tag{4.35}$$

and

$$\nabla \cdot \mathbf{u} = 0 \text{ } (\textbf{imcompressibility}) \tag{4.36}$$

where $\mathbf{u} = (u^1, u^2)$ is the fluid's velocity, v is the viscosity and $\mathbf{f} = (f^1, f^2)$ are external forces.

We can simulate the fluid flow as follow: we first use the stable fluid solver to solve (*). Then update the position of the fluid by $\mathbf{x}^{new} = \mathbf{x}^{old} + \mathbf{u}dt$, where $\mathbf{x}^{new}$ = updated position of the fluid particle and $\mathbf{x}^{old}$= previous position of the fluid particle.

To simulate fluid flow on the Riemann surface, we have to modify the 2D Navier-Stokes equation by the manifold version of gradient and lapacian. Replacing the gradient and laplacian by the manifold version of gradient and laplacian, we get the corresponding Navier-Stokes equation for the Riemann surface S:

$$\frac{\partial \mathbf{u}}{\partial t} = -(\mathbf{u} \cdot \nabla_S)\mathbf{u} + v\triangle_S\mathbf{u} + \mathbf{f} \tag{4.37}$$

where $\mathbf{u}$ is the velocity field which is a vector field on S.

Let ϕ be the conformal parametrization of S and $\mathbf{w} = \mathbf{u} \circ \phi$. We have:

$$\frac{\partial \mathbf{w}}{\partial t} = -\frac{1}{\lambda}(\mathbf{w} \cdot \bigtriangledown)\mathbf{w} + \frac{1}{\lambda} v \triangle \mathbf{w} + \mathbf{f} \tag{4.38}$$

We can next use the Stable Fluid Solver introduced by Stam to solve the Navier-Stokes equation. We describe the algorithm as follow:

Step 1 : (**Adding force**) We solve: $\frac{\partial \mathbf{w_1}}{\partial t} = \mathbf{f}$. The iterative scheme is: $\mathbf{w}_1 = \mathbf{w}_0 + dt\mathbf{f}$

Step 2 : (**Diffusion equation**) We solve: $\frac{\partial \mathbf{w_2}}{\partial t} = \frac{1}{\lambda} v \triangle \mathbf{w}_1$. We use a simple implicit solver to get the iterative scheme: $(I - dt\frac{1}{\lambda} v \triangle)\mathbf{w}_2 = \mathbf{w}_1$.

Step 3 : (**Advection equation**) We solve: $\frac{\partial \mathbf{w_3}}{\partial t} = -\frac{1}{\lambda}(\mathbf{w}_2 \cdot \bigtriangledown)\mathbf{w}_3$. We use a semi-Lagrangian to get an iterative scheme: $\mathbf{w}_3 = \mathbf{w}_2(\mathbf{x} - dt\frac{1}{\lambda}\mathbf{w_2}(\mathbf{x}))$

Step 4 : (**Projection**) We project $\mathbf{w}$ onto its imcompressible (divergence free) component. For this, we first solve the Poisson equation

$$\triangle \varphi = \nabla \cdot \mathbf{w}_3 \tag{4.39}$$

We then update: $\mathbf{w}_4 = \mathbf{w}_3 - \frac{1}{\lambda}\nabla\varphi$. Update $\mathbf{w} = \mathbf{w}_4$.

Step 5 : (**Update fluid position**) Update $\mathbf{x}$ by $\mathbf{x}^{new} = \mathbf{x}^{old} + \mathbf{w} \cdot (\frac{\partial}{\partial x}, \frac{\partial}{\partial y})dt$

As an example, we simulate the snow flowing down the surface based on the Navier-Stokes equation in Figure 4.10. Figure 4.11(A) shows a simulation of fluid flow on a bunny surface by solving Navier-Stoker's equation at different iterations. A circular force field is applied on the surface. Figure 4.11(B) shows another example of fluid flow on a bird surface. Figure 4.11(C) shows how solving surface fluid flow by Navier-Stoke's equation can be applied for surface decoration

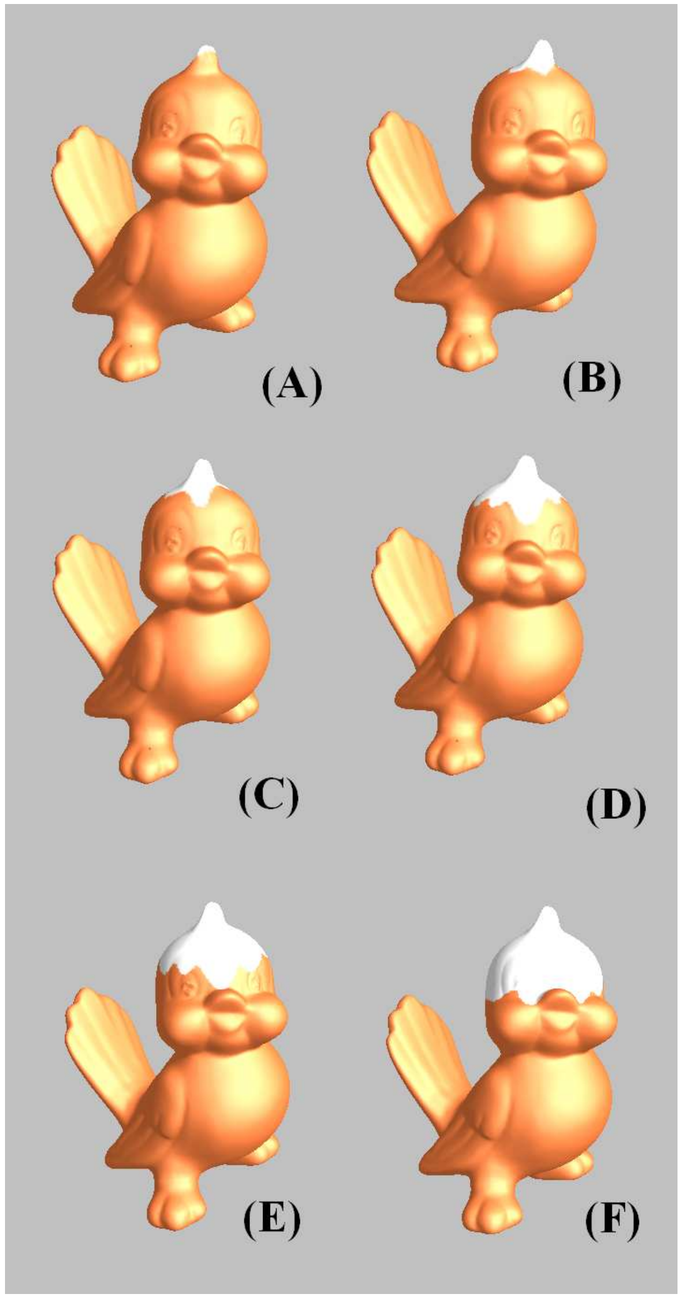

Figure 4.10: Illustration of Navier-Stokes equation on the surface. This example simulates the snow flowing down the bird surface. The external force used is the downward gravitational force projected to the tangent space of the surface.

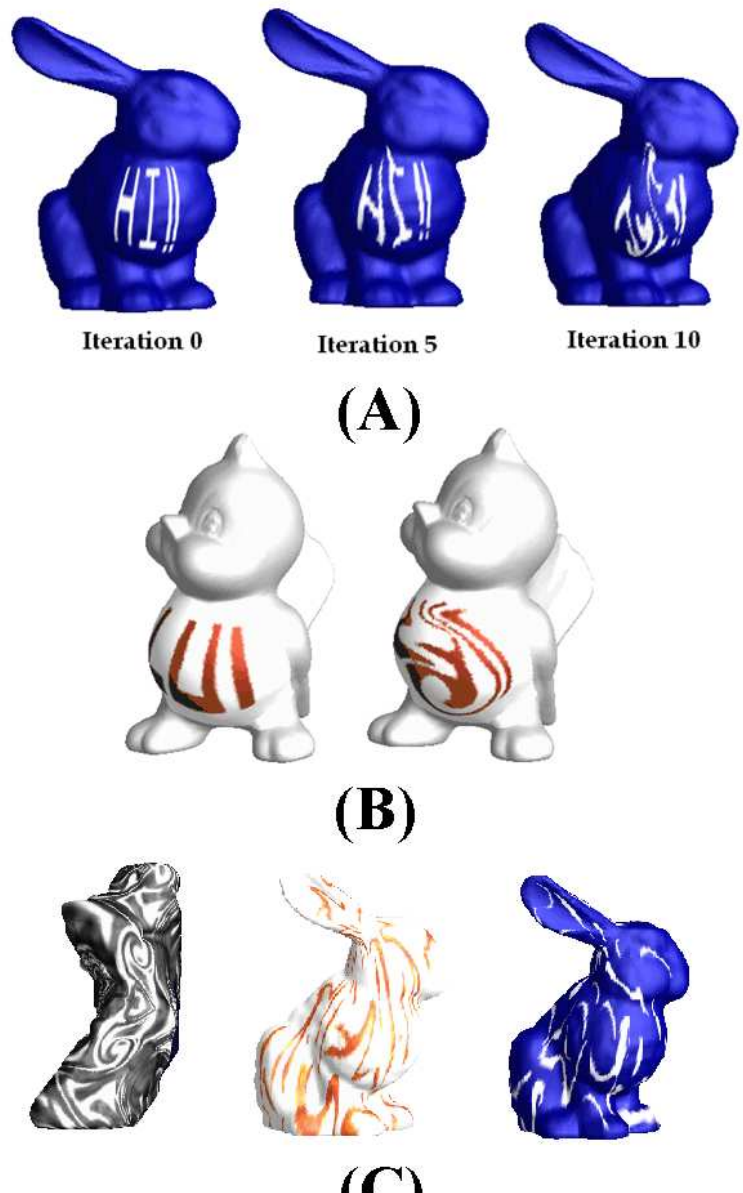

Figure 4.11: (A) shows a simulation of fluid flow on a bunny surface by solving Navier-Stoker's equation at different iterations. A circular force field is applied on the surface. (B) shows another example of fluid flow on a bird surface. (C) shows how solving surface fluid flow by Navier-Stoke's equation can be applied for surface decoration to generate texture on surfaces.

to generate texture on surfaces., we simulate fluid flow on a bunny surface by adding a S-shaped force.

4.6 Conclusion

In conclusion, we describe a method in this paper to solve variational problems on general surfaces with arbitrary topologies using the global conformal parameterization. With the conformal parameterization of the surface, the problems can be greatly simplified and are transformed into 2D problems on the parameter domain. The conformal parameterization has a simple metric $(g_{ij}) = \lambda \mathbf{Id}$. Under the conformal parameterization, the surface differential operators can be computed easily on the 2D parameter domain with simple formulae. The formulae are very similar to the formulae for the 2D Euclidean differential operators, except for the scalar multiplication of the conformal factor λ. Therefore, using the conformal parameterization to transform the variational problems on general surfaces to the 2D problems on the parameter domain has much easier equations than using other arbitrary parameterizations. The problem can then be solved easily by other well-known numerical schemes.

We have tested our algorithm on solving different image processing and surface processing problems on different surfaces, which require solving different variational problems. The experimental results show that our proposed algorithm can effectively solve the variational problems on the surface. Numerical analysis on the proposed algorithm has also been done to determine how the accuracy of the algorithm is affected by the accuracy in the approximation of the conformal parameterization.

CHAPTER 5

Automatic Brain Anatomical Feature Detection with Conformal Parameterization

5.1 Introduction

One important problem in human brain mapping research is to locate the important anatomical features. Anatomical features on the cortical surface are usually represented by landmark curves, called sulci/gyri curves. These landmark curves are important information for neuroscientists to study brain disease and to match different cortical surfaces [94][95][96]. Manual labelling of these landmark curves is time-consuming, especially when large sets of data have to be analyzed. Therefore, an automatic or semi-automatic way to detect these feature curves is necessary.In this paper, we present algorithms to automatically detect and match landmark curves on cortical surfaces to get an optimized brain conformal parametrization [97][39][38]. We trace the landmark curves on the cortical surfaces automatically based on the principal directions. Using geometric variants to detect features has been commonly used [98][99][100][101]. Suppose we are given the global conformal parametrization of the cortical surface. Fixing two endpoints, called the anchor points, we trace the landmark curve iteratively on the spherical/rectangular parameter domain along one of the two principal directions. Consequently, the landmark curves can be mapped onto the cortical surface. To speed up the iterative scheme, a good initial guess of the landmark curve is necessary. Therefore, we propose a method to get a good initialization by extracting the high curvature region on the cortical surface using Chan-Vese segmentation [54]. This involves solving a PDE (Euler-Lagrange equation) on the manifold using the global conformal parametrization as described in Chapter 4. As an application, we used these automatic labeled landmark curves to get an optimized brain conformal mapping, which can match important anatomical features across subjects. Similar to Chapter 3, this is done by minimizing a combined energy $E_{new} = E_{harmonic} + \lambda E_{landmark}$, which produces a close to conformal parameterization of the cortical surface while matching the important anatomical features as much as possible.

5.2 Previous works

Automatic detection of sulcal landmarks on the brain has been widely studied by different research groups. Prince et al. [102] has proposed a method for automated segmentation of major cortical sulci on the outer brain boundary. This is based on a statistical shape model, which includes a network of deformable curves on the unit sphere, seeks geometric features such as high curvature regions, and labels such features via a deformation process that is confined within a spherical map of the outer brain boundary. Lohmann et al. [103] has proposed an algorithm that automatically detects and attributes neuroanatomical names to the cortical folds using image analysis methods applied to magnetic resonance data of human brains. The sulci basins are segmented using a region growing approach. Zeng et al. [104] has proposed a method to automate intrasulcal ribbon finding, by using the cortex segmentation with coupled surfaces via a level set methods, where the outer cortical surface is embedded as the zero level set of a high-dimensional distance function. Recently, Kao et al. [105] presented a sequence of geometric algorithms to automatically extract the sulcal fundi and represent them as smooth polylines lying on the cortical surface. Based on geodesic depth information, their algorithm extracts sulcal regions by checking the connectivity above some depth threshold. After extracting endpoints of the fundi and then thinning each connected region with fixed endpoints, the curves are then smoothed using weighted splines on surfaces.

5.3 Sulci/Gyri on brain cortical surfaces

The human brain cerebrum is a convoluted surface with very complicated geometry. There are bumps and grooves on the cerebrum, called sulci and gyri respectively. Each hemisphere of the cerebral cortex is divided into four lobes by various sulci and gyri. In neuroanatomy, a sulcus is a depression in the surface of the brain that surrounds the gyri. The sulci and gyri on the cerebrum create the characteristic appearance of the brain in humans. Generally speaking, the sulci are the grooves and the gyri are the "bumps" that can be seen on the surface of the brain. Large furrows (sulci) that divide the brain into lobes are often called fissures. For example, the large furrow that divide the two hemispheres is called the interhemispheric fissure. The folding of the cerebral cortex produced by these bumps and grooves increases the amount of cerebral cortex that can fit in the skull. They are usually considered as important landmark features that provide useful anatomical information. The most common sulcus and gyrus include central sulcus, postcentral sulcus and precentral sulcus. The central sulcus is the most well-known of these landmarks. It protrudes into the brain at the central location from the top down, separating the parietal lobe from the frontal lobe and the primary motor cortex from the primary somatosensory cortex. The post-

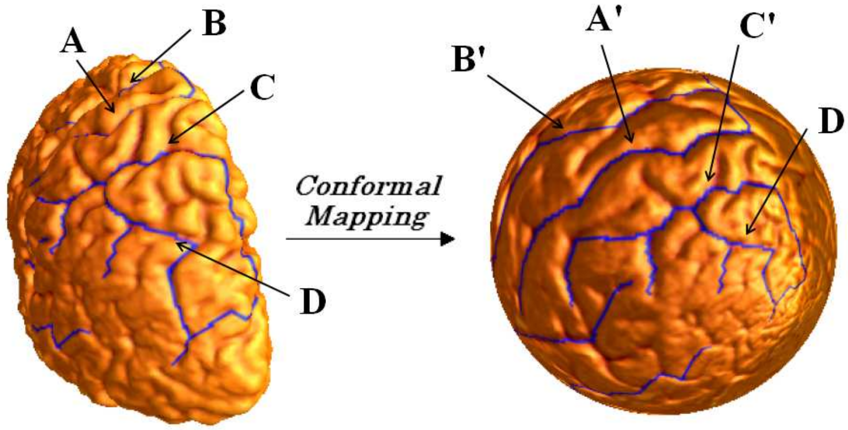

Figure 5.1: This figure shows some of the most important sulci on a human brain cortical surface. A, B, C and D represents the central sulcus, precentral sulcus, postcentral sulcus and intraparietal sulcus respectively on the human brain surface. They are projected onto a sphere through a conformal map for easier visualization. They are labelled as A', B', C' and D' respectively.

central sulcus lies immediately posterior to the central sulcus, and the precentral sulcus lies immediately anterior to the central sulcus. While most people share the same patterns of gyri and sulci on the cerebral cortex, the precise pattern can vary considerably from person to person. Figure 5.1 shows some of the most important sulci on a human brain cortical surface. On the left, A, B, C and D represents the central sulcus, precentral sulcus, postcentral sulcus and intraparietal sulcus respectively on the human brain surface. They are projected onto a sphere through a conformal map for easier visualization on the right. They are labelled as A', B', C' and D' respectively.

5.4 Basic Mathematical Theory

The brain surface is a convoluted surface with very complicated geometry. It is difficult to do calculation directly on the brain surface. In order to simplify the calculation, we parameterize the brain surface onto the 2D rectangle through a conformal map and solve everything on the 2D domain. Recall that a diffeomorphism $\phi : M \to N$ is a conformal mapping if it preserves the first fundamental form up to a scaling factor (the conformal factor). Mathematically, this means that $ds_M^2 = \lambda\phi^*(ds_N^2)$, where ds_M^2 and ds_N^2 are the first fundamental form on surfaces M and N, respectively and λ is the conformal factor. Consequently, the conformal parameterization of the brain surface preserves angles and thus preserves the local geometry. Also, the Jacobian of the conformal map is just the conformal factor. This is beneficial when conformal map is used to solve equations on the brain surface (See Chapter 4).

In order to detect the anatomical features, we need to have some shape descriptors defined on the brain surface which can delineate the sulci or gyri. In our project, we have found that the mean curvature and principal directions are good shape descriptors that well describe the sulci or gyri. The mean curvature and principal directions can all be computed from the Weingarten matrix. Recall that the normal curvature κ_n of a Riemann surface in a given direction is the reciprocal of the radius of the circle that best approximates a normal slice of the surface in that direction, which varies in different directions. It follows that:

$$\kappa_n = \mathbf{v}^T \mathbb{II}\mathbf{v} = \mathbf{v}^T \begin{pmatrix} e & f \\ f & g \end{pmatrix} \mathbf{v} \tag{5.1}$$

for any tangent vector $\mathbf{v}$.

$\mathbb{II}$ is called the Weingarten matrix and is symmetric. Its eigenvalues and eigenvectors are called principal curvatures and principal directions respectively. The mean of the eigenvalues is the mean curvature. A point on the Riemann surface at which the Weingarten matrix has the same eigenvalues is called an

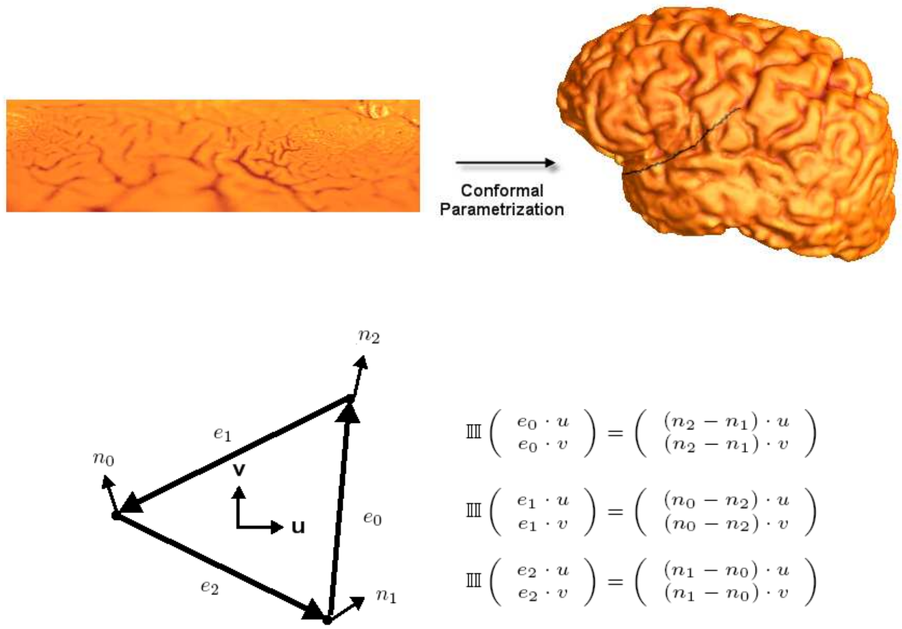

$$\mathbb{III}\begin{pmatrix} e_0 \cdot u \\ e_0 \cdot v \end{pmatrix} = \begin{pmatrix} (n_2 - n_1) \cdot u \\ (n_2 - n_1) \cdot v \end{pmatrix}$$

$$\mathbb{III}\begin{pmatrix} e_1 \cdot u \\ e_1 \cdot v \end{pmatrix} = \begin{pmatrix} (n_0 - n_2) \cdot u \\ (n_0 - n_2) \cdot v \end{pmatrix}$$

$$\mathbb{III}\begin{pmatrix} e_2 \cdot u \\ e_2 \cdot v \end{pmatrix} = \begin{pmatrix} (n_1 - n_0) \cdot u \\ (n_1 - n_0) \cdot v \end{pmatrix}$$

Figure 5.2: Left: Global conformal parametrization of the entire cortical surface onto the 2D rectangle. By introducing cutting boundaries on the cortical surface, the genus of the surface is increased. Holomorphic 1-form and the conformal parametrization can be found. The boundaries of the rectangle corresponds to the cutting boundaries on the surface. Right: A single face (triangle) of the triangulated mesh.

umbilic point. The detailed algorithm for computing the Weingarten matrix is described in Section.

5.5 Solving PDEs on surfaces using the global conformal parameterization

Our automatic landmark tracking algorithm involves solving partial differential equations on the surface. Solving equations directly on the brain surface is very difficult because of its complicated geometry. We propose to solve PDEs on the brain surface by using the global conformal parametrization. The main idea is to map the surface conformally to the 2D rectangles with the minimum number of coordinates patches. The problem can then be solved by solving a modified PDE on the 2D parameter domain. To do this, we have to use a set of differential operators on the manifold, namely, the covariant derivative. With the conformal parametrization, the covariant derivative can be formulated easily with simple formulas on the paramter domains. Once the PDE on the 3D surface is reformulated to the corresponding PDE on the 2D domain, we can solve the PDE on 2D by using some well-known numerical schemes. Since the Jacobian of the conformal mapping is simply a multiplication of the conformal factor, the modified PDE on the parameter domain will be very simple and easy to solve. For detail, please refer to Chapter.

5.6 Algorithm for automatic landmark tracking

In this section, we discuss our algorithm for automatic landmark tracking.

5.6.1 Computation of principal direction fields from the global conformal parametrization

In order to detect the anatomical features, we need to have some shape descriptors defined on the brain surface which can delineate the sulci or gyri. In this project, we use mean curvature and principal directions as the shape descriptor. They can all computed from the Weingarten matrix. We firstly describe how we can compute the Weingarten matrix.

Denote the cortical surface by C. Let $\phi : D \to C$ be the global conformal parametrization of C where D is a rectangular parameter domain. Let λ be the conformal factor of ϕ. Similar to Rusinkiewicz's work [106], we can compute the principal directions, and represent them on the parameter domain D. This is based on the following three steps:

Step 1 : Per – Face Curvature Computation

Let $u = \begin{pmatrix} \frac{1}{\sqrt{\lambda}} \\ 0 \end{pmatrix}$ and $v = \begin{pmatrix} 0 \\ \frac{1}{\sqrt{\lambda}} \end{pmatrix}$ be the directions of an orthonormal coordinate system for the tangent plane (represented in the parameter domain D). We can approximate the Weingarten matrix $\mathbb{III}$ for each face (triangle). For a triangle with three well-defined directions (edges) together with the differences in normals in those directions (Refer to Figure 5.2 right), we have a set of linear constraints on the elements of the Weingarten matrix, which can be determined using the least square method.

Step 2 : Coordinate system Transformation

After we have computed the Weingarten matrix on each face in the (u_f, v_f) coordinate system, we can average it with contribution from adjacent triangles. Suppose that each vertex p has its own orthonormal coordinate system (u_p, v_p). We have to transform the Weingarten matrix tensor into the vertex coordinates frame. The first component of $\mathbb{III}$, expressed in the (u_p, v_p) coordinate system, can be found as:

$$e_p = u_p^T \mathbb{III} u_p = (1,0) \begin{pmatrix} e_p & f_p \\ f_p & g_p \end{pmatrix} (1,0)^T$$

Thus,

$$e_p = (u_p \cdot u_f, u_p \cdot v_f) \mathbb{III} (u_p \cdot u_f, u_p \cdot v_f)^T$$

We can find f_p and g_p similarly.

Step3 : Weighting

The question about how much of the face curvature should be accumulated at each vertex is very important because different meshes have different resolution at different position. Thus, an aprropriate weighting function can help to reduce the error in the curvature approximation significantly. For each face f which is adjacent to the vertex p, we take the weighting $w_{f,p}$ to be the area of f divided by the squares of the lengths of the two edges that touch the vertex p. The weighting function we use can take care of the different resolution at different location of the mesh and effectively produce more accurate estimation of the curvature, normal and so on.

5.6.2 Extraction of Sulcal Region by Chan-Vese Segmentation

In order to speed up the landmark tracking algorithm, we begin with extracting the sulcal regions on the brain surface. This is done by extracting the high mean curvature regions on the cortical surface using the Chan-Vese (CV) segmentation method [107][105], based on the Mumford-Shah functional for segmentation [108][54][97]. After the sulcal region is extracted, we pick an arbitrary curve lying within the sulcal region as an initial guess of the sulcal landmark.

CV segmentation is a well known segmentation method on the 2D domain. We can extend the CV segmentation on $\mathbb{R}^2$ to the brain cortical surface M through conformal parameterization.

Let $\phi : \mathbb{R}^2 \to M$ be the conformal parametrization of the surface M. We propose to minimize the following energy functional:

$$
\begin{aligned}
F(c_1, c_2, \psi) = &\int_M (u_0 - c_1)^2 H(\psi) dS \\
&+ \int_M (u_0 - c_2)^2 (1 - H(\psi)) dS \\
&+ \nu \int_M |\nabla_M H(\psi)|_M dS
\end{aligned}
$$

where $\psi : M \to \mathbb{R}$ is the level set function and $| \cdot |_M = \sqrt{< \cdot, \cdot >}$ and u_0 is the mean curvature function on the cortical surface.

With the conformal parametrization, we have:

$$
\begin{aligned}
F(c_1, c_2, \psi) = &\int_{\mathbb{R}^2} \lambda (u_0 \circ \phi - c_1)^2 H(\psi \circ \phi) dxdy \\
&+ \int_{\mathbb{R}^2} \lambda (u_0 \circ \phi - c_2)^2 (1 - H(\psi \circ \phi)) dxdy \\
&+ \nu \int_{\mathbb{R}^2} \sqrt{\lambda} |\nabla H(\psi \circ \phi)| dxdy
\end{aligned}
$$

For simplicity, we let $\zeta = \psi \circ \phi$ and $w_0 = u_0 \circ \phi$. Fixing ζ, we must have:

$$
\begin{aligned}
c_1(t) &= \frac{\int_\Omega w_0 H(\zeta(t, x, y)) \lambda dxdy}{\int_\Omega H(\zeta(t, x, y)) \lambda dxdy}; \\
c_2(t) &= \frac{\int_\Omega w_0 (1 - H(\zeta(t, x, y)) \lambda dxdy}{\int_\Omega (1 - H(\zeta(t, x, y))) \lambda dxdy}
\end{aligned}
$$

Fixing c_1, c_2, the Euler-Lagrange equation becomes:

$$
\frac{\partial \zeta}{\partial t} = \lambda \delta(\zeta) [\ \nu \frac{1}{\lambda} \bigtriangledown \cdot (\sqrt{\lambda} \frac{\nabla \zeta}{||\nabla \zeta||}) - (w_0 - c_1)^2 + (w_0 - c_2)^2]
$$

Now, the sulcal landmarks on the cortical surface lie at locations with relatively high mean curvature. As shown in Figure, the brain surface is mapped to a 2D parameter domain with the conformal parameterization. It is colored with the mean curvature information. Note that the sulcal region has darker color, meaning that the sulcal region has higher mean curvature. To formulate the CV segmentation to extract the sulcal region, we can consider the intensity term as being defined by the mean curvature. Sulcal locations can then be circumscribed by first extracting out the high curvature regions. Fixing two anchor points inside the extracted region, we can get a good initialization of the landmark curve by looking for a shortest path inside the region that joins the two points. We select two umbilic points as the anchor points. By definition, an umbilic point on a manifold is a location at which the two principal curvatures are the same. Therefore, the umbilic points are the 'singularities' of the surface. Also, the umbilic points are the positions where the principal directions are not well-defined. In other words, $E_{principal}$ is not well defined at these points. If there are multiple umbilic points are found in one region, we select the two that are furthest apart.

5.6.3 Variational Method for Landmark Tracking

After the sulcal region is extracted, we can get an initial guess of the sulcal landmark by choosing an arbitrary curve joining the two feature points (umbilic points). This initial guess may not be the most accurate approximation of the sulcus and may not lie on the deepest region. We can iteratively improve the curve such that it moves to the deepest valley of the sulcal region. This is done by a variational approach to get a minimizing curve that follows the principal curvature as much as possible. We have found that the principal directions can effectively be used to trace the sulci and gyri. As shown in Figure 5.3, the red

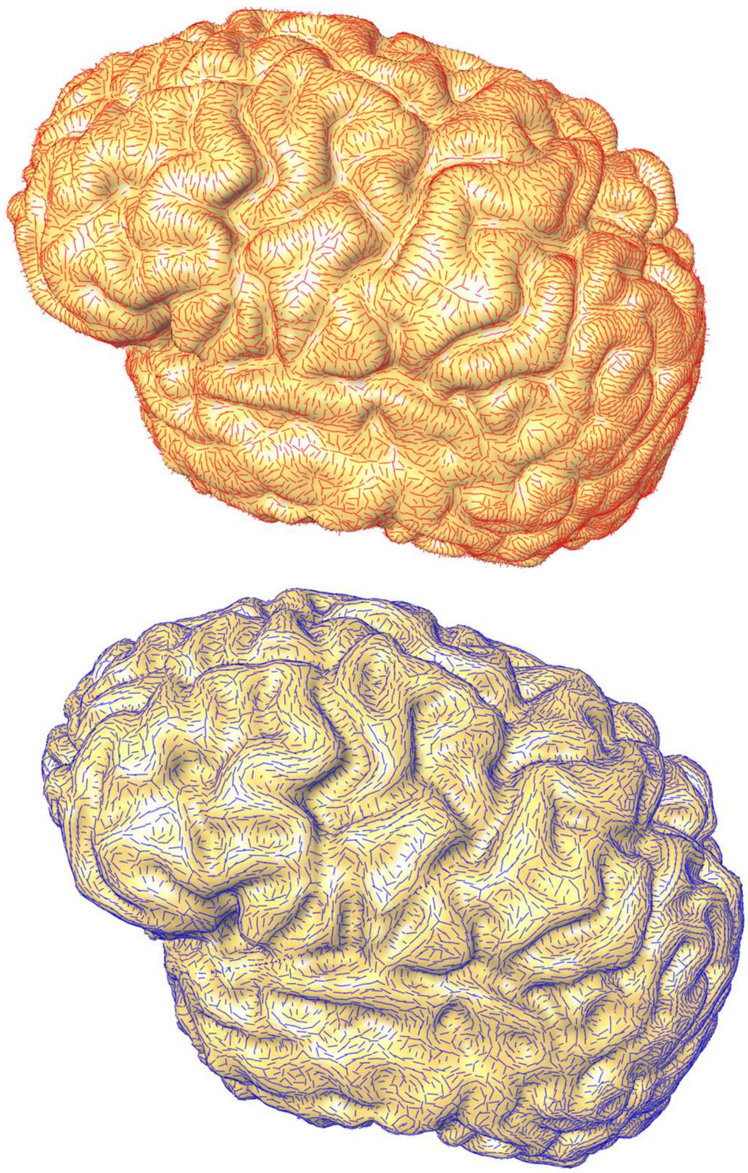

Figure 5.3: **Top** : The value of $E_{principal}$ at each iteration is shown. Energy reached its steady state with 30 iterations, meaning that our algorithm is efficient using the CV model as the initialization. **Bottom** : Numerical comparison between automatic labeled landmarks and manually labeled landmarks by computing the Euclidean distance $E_{difference}$ (on the parameter domain) between the automatically and manually labeled landmark curves, which are unit-speed parametrized. These manually-labeled sulcal landmarks are manually labeled directly on the brain surface by neuroscientists.

arrow represents the principal direction field with smaller eigenvalues at each points on the brain surface. They follow the direction of the sulci. (B) shows the principal directions with larger eigenvalues at each points on the brain surface. They follow the direction of the gyri.

The principal direction field $\overrightarrow{V}(t)$ with smaller eigenvalues on the cortical surface C can be computed as described in Section. With $\overrightarrow{V}(t)$, we propose a variational method to trace the sulcal landmark curve iteratively, after fixing two anchor points (a & b) on the sulci. Let $\phi : D \to C$ be the conformal parametrization of C, $< \cdot, \cdot >$ to be its Riemannian metric and λ to be its conformal factor. We propose to locate a curve $\overrightarrow{c} : [0,1] \to C$ with endpoints a and b, that minimizes the following energy functional:

$$E_{principal}(\overrightarrow{c}) = \int_0^1 |\frac{\overrightarrow{c}'}{\sqrt{< \overrightarrow{c}', \overrightarrow{c}' >_M}} - \overrightarrow{V} \circ \overrightarrow{c}|_M^2 dt = \int_0^1 |\frac{\overrightarrow{\gamma}'}{|\overrightarrow{\gamma}'|} - \overrightarrow{G}(\overrightarrow{\gamma})|^2 dt$$

where $\overrightarrow{\gamma} = \overrightarrow{c} \circ \phi^{-1} : [0,1] \to D$ is the corresponding iteratively defined curve on the parameter domain; $\overrightarrow{G}(\overrightarrow{\gamma}) = \sqrt{\lambda(\overrightarrow{\gamma})}\overrightarrow{V}(\overrightarrow{\gamma})$; $| \cdot |_M^2 =< \cdot, \cdot >_M$ and $| \cdot |$ is the (usual) length defined on D. By minimizing the energy E, we minimize the difference between the tangent vector field along the curve and the principal direction field $\overrightarrow{V}$. The resulting minimizing curve is the curve that is closest to the curve traced along the principal direction (See Figure 5.4).

Let:

$\overrightarrow{G} = (G_1, G_2, G_3)$; $\overrightarrow{K} = (K_1, K_2, K_3) = \frac{\overrightarrow{\gamma}'}{|\overrightarrow{\gamma}'|} - \overrightarrow{G}(\overrightarrow{\gamma})$

$\overrightarrow{L}_1 = \frac{(1,0,0)}{|\overrightarrow{\gamma}'|} - \frac{\gamma_1' \overrightarrow{\gamma}}{|\overrightarrow{\gamma}'|^3}$; $\overrightarrow{L}_2 = \frac{(0,1,0)}{|\overrightarrow{\gamma}'|} - \frac{\gamma_2' \overrightarrow{\gamma}}{|\overrightarrow{\gamma}'|^3}$; $\overrightarrow{L}_3 = \frac{(0,0,1)}{|\overrightarrow{\gamma}'|} - \frac{\gamma_3' \overrightarrow{\gamma}}{|\overrightarrow{\gamma}'|^3}$

Based on the Euler-Lagrange equation, we can locate the landmark curve iteratively using the steepest descent algorithm:

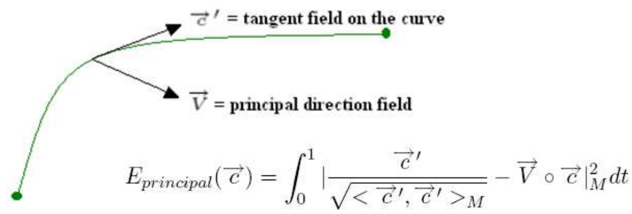

Figure 5.4: The figure demonstrates the meaning of $E_{principal}$. It measures the difference between the tangent vector field along the curve and the principal direction field $\vec{V}$. The resulting minimizing curve is the curve that is closest to the curve traced along the principal direction.

$$\frac{d\overrightarrow{\gamma}}{dt} = \Sigma_{i=1}^{3}[K_i \overrightarrow{L}_i]' + K_i \nabla G_i$$

With this iterative scheme, the energy $E_{principal}$ is actually decreasing.

Proof :

$\frac{dE_{principal}}{ds}|_{s=0}(\overrightarrow{\gamma} + s\overrightarrow{u})$

$= \int_0^1 \frac{d}{ds}|_{s=0}|\frac{\overrightarrow{\gamma}'+s\overrightarrow{u}'}{|\overrightarrow{\gamma}'+s\overrightarrow{u}'|} - \overrightarrow{G}(\overrightarrow{\gamma} + s\overrightarrow{u})|^2 dt$

$= \int_0^1 (\frac{\overrightarrow{\gamma}'}{|\overrightarrow{\gamma}'} - \overrightarrow{G}(\overrightarrow{\gamma})) \cdot [\frac{\overrightarrow{u}'}{|\overrightarrow{\gamma}'|} - \frac{\overrightarrow{\gamma}'(\overrightarrow{\gamma}' \cdot \overrightarrow{u}')}{|\overrightarrow{\gamma}'|^3} - \overrightarrow{G}'(\overrightarrow{\gamma}) \cdot \overrightarrow{u}]dt$

$= \int_0^1 (\frac{\overrightarrow{\gamma}'}{|\overrightarrow{\gamma}'} - \overrightarrow{G}(\overrightarrow{\gamma})) \cdot [\frac{\overrightarrow{u}'}{|\overrightarrow{\gamma}'|} - \frac{\overrightarrow{\gamma}'(\overrightarrow{\gamma}' \cdot \overrightarrow{u}')}{|\overrightarrow{\gamma}'|^3} - \overrightarrow{G}'(\overrightarrow{\gamma}) \cdot \overrightarrow{u}]dt$

$= -\int_0^1 \Sigma_{i=1}^{3}\{[K_i \overrightarrow{L}_i]' + K_i \nabla G_i\} \cdot \overrightarrow{u} < 0$

if we let $\overrightarrow{u} = \Sigma_{i=1}^{3}\{[K_i \overrightarrow{L}_i]' + K_i \nabla G_i\}$.

(Here, G_i, K_i, L_i are defined as in Section 4.3)

Thus, the energy $E_{principal}$ is decreasing. **QED**

Our automatic landmark tracking algorithm is summarized in Figure 5.5

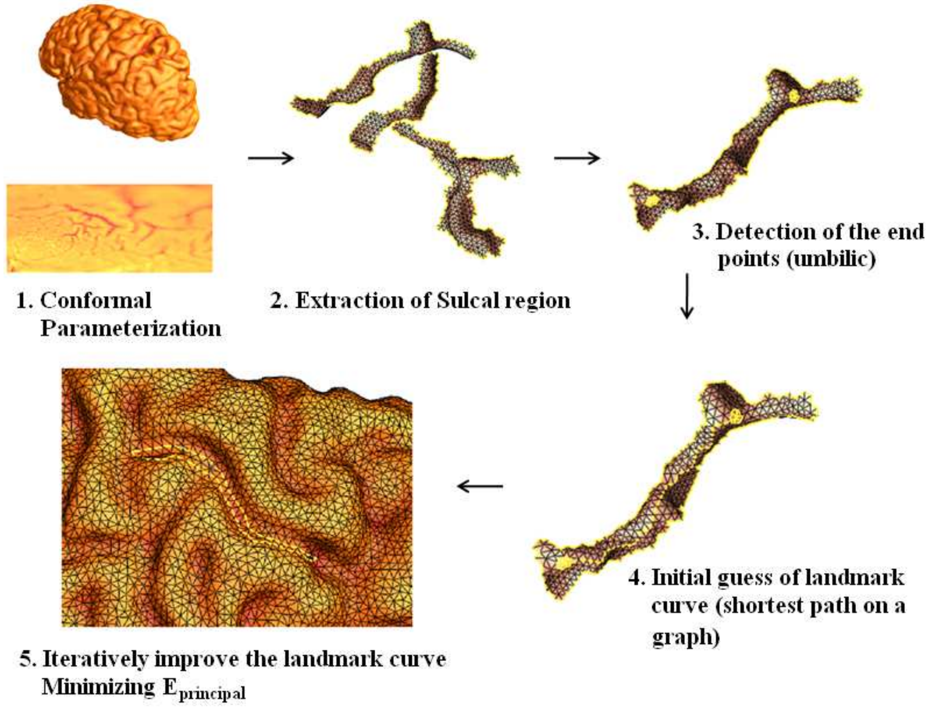

Figure 5.5: The figure summarizes the five steps of our automatic landmark tracking algorithm.

5.7 Optimization of brain conformal parametrization

In brain mapping research, cortical surface data are often mapped conformally to a parameter domain such as a sphere, providing a common coordinate system for data integration. As an application of our automatic landmark tracking algorithm, we use the automatically labeled landmark curves to generate an optimized conformal mapping on the surface, in the sense that homologous features across subjects are caused to lie at the same parameter locations in a conformal grid. This matching of cortical patterns improves the alignment of data across subjects. We apply the algorithm introduced in Chapter 3 to get the optimized brain conformal parameterization which minimizes the compound energy functional $E_{new} = E_{harmonic} + \lambda E_{landmark}$, where $E_{harmonic}$ is the harmonic energy of the parameterization and $E_{landmark}$ is the landmark mismatch energy. Here, instead of using the manually labeled discrete landmark points, automatically traced landmark (continuous) curves are used. Also, in our previous work, correspondences between discrete landmark points have to be manually specified. Here, the correspondence are obtained automatically using the unit speed reparametrization.

Suppose C_1 and C_2 are two cortical surfaces we want to compare. We let $\phi_1 : C_1 \to S^2$ be the conformal parameterization of C_1 mapping it onto S^2. Let $\{p_i : [0,1] \to S^2\}$ and $\{q_i : [0,1] \to S^2\}$ be the automatic labeled landmark curves, represented on the parameter domain S^2 with unit speed parametrization, for C_1 and C_2 respectively. Let $h : C_2 \to S^2$ be any homeomorphism from C_2 onto S^2. We define the landmark mismatch energy of h as: $E_{landmark}(h) = 1/2 \sum_{i=1}^{n} \int_0^1 ||h(q_i(t)) - \phi_1(p_i(t))||^2 dt$, where the norm represents distance on the sphere. By minimizing this energy functional, the Euclidean distance between the corresponding landmarks on the sphere is minimized.

5.8 Experimental Results

In one experiment, we tested our automatic landmark tracking algorithm on a set of 40 left hemisphere cortical surfaces extracted from brain MRI scans, acquired from normal subjects at 1.5 T (on a GE Signa scanner). In our experiments, 10 major sulcal landmarks (central/precentral) were automatically located on cotical surfaces.

Figure 5.6 shows how we can effectively locate the initial landmark guess areas on the cortical surface using the Chan-Vese segmentation. We consider the intensity term as being defined by the mean curvature. Sulcal locations can then be circumscribed by first extracting out the high curvature regions. (A) shows the result of extraction using a circular initial contour. Notice that the contour evolved to the deep sulcal region. (B) shows the result of extration using a larger initial circular contour. More sulcal regions can be extracted.

In Figure 5.7, we locate the umbilic points in each sulcal region, which are chosen as the anchor points.

Our variational method to locate landmark curves is illustrated in Figure 5.8. With the initial guess given by the Chan-Vese model (we choose the two extreme points in the located area as the anchor points), we trace the landmark curves iteratively based on the principal direction field. In Figure 5.8 (left), we trace the landmark curves on the parameter domain along the edges whose directions are closest to the principal direction field. The corresponding landmark curves on the cortical surface is shown. Figure 5.8 (left) shows how the curve evolves to a deeper sulcal region with our iterative scheme. In Figure 5.8 (right), ten sulcal landmarks are located using our algorithm. Our algorithm is quite efficient with the good initial guess using the CV-model. (See Fig 5.9 Top) To compare our automatic

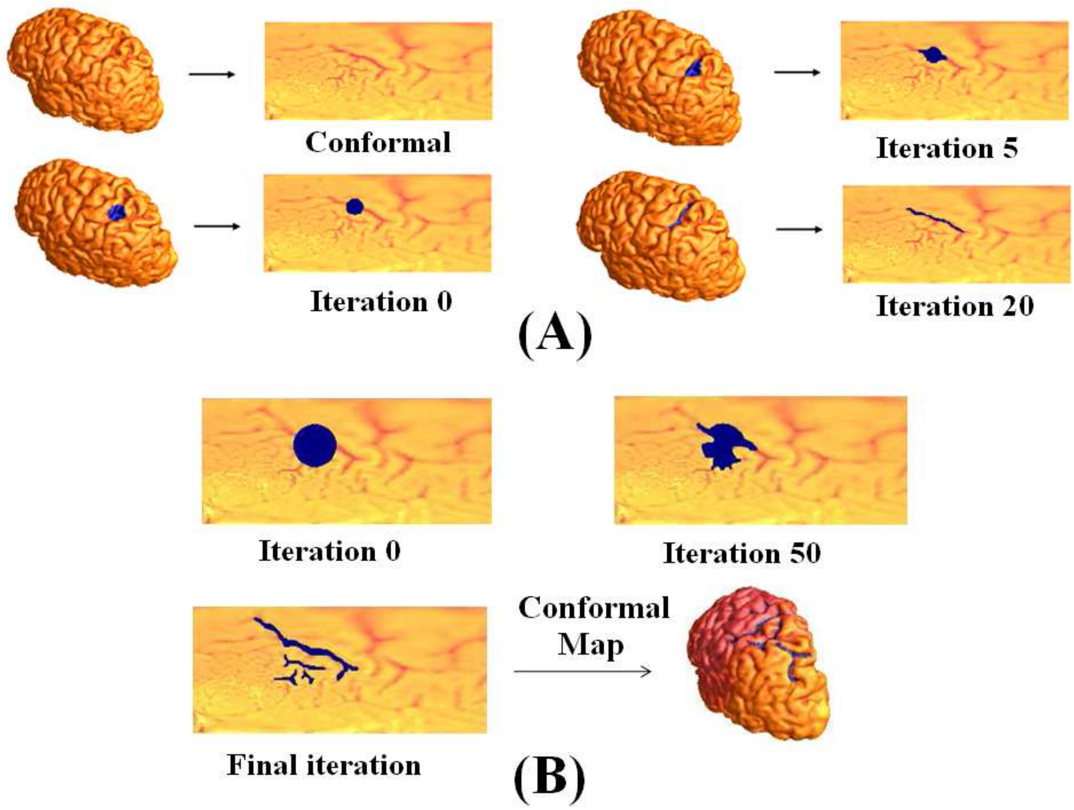

Figure 5.6: Sulcal region extraction on the cortical surface by Chan-Vese segmentation. We consider the intensity term as being defined by the mean curvature. Sulcal locations can then be circumscribed by first extracting out the high curvature regions. (A) shows the result of extraction using a circular initial contour. (B) shows the result of extration using a larger initial circular contour. More sulcal regions can be extracted

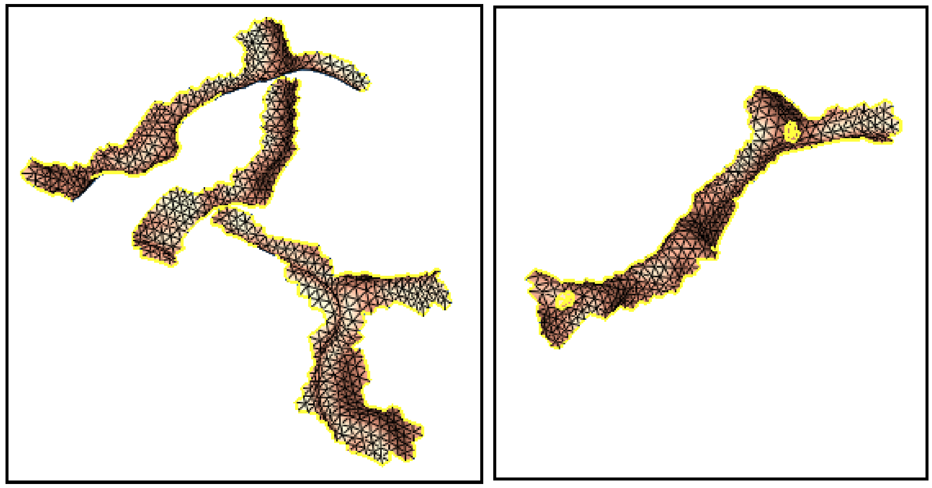

Figure 5.7: Detection of end points of the landmark curve. Umbilic points are located on each sulci region, which are chosen as the end points of the landmark curves.

landmark tracking results with the manually labeled landmarks, we measured the Euclidean distance $E_{difference}$ (on the parameter domain) between the automatically and manually labeled landmark curves. Figure 5.9(Bottom) shows the value of the Euclidean distance $E_{difference} = \int_0^1 ||\overrightarrow{c}_{principal}(t) - \overrightarrow{c}_{manual}(t)||^2 dt$ between the automatically and manually labeled landmark curves at different iterations for different landmark curves. The two landmark curves are unit-speed parametrized, denoted by $\overrightarrow{c}_{principal}(t)$ and $\overrightarrow{c}_{manual}(t)$ respectively. The manually-labeled sulcal landmarks are manually labeled directly on the brain surface by neuroscientists. Note that the value becomes smaller as the iterations proceed. This means that the automatically labeled landmark curves more closely resemble those defined manually as the iterations continues. Figure 5.10 illustrates the application of our automatic landmark tracking algorithm. We illustrated our idea of the optimization of conformal mapping using the automatically traced landmark curves. Figure 5.10 (A) and (B) show two different cortical surfaces being mapped con-

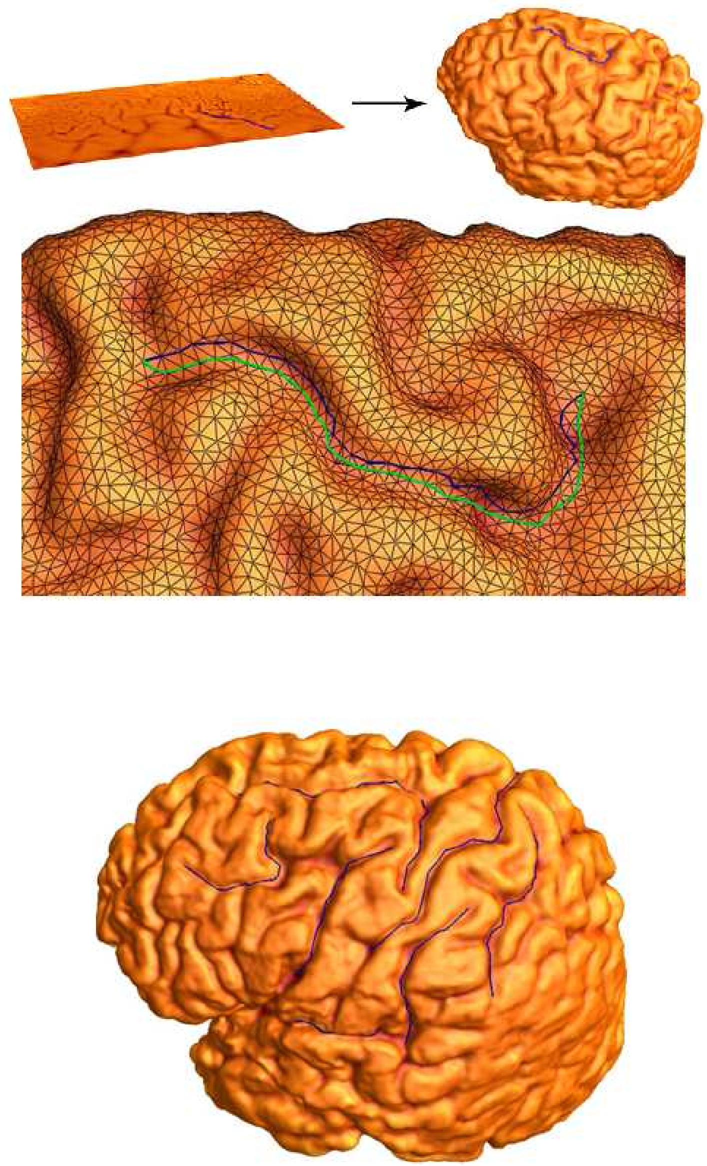

Figure 5.8: Automatic landmark tracking using a variational approach. **Top** : With the global conformal parameterization of the entire cortical surface, we trace the landmark curves on the parameter domain along the edges whose directions are closest to the principal direction field. It gives a good initial guess of the landmark curve (blue curve). The landmark curve is then evolved to a deeper region (green curve) using our variational approach. **Bottom** : Ten sulcal landmarks are automatically traced using our algorithm.

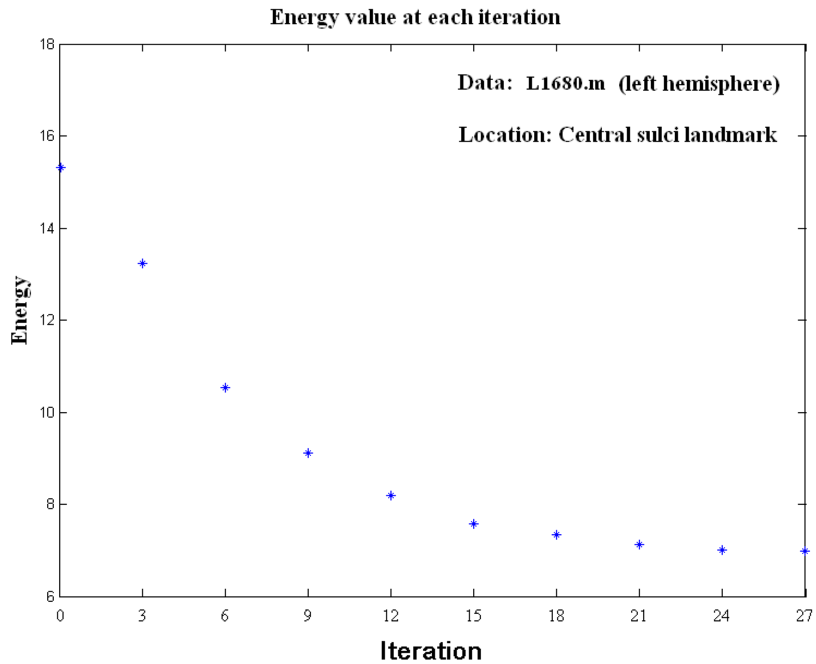

Difference between the two landmarks is measured by:

$$E_{difference} = \int_0^1 ||\vec{c}_{principal}(t) - \vec{c}_{manual}(t)||^2 dt$$

L1627.m	Central	Pre-central	Post-central
Iteration 0	1.28	1.31	1.27
Iteration 30	0.21 $\downarrow$ 83.6%	0.22 $\downarrow$ 83.2%	0.21 $\downarrow$ 83.5%

L1680.m	Central	Pre-central	Post-central
Iteration 0	1.33	1.35	1.26
Iteration 30	0.24 $\downarrow$ 82.0%	0.28 $\downarrow$ 79.3%	0.26 $\downarrow$ 79.4%

Figure 5.9: **Top** : The value of $E_{principal}$ at each iteration is shown. Energy reached its steady state with 30 iterations, meaning that our algorithm is efficient using the CV model as the initialization. **Bottom** : Numerical comparison between automatic labeled landmarks and manually labeled landmarks by computing the Euclidean distance $E_{difference}$ (on the parameter domain) between the automatically and manually labeled landmark curves, which are unit-speed parametrized. These manually-labeled sulcal landmarks are manually labeled directly on the brain surface by neuroscientists.

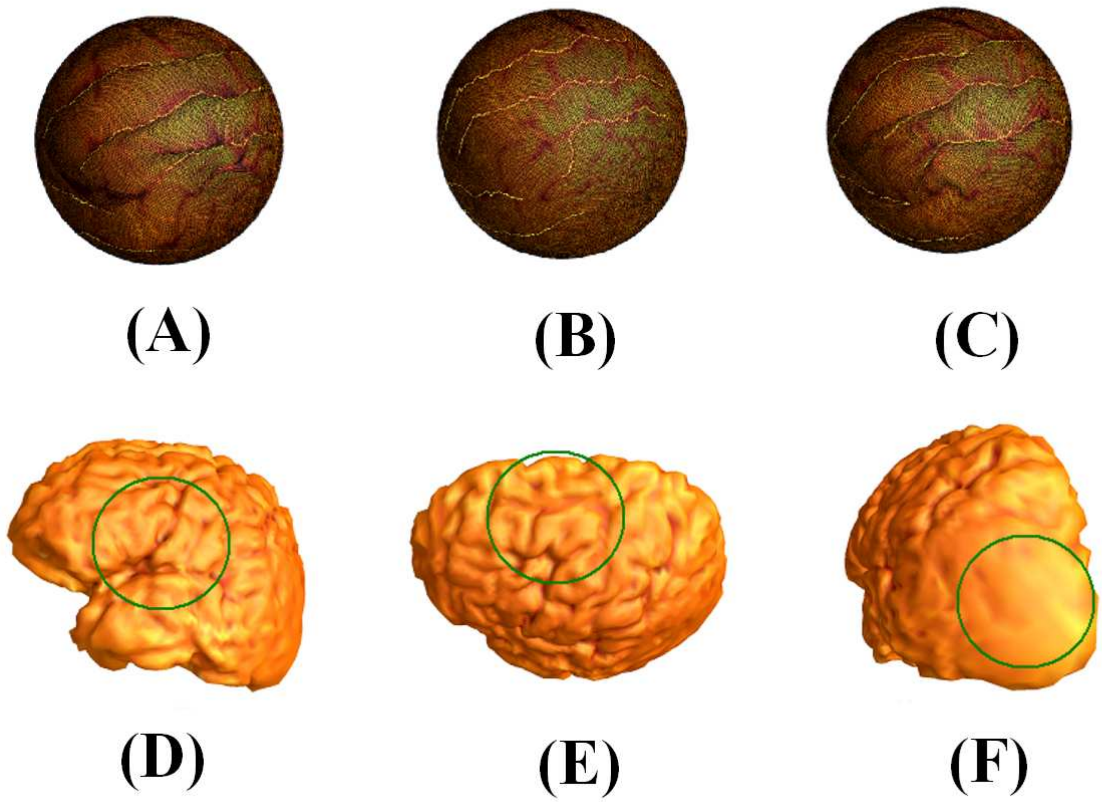

Figure 5.10: Optimization of brain conformal mapping using automatic landmark tracking. In (A) and (B), two different cortical surfaces are mapped conformally to the sphere. The corresponding landmark curves are aligned inconsistently on the spherical parameter domain. In (C), we map the same cortical surface of (B) to the sphere using our algorithm. Note that the alignment of the landmark curves is much more consistent with the those in (A). (D), (E), (F) shows the average surface (for N=15 subjects) based on the optimized conformal re-parametrization using the variational approach. Except in (F), where no landmarks were defined automatically, the major sulcal landmarks are remarkably well defined, even in this multi-subject average.

formally to the sphere. Notice that the alignment of the sulci landmark curves are not consistent. In Figure 5.10 (C), the same cortical surface in (B) is mapped to the sphere using our method. Notice that the landmark curves closely resemble to those in (A), meaning that the alignment of the landmark curves is more consistent with our algorithm. To visualize how well our algorithm can improve the alignment of the important sulcal landmarks is, we took average surface of the 15 cortical surfaces by using the optimized conformal parametrization algorithm [109]. Figure 5.10(D), (E) and (F) shows the average surface (for N=15 subjects) based on the optimized conformal re-parametrization using the variational approach. Except in (F), where no landmarks were defined automatically, the major sulcal landmarks are remarkably well defined, even in this multi-subject average. As sown in (D) and (E), sulcal landmarks are clearly preserved inside the green circle where landmarks were defined automatically. In (F), the sulcal landmarks are averaged out inside the green circle where no landmarks were defined. This suggests that our algorithm can help by improving the alignment of major anatomical features in the cortex. Further validation work, of course, would be necessary to assess whether this results in greater detection sensitivity in computational anatomy studies of the cortex, but the greater reinforcement of features suggests that landmark alignment error is substantially reduced, and this is one major factor influencing signal detection in multi-subject cortical studies.

5.9 Conclusion

In this paper, we propose a variational method to automatically trace landmark curves on cortical surfaces, based on the principal directions. To accelerate the iterative scheme, we initialize the curves by extracting high curvature regions using Chan-Vese segmentation. This involves solving a PDE on the cortical manifold. The landmark curves detected by our algorithm closely resembled those labeled manually. Finally, we use the automatically labeled landmark curves to create an optimized brain conformal mapping, which matches important anatomical features across subjects. Surface averages from multiple subjects show that our computed maps can consistently align key anatomic landmarks.

CHAPTER 6

Shape Based Landmark Matching Diffeomorphism between Cortical Surfaces

6.1 Introduction

As it was mentioned in earlier chapters, finding meaningful parametrization of the cortical surface is a key problem in brain mapping research. Applications include the registration of functional activation data across subjects, statistical shape analysis, morphometry, and processing of signals on brain surfaces (e.g., denoising or filtering). Applications that compare surface data often make use of surface diffeomorphisms that result from parameterization. For the above diffeomorphisms to map data consistently across surfaces, parametrizations are required to preserve the original surface geometry as much as possible. Parameterizations should also be chosen so that the resulting diffeomorphisms between surfaces align key anatomical features consistently. This kind of parameterizations with good anatomical features alignment is particularly important for brain disease analysis such as building the average brain shape. This is advantageous as the surface average of many subjects would retain features that consistently occur on sulci, while uniform speed parameterizations may cause these features to cancel out. Figure 6.2 gives an illustration of features can be canceled out with poor correspondece between landmarks when computing the surface average.

Conformal mapping [17][19] is particularly convenient for genus-zero cortical surface models since it gives a parameterization without angular distortions, and comes with computational advantages when solving PDEs on surfaces using grid-based and metric-based computations [63]. However, the above parameterization is not guaranteed to map anatomical features, such as sulcal landmarks, consistently from subject to subject [20][19].

Landmark-based diffeomorphisms [20][19][48][49][51][110] are often used to compute, or adjust, cortical surface parameterizations. Similarly to the above works, given two cortical surfaces with anatomical landmarks (sulci curves), we propose a method to find close to conformal parameterizations for the surfaces driven by shape based correspondences (*registration*) between the curves. Our work has three main contributions; first, the surface diffeomorphism resulting from our parameterization maps the sulcal curves *exactly*; second, the correspondence is shape based, i.e., maps similarly-shaped segments of sulcal curves to each other; finally, the conformality of the surface parameterizations is preserved to the greatest possible extent [37].

6.2 Previous works

Optimization of surface diffeomorphisms by landmark matching has been studied intensively. As described in Chapter 2, Gu et al. [19] proposed to optimize the conformal parametrization by composing an optimal Möbius transformation so that it minimizes a landmark mismatch energy. The resulting parameterization remains conformal. Glaunes et al.[48] proposed to generate large deformation diffeomorphisms of the sphere onto itself, given the displacements of a finite set of template landmarks. The diffeomorphism obtained can match landmark features well, but it is, in general, not a conformal mapping, which can be advantageous for solving PDEs on the resulting grids. Leow et al.[49] proposed a level-set based approach for matching different types of features, including points and 2D or 3D curves represented as implicit functions.

Tosun et al. [51] proposed a more automated mapping technique that results in good sulcal alignment across subjects, by combining parametric relaxation, iterative closest point registration and inverse stereographic projection. In Chapter 3, we [20] proposed an energy that computes maps that are close to conformal and also driven by a landmark matching term that measures the Euclidean distance between the specified landmarks. We proposed to use discrete landmark points in Chapter 2, where correspondence between landmarks are labelled manually. In Chapter 5, we proposed to use landmark curves which are automatically detected. The correspondence between landmark curves are obtained automatically through unit speed reparameterization. It has a drawback because the correspondence between landmark curves does not follow any shape information and thus affecting the quality of the optimized conformal map (See Figure 6.1 and Figure 6.2). (A) and (B) shows two different surfaces. The correspondence between landmark curves are labeled with yellow dots. Note that the correspondence does not follow any shape information (corners are not mapped to corners). The ideal correspondence based on the shape information of the curve is shown in (C).

Many of the above methods e.g. [20][48] require corresponding landmark points on the surfaces to be labeled in advance. Secondly, the landmark match measures used above are based on Euclidean distance, or overlap of level set functions representing the landmarks, and do not use shape information to guide correspondences of features within curves. So, the resulting correspondences would be unreliable in the case of landmark curves that differ by non-rigid deformations. Finally, constraining the surface diffeomorphism to exactly align the landmark curves during minimization is difficult, e.g. [20][51].

To resolve the above issues, we propose a method to optimize the conformal parameterization of the surfaces while non-rigidly registering the landmark curves. Specifically, we formulate our problem as a variational energy defined on a search space of diffeomorphisms generated as flows of smooth vector fields. The vector fields are restricted only to those that *do not flow* across the landmark curves (to enforce exact landmark correspondence). Our energy has 2 terms: (1) a shape term to map similar shaped segments of the landmark curves to each other, and (2) a harmonic energy term to optimize the conformality of the parametrization maps.

6.3 Basic Mathematical Background: Integral Flow on Surfaces

In this section, we introduce briefly the concept of integral flow of a vector field on a Riemann surface.

Let $\vec{V}$ be a smooth vector field on a Riemann surface M, which associates a tangent vector to every point on S. Given the vector field $\vec{V}$, we can try to define curves γon S such that for each t in an interval I

$$\gamma'(t) = V(\gamma(t)); \quad \gamma(0) = p \tag{6.1}$$

If V is Lipschitz continuous we can find a unique C^1-curve γ^x for each point x in S so that:

$$\gamma_x'(t) = V(\gamma_x(t)) \quad (t \in (-\epsilon, +\epsilon) \subset R); \qquad \gamma^x(0) = x \tag{6.2}$$

On a compact Riemann surface S, any smooth vector field $\vec{V}$ is *complete* meaning that every integral curve is defined for aa $t \in R$. We can define a map, called the *integral flow* of $\vec{V}$, $\phi(t,x) : R \times S \to S$ as follow:

$$\phi(t,x) = \gamma_x(t) \tag{6.3}$$

Fixing t, $\phi^t(x)\phi(t,x)$ is a diffeomorphism of the surface S. Therefore, we can regards the integral flow as a collection of diffeomorphisms of S. Interestingly, the integral flow follows the group law meaning that $\phi^t \circ \phi^s(x) = \phi^{s+t}(x)$.

In this work, we consider the search space of diffeomorphisms as the integral of smooth vector fields. By looking for a smooth vector field which satisfies certain energy functional, we can ensure that the map obtained is a diffeomporphism which matches landmarks based on the shape information.

6.4 Model

Given two cortical surfaces M_1 and M_2, with sulcal landmark curves $\hat{C}_1$ and $\hat{C}_2$ labeled on them. The curves $\hat{C}_i$ have the same topology relative to M_i. These landmarks curves can be detected automatically by the automatic landmark tracking technique as described in Chapter 5 [97]. Here, we want to find a diffeomorphism $F : M_1 \to M_2$ between M_1 and M_2 such that F maps similarly shaped segment of $\hat{C}_1$ and $\hat{C}_2$ to each others. In particular, we want to find parameterizations $\hat{f}_1 : \Omega \subset \Re^2 \to M_1$, $\hat{f}_2 : \Omega \to M_2$ of M_1 and M_2 onto the 2D parameter domain Ω such that the diffeomorphism $F = \hat{f}_2$ o $\hat{f}_1^{-1}|$ is a shape based diffeomorphism that maps $\hat{C}_1$ exactly onto $\hat{C}_2$. Also we want $\hat{f}_i$ to be as conformal as possible.

To simplify our computations, M_i are firstly conformally parameterized onto the conformal parameter domain D_i by $g_i : M_i \to D_i$. Assume that $\hat{C}_i$ are mapped to C_i on the parameter domain D_i. Thus, we can reduce our problem to the 2D problem of finding diffeomorphism $\tilde{f}_i : \Omega \to D_i$ such that $\tilde{f}_2$ o $\tilde{f}_1^{-1}|_{C_1} = C_2$ is a shape-based diffeomorphism onto C_2. The shaped based landmark matching diffeomorphism between M_1 and M_2, that is close to conformal, can be obtained from the composition of maps $F = g_2^{-1} \circ \tilde{f}_2 \circ \tilde{f}_1^{-1} \circ g_1$.

We propose our problem as the minimization of a variational energy with respect to diffeomorphisms $\tilde{f}_i : \Omega \to D_i$, subject to the correspondence constraint $\tilde{f}_2$ o $\tilde{f}_1^{-1}(C_1) = C_2$. The energy consists of two terms. The first term measures the harmonic energy of the maps $\tilde{f}_i$, and the second term measures the shape dissimilarity between C_1 and $\tilde{f}_2$ o $\tilde{f}_1^{-1}(C_1)$.

To handle the above correspondence constraint, we move all our computations to the parameter domain Ω using initial diffeomorphisms $f_{0,i} : \Omega \to D_i$. Let $C \subset \Omega$ be a topological representative of C_i, the common representation of C_i on Ω. We assume the initial map satisfies $f_{0,i}(C) = C_i$ (See Figure 6.3). With the above framework, the energy is formulated over Ω, and the search space of diffeomorphisms $\tilde{f}_i : \Omega \to D_i$, subject to $\tilde{f}_2$ o $\tilde{f}_1^{-1}(C_1) = C_2$, can be constructed as time-1 flows of smooth vector fields on Ω that do not flow across C. For the shape term, we measure the shape dissimilarity between the corresponding landmarks which minimizes the difference in *geodesic curvatures* on the corresponding pairs of points on C_1 and C_2. We discuss the details in the following sections.

6.4.1 Formulation

The initial diffeomorphisms $f_{0,i}$ give us a convenient way to perform our computations on the domain Ω. Diffeomorphisms $\tilde{f}_i : \Omega \to D_i$ with $\tilde{f}_2$ o $\tilde{f}_1^{-1}(C_1) = C_2$ can be realized through unique diffeomorphisms $f_i : \Omega \to \Omega$ with $f_i(C) = C$, satisfying $\tilde{f}_i = f_{0,i}$ o f_i (Fig. 6.3(left)). Thus we formulate our problem as the

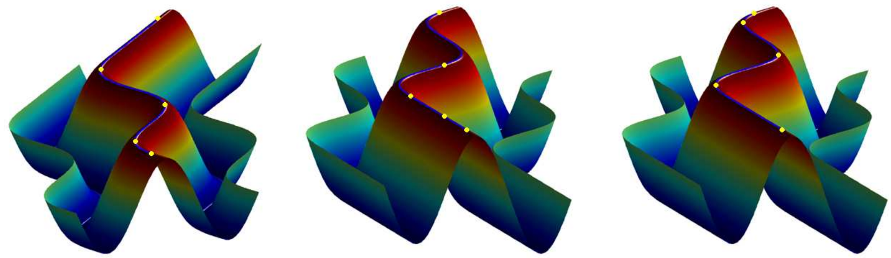

(A) (B) (C)

Figure 6.1: The figure shows the correspondece between landmark curves obtained through unit speed reparameterization. (A) and (B) shows two different surfaces. The correspondence between landmark curves are labeled with yellow dots. Note that the correspondence does not follow any shape information (corners are not mapped to corners). The ideal correspondence based on the shape information of the curve is shown in (C).

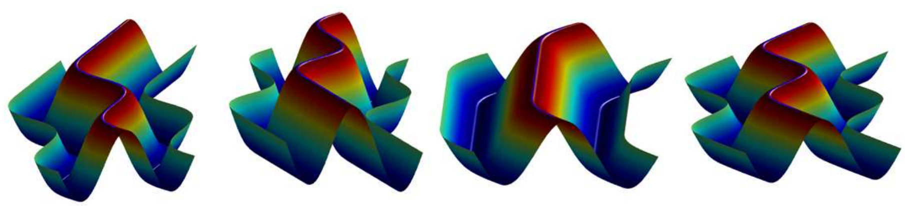

(A) (B) (C) (D)

Figure 6.2: (A) and (B) shows two surfaces. (C) shows the averaging result of the two surface with arc-length correspondence between landmarks curves. Note that the shape of the landmarks is averaged out and cannot be preserved. (D) shows the averaging result with shape correspondence between landmark curves. Note that the shape of the landmark curve is well preserved.

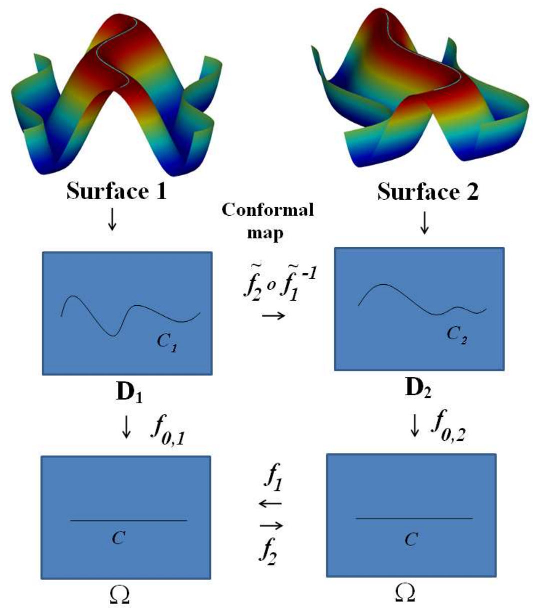

Figure 6.3: The figure show the framework of our algorithm.

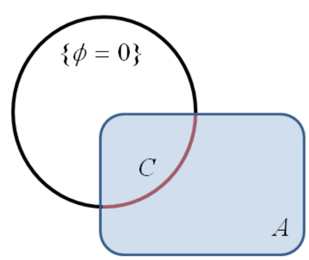

Figure 6.4: The figure shows the level set representation for C (Brown open curve), $C = \{\phi = 0\} \cap A$. A is the shaded region, $\{\phi = 0\}$ is the circle.

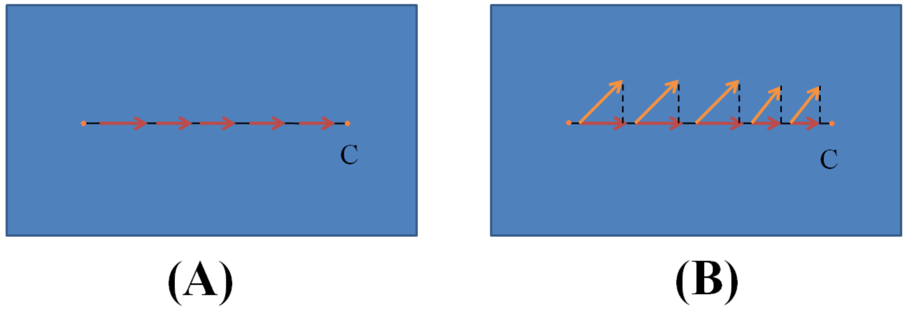

Figure 6.5: Illustration of how exact matching of landmark curves can be ensured by the projection of vector field. As shown in (A), the exact matching of landmark curves can be guranteed by restricting the vector field on C is parallel to the tangential direction of C. This requirement is satisfied by projecting the vector field along C to the horizontal component.

minimization of the following energy over diffeomorphisms $f_i : \Omega \to \Omega$ with $f_i(C) = C$. Denote $\tilde{f}_i = f_{0,i} \text{ o } f_i$, $F = [\tilde{f}_1, \tilde{f}_2]$,

$$E[f_1, f_2] = \int_\Omega |\nabla \tilde{f}_1|^2 \; + |\nabla \tilde{f}_2|^2 \; dx + \lambda \int_C \left(\kappa_1(\tilde{f}_1) - \kappa_2(\tilde{f}_2)\right)^2 |F_x \wedge F_y| \; ds \tag{6.4}$$

The first term is the harmonic energy of $\tilde{f}_i$. The second term is a *symmetric* shape term defined as an arc length integral over $F(C)$, similar to Thiruvenkadam et al. [111]. Here, the shape measure $\kappa_i(p_i)$ is determined by the geodesic curvature of M_i corresponding to the point p_i. Defining the symmetric shape measure over $F(C)$ makes the term independent of the choice of the initial maps $f_{0,i}$, and also avoids local minima problems that occur while matching flat curve segments.

In the above energy, using a search space of diffeomorphisms $f_i : \Omega \to \Omega$, and then imposing $f_i(C) = C$ as a constraint during minimization is difficult. Hence we propose a method to directly consider a *reduced search space* of diffeomorphisms $f_i : \Omega \to \Omega$ that satisfy $f_i(C) = C$.

6.4.2 Level Set Representation for C

Since we are dealing with the sulcal curves as our landmarks, we assume that $C = \cup_{k=1}^{N} \Gamma_k$, a union of open curves $\Gamma_k \subset \Omega$. We represent C implicitly in level set form to be able to write the second integral in energy (6.4) with respect to x. Being the union of open curves, C can be represented as the intersection of the 0-level set of a signed distance function ϕ, and a region A (Fig. 6.3(right)). Then the arc length integral of C becomes

$$\int_C ds = \int_\Omega \chi_A \, |\nabla H(\phi)| \, dx,$$

where $H(t)$ is a regularized version of the Heaviside function.

6.4.3 Modelling the Search Space for f_i

To construct an appropriate search space for f_i, we consider smooth vector fields, $\vec{X}_i = a_i \frac{\partial}{\partial x} + b_i \frac{\partial}{\partial y}$, where $a_i, b_i : \Omega \to \Re$ are C^1 functions with compact support. Then the flow of $\vec{X}_i$, $\Phi^{\vec{X}_i}(\mathbf{x}, t)$ is given by the differential equation,

$$\begin{aligned} \frac{\partial \Phi^{\vec{X}_i}}{\partial t}(\mathbf{x}, t) &= \vec{X}_i(\Phi^{\vec{X}_i}(\mathbf{x}, t)), \\ \Phi^{\vec{X}_i}(\mathbf{x}, 0) &= \mathbf{x}. \end{aligned}$$

Then the time-1 flow $\Phi^{\vec{X}_i}(\mathbf{x}, 1) : \Omega \to \Omega$ is a diffeomorphism.

Now let $\vec{n} := \tilde{\delta}(\phi) \, \tilde{\chi}_A \nabla \phi$, for regularized versions $\tilde{\delta}$, $\tilde{\chi}_A$ of the Dirac-δ function, and χ_A. We see that $\vec{n}$ coincides with the unit-normal vector field on C. Let η_{ep} be a smooth function on Ω such that $\eta_{ep} = 0$ at the endpoints of the open curves

$\Gamma_k \subset C$, $k = 1, 2, ..N$. Consider the vector fields $\vec{Y_i}$ that do not *flow across* C,

$$\vec{Y_i} = P_C X_i := \eta_{ep} \left(\vec{X_i} - (\vec{X_i} \cdot \vec{n})\vec{n}_i\right).$$

This property of the vector field is important to ensure the diffeormorphism obtained matches landmarks exactly. Figure 6.5 illustrates the idea of how exact matching of landmark curves can be ensured. As shown in (A), the exact matching of landmark curves can be guranteed by restricting the vector field on C is parallel to the tangential direction of C. This requirement is satisfied by projecting the vector field along C to the horizontal component.

We notice the following properties for the time-1 flow, $\Phi^{\vec{Y_i}}(., 1)$,

- $\Phi^{\vec{Y_i}}(., 1) : \Omega \to \Omega$ is a diffeomorphism since $\vec{Y_i}$ is C^1.
- Also $\vec{Y_i}|_C$ is a C^1 vector field *on* C. Thus $\Phi^{\vec{Y_i}}(., 1)|_C$ is a diffeomorphism onto C.

Hence it is natural to set $f_i = \Phi^{\vec{Y_i}}(., 1)$.

6.4.4 Energy

We formulate the energy (6.4) over the space of C^1 smooth vector fields on Ω, $\vec{X_i} = a_i \frac{\partial}{\partial x} + b_i \frac{\partial}{\partial y}$,
$J[a_i, b_i] =$

$$\int_\Omega |\nabla \tilde{f}_1|^2 \ + |\nabla \tilde{f}_2|^2 \ dx + \lambda \int_\Omega \chi_A \big(\kappa_1(\tilde{f}_1) - \kappa_2(\tilde{f}_2)\big)^2 \ |\nabla H(\phi)| \ |F_x \wedge F_y| \ dx$$
$$+\beta \int_\Omega |D\vec{X}_1|^2 + |D\vec{X}_2|^2 \ dx \qquad (6.5)$$

Here, as before $\tilde{f}_i = f_{0,i}$ o f_i, and $f_i = \Phi^{\vec{Y}_i}(.,1)$, the time-1 flow of the vector field $\vec{Y}_i = P_C X_i$. The last integral in the energy is the smoothness term for the vector fields $\vec{X}_i$.

6.5 Minimization of the energy

We are going to briefly describe how we derive the Euler-Lagrange equation of the energy functional.

In this work, we formulate the energy functional over the space of C^1 smooth vector fields on Ω, $\vec{X}_i = a_i \frac{\partial}{\partial x} + b_i \frac{\partial}{\partial y}$,

$J[a_i, b_i] =$

$$\int_\Omega |\nabla \tilde{f}_1|^2 \; + |\nabla \tilde{f}_2|^2 \; dx + \lambda \int_\Omega \chi_A \big(\kappa_1(\tilde{f}_1) - \kappa_2(\tilde{f}_2)\big)^2 \; |\nabla H(\phi)| \; |F_x \wedge F_y| \; dx$$
$$+\beta \int_\Omega |D\vec{X}_1|^2 + |D\vec{X}_2|^2 \; dx \qquad (6.6)$$

Here, as before $\tilde{f}_i = f_{0,i}$ o f_i, and $f_i = \Phi^{\vec{Y}_i}(.,1)$, the time-1 flow of the vector field $\vec{Y}_i = P_C X_i$. The last integral in the energy is the smoothness term for the vector fields $\vec{X}_i$. The Euler Lagrange equations of (6.6) are derived here. Let $D_v^\eta F = \frac{d}{d\epsilon} F(v + \epsilon\eta)$ denote the derivative of a functional F with respect to variable v, and for variation η. Also denote the vector fields $\vec{e}_1 := \frac{\partial}{\partial x}$, $\vec{e}_2 := \frac{\partial}{\partial y}$.

It follows that,

$$\begin{aligned} D_{a_i}J(\eta) = -\int_\Omega \Delta\tilde{f}_i\ Df_{0,i}\ D^\eta_{a_i} f_i\ dx + \lambda\int_\Omega \chi_A(-1)^{i-1}\big(\kappa_1(\tilde{f}_1) - \kappa_2(\tilde{f}_2)\big) \\ \nabla\kappa_i Df_{0,i}\ D^\eta_{a_i} f_i|\nabla H(\phi)|\ |F_x \wedge F_y|\ dx + \lambda\int_\Omega \chi_A\big(\kappa_1(\tilde{f}_1) - \kappa_2(\tilde{f}_2)\big)^2 \\ \frac{1}{|F_x \wedge F_y|}(|F_y|^2 F_x \cdot D^\eta_{a_i} F_x + |F_x|^2 F_x \cdot D^\eta_{a_i} F_y - (F_x \cdot F_y)(F_x \cdot D^\eta_{a_i} F_y + F_y \cdot D^\eta_{a_i} F_x)) \\ |\nabla H(\phi)|dx - \int_\Omega \Delta a_i\ \eta\ dx \end{aligned} \tag{6.7}$$

Integrating the third term by parts gives,

$$\begin{aligned} -\lambda\int_\Omega \chi_A\nabla\cdot\big((\kappa_1(\tilde{f}_1) - \kappa_2(\tilde{f}_2))^2\frac{1}{|F_x \wedge F_y|}[|F_y|^2\partial_x f_i - (F_x \cdot F_y)\partial_y f_i\ ; \\ |F_x|^2\partial_y f_i - (F_x \cdot F_y)\partial_x f_i]\big)\ |\nabla H(\phi)|Df_{0,i}\ D^\eta_{a_i} f_i dx \end{aligned} \tag{6.8}$$

In the first two integrals, the term $D^\eta_{a_i} f_i$ is given by the flow equation of $\vec{Y}_i = P_C X_i$,

$$\begin{aligned} \frac{\partial\Phi^{\vec{Y}_i}}{\partial t}(x,t) = \vec{Y}_i(\Phi^{\vec{Y}_i}(x,t)), \\ \Phi^{\vec{Y}_i}(x,0) = x. \end{aligned}$$

Now computing the derivative with respect to a_i on both sides, for variation η gives the following differential equation, $P_i := D^\eta_{a_i}\Phi^{\vec{Y}_i}$,

$$\begin{aligned} \frac{\partial}{\partial t}P_i(x,t) = \eta P_C\vec{e}_1\ (\Phi^{\vec{Y}_i}(x,t)) + D\vec{Y}_i(\Phi^{\vec{Y}_i}(x,t))\ P_i(x,t), \\ P_i(x,0) = \mathbf{0}. \end{aligned} \tag{6.9}$$

Since $D\vec{Y}_i(\Phi^{\vec{Y}_i}(x,t))$ is continuous with respect to t, we have the existence of an orthogonal fundamental matrix Ψ_i, for the homogeneous system of (6.9). Then a solution for the above problem can be easily verified to be

$$P_i(x,t) = \Psi_i(x,t) \int_0^t \Psi_i^{-1}(x,s) P_C \vec{e}_1 \ (\Phi^{\vec{Y}_i}(x,s)) \eta(\Phi^{\vec{Y}_i}(x,s)) \ \ ds$$

Let $B_i := -\Delta \tilde{f}_i \, Df_{0,i} + \lambda \chi_A \left((-1)^{i-1} \big(\kappa_1(\tilde{f}_1) - \kappa_2(\tilde{f}_2) \big) \nabla \kappa_i - \nabla \cdot C_i \right) Df_{0,i} \, |\nabla H(\phi)|$, where $C_i = (\kappa_1(\tilde{f}_1) - \kappa_2(\tilde{f}_2))^2 \ \frac{1}{|F_x \wedge F_y|} [|F_y|^2 \partial_x f_i - (F_x \cdot F_y) \partial_y f_i \ ; |F_x|^2 \partial_y f_i - (F_x \cdot F_y) \partial_x f_i]$. Substituting $D^{\eta}_{X_i} f_i = P_i(.,1)$ in (6.7), we have

$$D_{a_i} J(\eta) = \int_\Omega B_i(x) \ \Psi_i(x,1) \ \int_0^1 \Psi_i^{-1}(x,s) \ P_C \vec{e}_1 \ (\Phi^{\vec{Y}_i}(x,s)) \ \eta(\Phi^{\vec{Y}_i}(x,s)) \ \ ds \ dx \\ - \int_\Omega \Delta a_i \ \eta \ dx$$

For a fixed s, $\Phi^{\vec{Y}_i}(y,s) : \Omega \to \Omega$, is a diffeomorphism; denote the inverse map by $\phi_s^{\vec{Y}_i}$, and its Jacobian by $|D\phi_s^{\vec{Y}_i}|$. Change of variables $(x,s) \to (y = \Phi^{\vec{Y}_i}(x,s), s)$ in the first term gives

$$\int_\Omega B_i(\phi_s^{\vec{Y}_i}(y)) \ \int_0^1 \Psi_i(\phi_s^{\vec{Y}_i}(y),1) \ \Psi_i^{-1}(\phi_s^{\vec{Y}_i}(y),s) \ P_C \vec{e}_1 \ (y) \ |D\phi_s^{\vec{Y}_i}(y)| \ \eta(y) \ \ ds \ dy$$

Thus the Euler Lagrange equations are

$$\frac{da_i}{dt} = \int_0^1 B_i(\phi_s^{\vec{Y}_i}) \ \Psi_i(\phi_s^{\vec{Y}_i},1) \ \Psi_i^{-1}(\phi_s^{\vec{Y}_i},s) \ P_C \vec{e}_1 \ \ |D\phi_s^{\vec{Y}_i}| \ ds - \beta \Delta a_i$$
$$\frac{db_i}{dt} = \int_0^1 B_i(\phi_s^{\vec{Y}_i}) \ \Psi_i(\phi_s^{\vec{Y}_i},1) \ \Psi_i^{-1}(\phi_s^{\vec{Y}_i},s) \ P_C \vec{e}_2 \ \ |D\phi_s^{\vec{Y}_i}| \ ds - \beta \Delta b_i,$$

where: $B_i := -\Delta \tilde{f}_i \, Df_{0,i} + \lambda \chi_A \left((-1)^{i-1} \big(\kappa_1(\tilde{f}_1) - \kappa_2(\tilde{f}_2) \big) \nabla \kappa_i - \nabla \cdot C_i \right) Df_{0,i} \, |\nabla H(\phi)|$;

Ψ_i is the orthogonal fundamental matrix for the homogeneous system of

$$\frac{\partial}{\partial t}P_i(x,t) = \eta P_C \vec{e}_1\ (\Phi^{\vec{Y}_i}(x,t)) + D\vec{Y}_i(\Phi^{\vec{Y}_i}(x,t))\ P_i(x,t),\ \ P_i(x,0) = \mathbf{0}.$$

6.6 Computer Algorithm

To summarize, the algorithm for computing the optimized shape-based landmark matching conformal diffeomorphisms between cortical surfaces is as follow:

$\underline{\textbf{Algorithm 6.5.1}: \textbf{ Shape} - \textbf{based landmark matching diffeomorphism}}$

Input : Conformal parameterization $\phi_1 : S_1 \to D_1$, $\phi_2 : S_2 \to D_2$ of S_1 and S_2 respectively. Initial maps $f_{0,1} : D_1 \to \Omega$, $f_{0,2} : D_2 \to \Omega$, time step dt, energy threshold ε, β

Output : Optimized shape-based landmark matching conformal diffeomorphisms $G_{1,2} : S_1 \to S_2$ and $G_{2,1} : S_2 \to S_1$

1. Set $n = 0$. Set $\vec{X}_i^0 = (a_i^0, b_i^0) = (0,0)$ everywhere on Ω for $i = 1,2$. Compute energy $E_0 = E[f_1, f_2]$.
2. Compute $\vec{Y}_i^n = P_C\vec{X}_i$; $\phi_S^{\vec{Y}_i^n} : \Omega \to \Omega$; Orthogonal fundamental matrix Ψ_i^n; $B_i(\phi_S^{\vec{Y}_i^n})$ for $i = 1,2$
3. Update (a_i^n, b_i^n) by:

$$a_i^{n+1} = [\int_0^1 B_i(\phi_s^{\vec{Y}_i})\ \Psi_i(\phi_s^{\vec{Y}_i},1)\ \Psi_i^{-1}(\phi_s^{\vec{Y}_i},s)\ P_C\vec{e}_1\ \ |D\phi_s^{\vec{Y}_i}|\ ds - \beta\Delta a_i]dt + a_i^n$$

$$b_i^{n+1} = [\int_0^1 B_i(\phi_s^{\vec{Y}_i})\ \Psi_i(\phi_s^{\vec{Y}_i},1)\ \Psi_i^{-1}(\phi_s^{\vec{Y}_i},s)\ P_C\vec{e}_2\ \ |D\phi_s^{\vec{Y}_i}|\ ds - \beta\Delta b_i]dt + b_i^n$$

4. Compute energy $E_{n+1} = E[f_1, f_2]$

5. If $E_{n+1} - E_n < \varepsilon$, stop and return $G_{1,2} = \phi_2^{-1} \circ f_{0,2}^{-1} \circ f_2 \circ f_{0,1}^{-1} \circ \phi_1$, $G_{2,1} = \phi_1^{-1} \circ f_{0,1}^{-1} \circ f_1 \circ f_{0,2}^{-1} \circ \phi_2$. Otherwise, repeat step 2 to step 4.

6.7 Experimental Results

We have tested our algorithm on synthetic surfaces. Figure 6.6 shows the matching result of the synthetic surfaces with two sharp corners. Figure 6.6(A) shows a synthetic surface. It is mapped to another synthetic surface through parameterizations without the shape based correspondence between landmark curves, as shown in (B). Note that the correspondence between the landmark curves does not follow the shape information ([See the yellow dot]). (C) shows the result of matching using our proposed algorithm. Note that the correspondence between the landmark curves follows the shape information (corners to corners [See the yellow dot]). Figure 6.7 shows the matching result of the synthetic surfaces with three sharp corners. (A) shows one synthetic surface with three sharp corners. Again, it is mapped to another synthetic surface through parameterizations without the shape based correspondence between landmark curves, as shown in (B). The correspondence between the landmark curves does not follow the shape information. (C) shows the result of matching using our proposed algorithm. The correspondence between the landmark curves follows the shape information. We have also tested our algorithm on cortical hemispheric surfaces extracted from brain MRI scans, acquired from normal subjects at 1.5 T (on a GE Signa scanner). Experimental results show that our algorithm can effectively compute cortical surface parameterizations that align the landmark features in a way that also enforces shape correspondence, while preserving the conformality

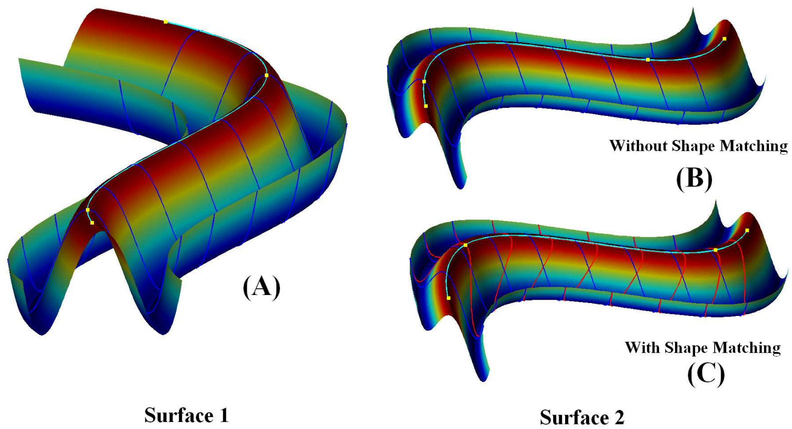

Figure 6.6: The figure shows matching result of the synthetic data with two sharp corners.

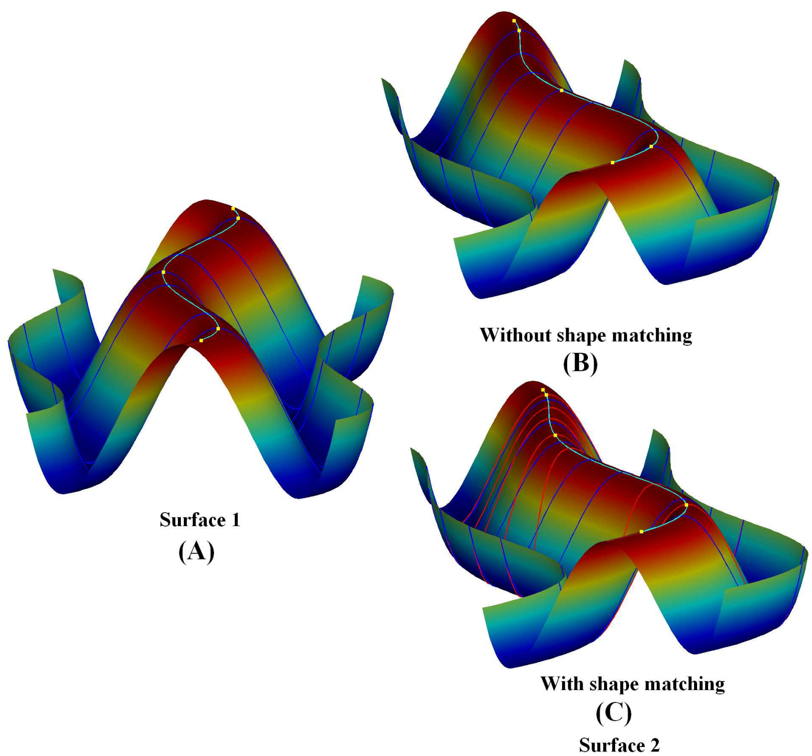

Figure 6.7: The figure shows matching result of the synthetic data with three sharp corners.

of the surface-to-surface mapping to the greatest extent possible. The computed map is guaranteed to be a diffeomorphism because the map is formulated as the integral flow of a smooth vector field.

Figure 6.8 shows two different cortical surfaces with sulcal landmarks labeled on them. We seek parameterizations of these surfaces that align the landmark features consistently while optimally preserving conformality. A diffeomorphism between the two surfaces is then obtained by computing the composition of the two parameterizations. Figure 6.9 shows the result of matching the cortical surfaces with one landmark labeled (for purposes of illustration) on each brain. Figure 6.9(A) shows the cortical surface of Brain 1. It is mapped to the cortical surface of Brain 2 under the conformal parameterization as shown in Figure 6.9(B). Note that the sulcal landmark on Brain 1 is only mapped approximately to the sulcal region on Brain 2. It is not mapped exactly to the corresponding sulcal landmark on Brain 2. Figure 6.9(C) shows the matching result under the parameterization we propose in this paper. Note that the corresponding landmarks are mapped exactly. Also, the correspondence between the landmark curves follows the shape information. It maps the secondary features of one landmark curve to the secondary features of the other landmark curve (See the black dots). Figure 6.9(D) and (E) show the standard 2D parameter domain of Brain 1 and Brain 2 respectively. The landmark curve is mapped to same horizontal line and the shape feature are mapped to the same positions (see the black dots). This is advantageous as the surface average of many subjects would retain features that consistently occur on sulci, while uniform speed parameterizations may cause these features to cancel out (please see Figure 6.2 for illustration). Figure 6.10 gives an illustration of the matching results for cortical surfaces with several sulcal landmarks labeled on them. Figure 6.10(A) shows the brain surface 1 with several landmarks labeled. It is mapped to brain surface 2 under the conformal

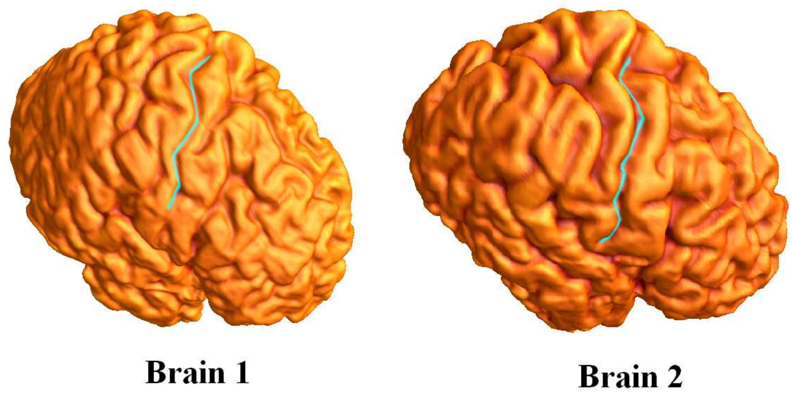

Figure 6.8: The figure shows two different cortical surfaces with sulcal landmarks.

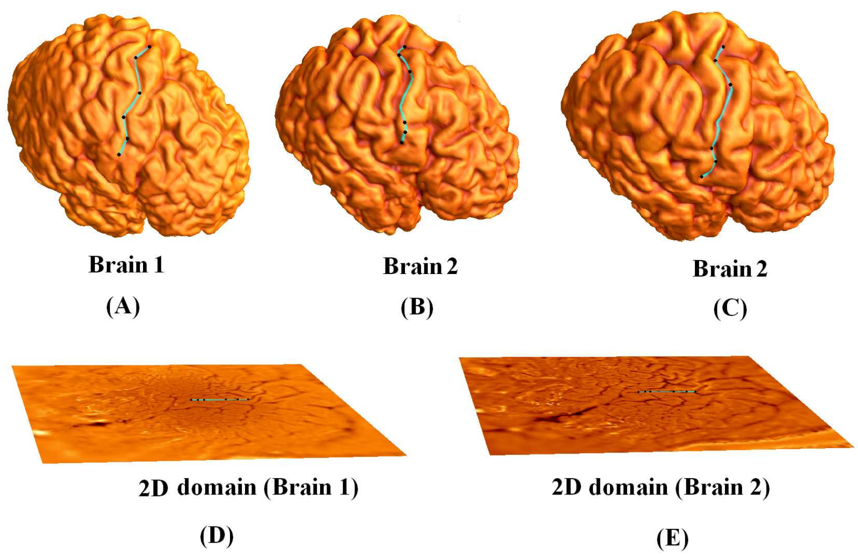

Figure 6.9: This figure shows the result of matching the cortical surfaces with one landmark labeled. (A) shows the surface of Brain 1. It is mapped to Brain 2 under conformal parameterization, as shown in (B). (C) shows the result of matching using our proposed algorithm. (D) and (E) show the standard 2D parameter domains for Brain 1 and Brain 2 respectively.

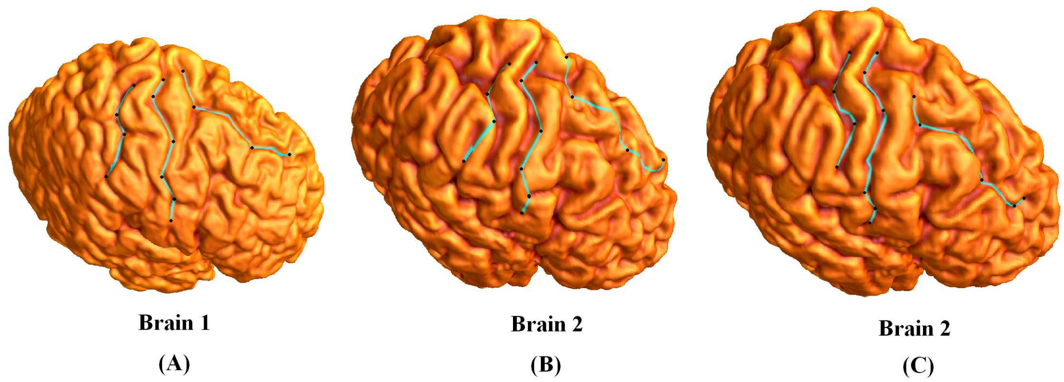

Figure 6.10: Illustration of the result of matching the cortical surfaces with several sulcal landmarks. (A) shows the brain surface 1. It is mapped to brain surface 2 under the conformal parameterization as shown in (B). (C) shows the result of matching under our proposed parameterization.

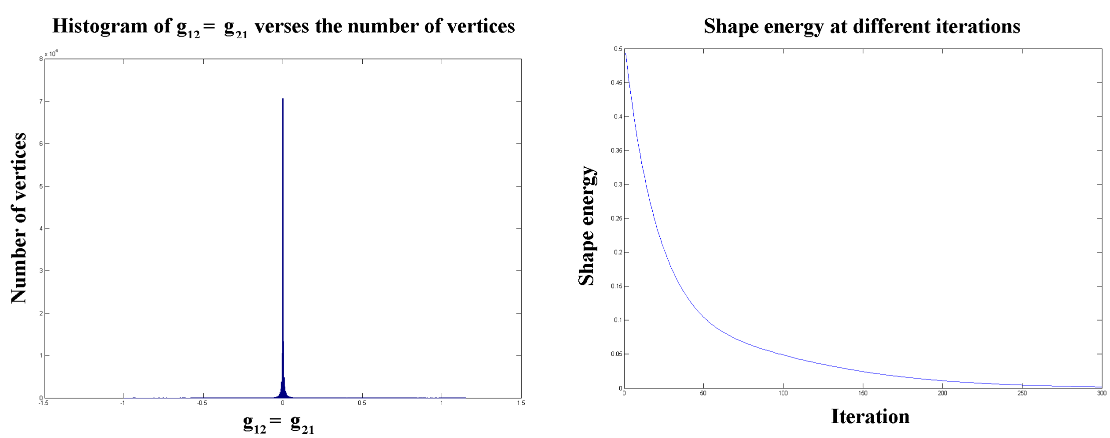

Figure 6.11: The left shows the histogram of $g_{12} = g_{21}$ of the brain surface under the parameterization computed with our algorithm. The right shows the shape energy at different iterations.

parameterization as shown in Figure 6.10(B). Again, the sulcal landmarks on Brain 1 are only mapped approximately to the sulcal regions on Brain 2. Figure 6.10(C) shows the matching result under the parameterization we proposed. The corresponding landmarks are mapped exactly. Also, the correspondence between the landmark curves follows the shape information (corners to corners [See the black dot]). To examine the conformality of the parameterization, we show in Figure 6.11(**Left**) the histogram of $g_{12} = g_{21}$ of the Riemannian metric under the parameterization computed with our proposed algorithm. Observe that $g_{12} = g_{21}$ are very close to zero at most vertices. This means that the Riemannian metric is a diagonal matrix, thus the parameterization computed is very close to conformal. It also shows that conformal map being intrinsic to global surface geometry, is not significantly affected by small changes in the local geometry induced by the shape term. Figure 6.11(**Right**) shows that the shape energy is decreasing with iterations, implying an improving shape based correspondence between the landmark curves.

6.8 Conclusion

In this paper, we developed an algorithm to find parametrizations of the cortical surfaces that are close to conformal and also give a *shape based* correspondence between embedded landmark curves. We propose a variational approach by minimizing an energy that measures the harmonic energy of the parameterization *maps*, and the shape dissimilarity between mapped points on the landmark curves. The parameterizations computed are guaranteed to give a *shape-based* diffeomorphism between the landmark curves. Experimental results show that our algorithm can effectively compute parameterizations of cortical surfaces that align landmark features consistently with shape correspondence, while preserving the conformality as much as possible. As future work, we plan to apply this algorithm to cortical models from healthy and diseased subjects to build population shape averages. The enforcement of higher-order shape correspondences may allow subtle but systematic differences in cortical patterning to be detected, for instance in neurodevelopmental disorders such as Williams syndrome, where the scope of cortical folding anomalies is of great interest but currently unknown. Another area of interest is to work on better numerical schemes to improve computational efficiency and accuracy.

References

[1] Wang, Y., Lui, L., Gu, X., Hayashi, K., Chan, T.F., Toga, A., Thompson, P., Yau, S.T.: Brain surface conformal parameterization using Riemann surface structure. IEEE Transactions on Medical Imaging **6** (2007) 853–865

[2] Lee, J.M.: Riemannian Manifolds. Springer (1997)

[3] Chern, S., Chen, W., Lam, K.: Lectures on Differential Geometry. World Scientific (1999)

[4] Carmo, M.P.D.: Differential Geometry of curves and surfaces. Prentice-Hall (1976)

[5] Jost, J.: Compact Riemann Surfaces: An Introduction to Contemporary Mathematics. Springer (1997)

[6] Boothby, W.: An introduction to Differential Manifolds and Riemannian Geometry. Academic (1986)

[7] Phillip Griffiths, J.H.: Principles of Algebraic Geometry. A Wiley-Interscience Publication (1994)

[8] Wang, Y., Jin, M., Chan, T.: Parameterize surfaces by surfaces. ACM Solid Physical Modeling Symposium, Beijing, China (2007)

[9] Strebel, K.: Quadratic Differentials. Springer (1984)

[10] Hoppe, H., DeRose, T., Duchamp, T., McDonald, J., Stuetzle, W.: Mesh optimiation. Annual conference of Computational Graph **27** (1993) in press.

[11] Schwartz, E., Shaw, A., Wolfson, E.: A numerical solution to the generalized mapmaker's problem: Flattening nonconvex polyhedral surfaces. IEEE Transaction of Pattern Analysis and Machine Intelligent **11** (1989) 1005–1008

[12] B.Timsari, Leahy, R.: An optimization method for creating semi-isometric flat maps of the cerebral cortex. SPIE Medical Imaging, San Diego, CA, U.S. (2000)

[13] Drury, H., Essen, D.V., Anderson, C., Lee, C., Coogan, T., Lewis, J.: Computerized mappings of the cerebral cortex: A multiresolution flattening method and a surface-based coordinate system. Journal of Cognitive Neuroscience **8** (1996) 1–28

[14] Carman, G., Drury, H., Essen, D.V.: Computational methods for reconstructing and unfolding of primate cerebral cortex. Cerebral Cortex **5** (1995) 506–517

[15] Hurdal, M.K., Stephenson, K.: Cortical cartography using the discrete conformal approach of circle packings. NeuroImage **23** (2004) S119–S128

[16] Stephenson, K.: An introduction to Circle Packing. Cambridge University Press (2005)

[17] Haker, S., Angenent, S., Tannenbaum, A., Kikinis, R., G. Sapiro, M.H.: Conformal surface parameterization for texture mapping. IEEE Transactions on Visualization and Computer Graphics (TVGC) **6** (2000) 181–189

[18] Angenent, S., Haker, S., Tannenbaum, A., Kikinis, R.: On the Laplace-Beltrami operator and brain surface flattening. IEEE Trans. Medical Imaging **18** (1999) 700–711

[19] Gu, X., Wang, Y., Chan, T.F., Thompson, P., Yau, S.T.: Genus zero surface conformal mapping and its application to brain surface mapping. IEEE Transaction on Medical Imaging **23** (2004) 949–958

[20] Wang, Y., Lui, L., Chan, T.F., P.Thompson: Optimization of brain conformal mapping with landmarks. MICCAI8th International Conference on Medical Image Computing and Computer Assisted Intervention (MICCAI) (2005)

[21] Gu, X., Yau, S.: Computing conformal structures of surfaces. Communication of Information System **2** (2002) 121–146

[22] Ju, L., Stern, J., Rehm, K., Schaper, K., Hurdal, M., Rottenberg, D.: Cortical surface flattening using least squares conformal mapping with minimal metric distortion. Proceeding of IEEE International Symposium of Biomedical Imaging: From Nano to Macro (2004) 77–80

[23] Joshi, A., Leahy, R., Thompson, P., D.W, S.: Cortical surface flattening using least squares conformal mapping with minimal metric distortion. Proceeding of IEEE International Symposium of Biomedical Imaging: From Nano to Macro (2004) 428–431

[24] Ju, L., Stern, J., Rehm, K., Schaper, K., Hurdal, M., Rottenberg, D.: Quantitative evaluation of three surface flattening methods. NeuroImage **28** (2005) 869–880

[25] Fischl, B., Sereno, M., Dale, A.: Cortical surface-based analysis ii: Inflation, flattening and a surface-based coordinate system. NeuroImage **9** (1999) 179–194

[26] Gu, X., Yau, S.T.: Global conformal surface parameterization. ACM Symposium on Geometry Processing 2003 (2003)

[27] Wang, Y., Gu, X., Hayashi, K., Chan, T.F., Thompson, P., Yau, S.: Brain surface parameterization using Riemann surface structure. Medical Image Computing and Computer-Assisted Intervention - MICCAI 2005 (2005) 657–665

[28] Drury, H., Essen, D.V., Corbetta, M., Snyder, A.: Surface-based analyses of the human cerebral cortex. In: Brain Warping. Academic Press (1999) 337–363

[29] Kelemen, A., Szekely, G., Greig, G.: Elastic model-based segmentation of 3D neuroradiological data sets. IEEE Transaction of Medical Imaging **18** (1999) 828–839

[30] Styner, M., Lieberman, J., Pantazis, D., Gerig, G.: Boundary and medial shape analysis of the hippocampus in schizophrenia. Medical Image Analysis **8** (2004) 197–203

[31] Csernansky, J., Wang, L., Jones, D., Rastogi-Cruz, D., Posener, J., Heydebrand, G., Miller, J., Miller, M.: Hippocampal deformities in schizophrenia characterized by high dimensional brain mapping. American Journal of Psychology **159** (2002) 2000–2006

[32] Gerig, G., Styner, M., Jones, D., Weinberger, D., Lieberman, J.: (Shape analysis of brain ventricles using SPHARM, journal = Proceeding in IEEE Computing Society MMBIA 2001 , year = 2001, optkey = , volume = , number = , pages = 171-178, month = Dec., optnote = , optannote =)

[33] B. Gutman, Y. Wang, L.L.T.C.P.T.: Hippocampal surface discrimination via invariant descriptors of spherical conformal maps. IEEE International Symposium on Biomedical Imaging - From Nano to Macro (ISBI), Washington D.C., USA (2007) 1316–1319

[34] B. Gutman, Y. Wang, L.L.T.C.P.T.: Hippocampal surface analysis using spherical harmonic function applied to surface conformal mapping. 8th International Conference on Pattern Recognition (ICPR), Hong Kong, China **3** (2006) 964–967

[35] Jin, M., Wang, Y., Gu, X., Chan, T.: Optimal global conformal surface parameterization for visualization. Proceeding of IEEE Visualization, Austin, TX **2** (2004) 267–274

[36] Wang, Y., Chiang, M., Thompson, P.: Automated surface matching using mutual information applied to Riemann surface structure. Proceeding of Medical Imaging Computation, Computational and Assistant Intervention Part II (2005) 666 – 674

[37] Lui, L., Thiruvenkadam, S., Wang, Y., Thompson, P., Chan, T.F.: Optimized conformal parameterizations of cortical surfaces using shape based landmark matching. UCLA CAM Report (08-14) (2008)

[38] L. M. Lui, Y. Wang, T.C., Thompson, P.: A landmark-based brain conformal parametrization with automatic landmark tracking technique. International Conference on Medical Image Computing and Computer Assisted Intervention - MICCAI **4191** (2006) 308–316

[39] L. M. Lui, Y. Wang, T.C., Thompson, P.: Automatic landmark tracking applied to optimize brain conformal mapping. IEEE International Symposium on Biomedical Imaging: From Nano to Macro (ISBI), Arlington, VA (2006) 205–208

[40] Gu, X., Wang, Y., Yau, S.: Geometric compression using riemann surface structure. Communication of Information System **3** (2003) 171–182

[41] L.M. Lui, Y. Wang, J.K., Yau, S.T.: Computation of curvatures using conformal parameterization. (Accepted by Communications in Information and Systems)

[42] Fischl, B., Sereno, M., Tootell, R., Dale, A.: High-resolution intersubject averaging and a coordinate system for the cortical surface. In: Human Brain Mapping. Volume 8. (1999) 272–284

[43] Thompson, P., Toga, A.: A surface-based technique for warping 3-dimensional images of the brain. IEEE Transaction of Medical Imaging **15** (1996) 1–16

[44] Davatzikos, C.: Spatial normalization of 3d brain images using deformable models. Computer Assisted Tomography **20** (1996) 656–665

[45] Lui, L., Wang, Y., Chan, T.F., Thompson, P.: Brain anatomical feature detection by solving partial differential equations on general manifolds. Discrete and Continuous Dynamical Systems B **7** (2007) 605–618

[46] Lui, L., Wang, Y., Chan, T.F., Thompson, P.: Landmark constrained genus zero surface conformal mapping and its application to brain mapping research. Applied Numerical Mathematics **57** (2007) 847–858

[47] Y. Wang, L.M. Lui, T.C., Thompson, P.: Combination of brain conformal mapping and landmarks: A variational approach. Proceedings of the Eighth IASTED International Conference, Computer Graphics and Imaging (CGIM),Honolulu, HI, USA (2005) 70–75

[48] Glaunès, J., Vaillant, M., Miller, M.: Landmark matching via large deformation diffeomorphisms on the sphere. J. Maths. Imaging and Vision **20** (2004) 179–200

[49] Leow, A., Yu, C., Lee, S., Huang, S., Protas, H., Nicolson, R., Hayashi, K., Toga, A., Thompson, P.: Brain structural mapping using a novel hybrid implicit/explicit framework based on the level-set method. NeuroImage **24** (2005) 910–927

[50] Thompson, P., Woods, R., Mega, M., Toga, A.: Mathematical/computational challenges in creating population-based brain atlases. Human Brain Mapping **9** (2000) 81–92

[51] Tosun, D., Rettmann, M., Prince, J.: Mapping techniques for aligning sulci across multiple brains. Med. Image Anal. **8** (2004) 295–309

[52] Thompson, P., et al.: Mapping cortical change in alzheimer's disease, brain development, and schizophrenia. NeuroImage **23** (2004) S2–S18

[53] Chan, T.F., Shen, J.: Non-texture inpainting by curvature-driven diffusions (CDD). Journal of Visual Communication and Image Representation **12** (2001) 436–449

[54] Vese, L.A., Chan, T.F.: Multiphase level set framework for image segmentation using the Mumford and Shah model. International Journal of Computer Vision **50** (2002) 271–293

[55] Rudin, L., Osher, S., Fatemi, E.: Nonlinear total variation based noise removal algorithms. Physica D: Nonlinear Phenomena **60** (1992)

[56] Blomgren, P., Chan, T.F.: Color TV: Total variation methods for restoration of vector valued images. IEEE Transaction on Image Processing **7** (1998) 304–309

[57] Chan, T.F., Sandberg, B.Y., Vese, L.A.: Active contours without edges for vector-valued images. Journal of Visual Communication and Image Representation **11** (2000) 130–141

[58] Gelfand, I.M., Fomin, S.V.: Calculus of Variations. Dover (2000)

[59] Bertalmio, M.: Processing of flat and non-flat image information on arbitrary manifolds using partial differential equations. University of Minnesota, Ph.D Thesis (2001)

[60] Clarenz, U., Rumpf, M., Telea, A.: Surface processing methods for point sets using finite elements. Journal of Computers and Graphics **28** (2004) 851–868

[61] Thompson, P., Woods, R., Mega, M.S., Toga, A.: Mathematical/computational challenges in creating deformable and probablistic atlases of the human brain. IEEE Transactions on Visualization and Computer Graphics (TVGC) **9** (2000) 81–92

[62] Thompson, P., Giedd, J., Woods, R., MacDonald, D., Evans, A., Toga, A.: Growth patterns in the developing human brain detected using continuum-mechancial tensor mapping. Nature **404** (2000) 190–193

[63] Lui, L., Wang, Y., Chan, T.F.: Solving PDEs on manifold using global conformal parameterization. IEEE Transaction on Medical Imaging:Variational, Geometric, and Level Set Methods in Computer Vision: Third International Workshop, VLSM 2005 (2005) 307–319

[64] Verdera, J., Caselles, V., Bertalmio, M., Sapiro, G.: Inpainting surface holes. Proceeding of International Conference on Image Processing, 2003 (ICIP 2003). **2** (2003) 903–906

[65] Stam, J.: Flows on surfaces of arbitrary topology. Proceedings of ACM SIGGRAPH 2003 **22** (2003) 724–731

[66] Lopez-Perez, L., Deriche, R., Sochen, N.: The Beltrami flow over triangulated manifolds. Computer Vision and Mathematical Methods in Medical and Biomedical Image Analysis **3117** (2004) 135–144

[67] Turk, G.: Generating textures on arbitrary surfaces using reaction-diffusion. Computer Graphic (SIGGRAPH '91) **25** (1991) 289–298

[68] Witkin, A., Kass, M.: Reaction-diffusion textures. Proceedings of the 18th annual conference on computer graphics and interactive techniques (1991) 299–308

[69] Diewald, U., Preusser, T., Rumpf, M.: Anisotropic diffusion in vector field visualization on Euclidean domains and surfaces. IEEE Transaction on Visualization and Computer Graphics **6** (2000) 139–149

[70] Dorsey, J., Hanrahan, P.: Digital materials and virtual weathering. Scientific American **282** (2000) 46–53

[71] Praun, E., Finkelstein, A., Hoppe, H.: Lapped textures. Proceedings of SIGGRAPH 2000 (2000)

[72] Winkenbach, G., Salesin, D.: Rendering parametric surfaces in pen and ink. Computer Graphic (SIGGRAPH 96) (1996) 469–476

[73] Faugeras, O., Clement, F., Deriche, R., Keriven, R., Papadopoulo, T., Roberts, J., Vieville, T., Devernay, F., Gomes, J., Hermosillo, G., Kornprobst, P., Lingrand, D.: The inverse EEG and MEG problems: The adjoint state approach I: The continuous case. INRIA Research Report (1999)

[74] Stam, J.: Stable fluids. Proceedings of the 26th annual conference on computer graphics and interactive techniques (2002)

[75] M. Desbrun, A.N. Hirani, J.M.: Discrete exterior calculus for variational problems in computer vision and graphics. 42nd IEEE Conference on Decision and Control. Proceedings. **5** (2003) 4902–4907

[76] Burger, M.: Finite element approximation of elliptic partial differential equations on implicit surfaces,. Advances in multiresolution for geometric modelling **04** (2004)

[77] Xu, G., Pan, Q., Bajaj, L.C.L.: Discrete surface modelling using partial differential equations. Computer Aided Geometric Design **23** (2006) 125–145

[78] Osher, S., Sethian, J.: Fronts propagating with curvature dependent speed: Algorithms based on hamilton-jacobi formulations. Journal of Computational Physics **79** (1988) 12–49

[79] Memoli, F., Sapiro, G., Thompson, P.: Implicit brain imaging. Neuroimage **23** (2004) 179–188

[80] Marcelo Bertalmio, Li-Tien Cheng, S.O., Sapiro, G.: Variational problems and partial differential equations on implicit surfaces. Journal of Computational Physics **174** (2001) 759 – 780

[81] Ruuth, S., Merriman, B.: A simple embedding method for solving partial differential equations on surfaces. UCLA CAM Report **06** (2006)

[82] Bertalmio, M., Memoli, F., Cheng, L., Sapiro, G., Osher, S.: Variational problems and partial differential equations on implicit surfaces: Bye bye triangulated surfaces. Geometric Level Set Methods in Imaging, Vision and Graphics (2003) 381–398

[83] Cheng, L., Burchard, P., Merriman, B., Osher, S.: Motion of curves constrained on surfaces using a level-set approach. Journal of Computational Physics **175** (2002) 602–644

[84] Bertalmio, M., Sapiro, G., Cheng, L., Osher, S.: A framework for solving surface partial differential equations for computer graphics applications. CAM Report 00-43, UCLA, Mathematics Department. (2000)

[85] Ratz, A., Voigt, A.: PDE's on surfaces: a diffuse interface approach. Communications in Mathematical Sciences **4** (2006) 575–590

[86] Floater, M.S., Kai, H.: Surface parameterization: a tutorial and survey. Advances in multiresolution for geometric modelling (2005) 157–186

[87] Lui, L., Wang, Y., Chan, T.F.: Numerical analysis of solving PDEs on manifold via conformal parameteriation. (To be appeared in UCLA CAM Report (http://www.lokminglui.com/researchucla/LuiNumerical.pdf))

[88] Lopez-Perez, L., Deriche, R., Sochen, N.: The Beltrami flow over triangulated manifolds. Computer Vision and Mathematical Methods in Medical and Biomedical Image Analysis **3117** (2004) 135–144

[89] Chan, T.F., Shen, J.: Variational restoration of nonflat image features: Models and algorithms. SIAM Journal on Applied Mathematics **61** (2000) 1338–1361

[90] Tang, B., Sapiro, G., Caselles, V.: Diffusion of general data on non-flat manifolds via harmonic maps theory: The direction diffusion case. International Journal of Computer Vision **36** (2000) 149–161

[91] Spira, A., Kimmel, R.: Enhancing images painted on manifolds. Scale Space and PDE Methods in Computer Vision **3459** (2005) 492–502

[92] Breckon, T.P., Fisher, R.B.: Direct geometric texture synthesis and transfer on 3D meshes. 3rd European Conference on Visual Media Production (CVMP) (2006) 186–186

[93] Breckon, T.P., Fisher, R.B.: Non-parametric 3D surface completion. Proceedings of the Fifth International Conference on 3-D Digital Imaging and Modeling (2005) 573–580

[94] Goualher, L., Procyk, E., collins, D., Venugopal, C., Evans, A.: Automated extraction and variability analysis of sulcal neuroanatomy. IEEE Transaction of Medical Imaging **18** (1999) 206–217

[95] Klein, A., Hirsch, J., Ghosh, S., Tourville, J.: Mindboogle: A scatter-brained approach to automate brain labeling. NeuroImage **24** (2005) 261–280

[96] Fillard, Arsigny, V., Pennec, X., Hayashi, K., Thompson, P.: Measuring brain variability by extrapolating sparse tensor fields measured on sulcal lines. Res. Rep. INRIA 5887 (2007)

[97] Lui, L.M., Wang, Y., Chan, T.F., Thompson, P.: Automatic landmark tracking and its application to the optimization of brain conformal mapping. IEEE Computer Society Conference on Computer Vision and Pattern Recognition (CVPR), New York **2** (2006) 1784–1792

[98] Fidrich, M.: Iso-surface extraction in nD applied to tracking feature curves across scale. Image Vision Comput. **16** (1998) 545–556

[99] Thirion, J.: The extremal mesh and the understanding of 3D surfaces. International Journal of Computer Vision **19** (1996) 115–128

[100] Rettmann, M., Tosun, D., Tao, X., Resnick, S., Prince, J.: Program for the assisted labeling of sulcal regions (pals): Description and validation. NeuroImage **24** (2005) 398–416

[101] Rey, D., Subsol, G., Delingette, H., Ayache, N.: Automatic detection and segmentation of evolving processes in 3D medical images: Application to multiple sclerosis. Medical Image Analysis **6** (2002) 163–179

[102] Tao, X., Prince, J., Davatzikos, C.: Using a statistical shape model to extract sulcal curves on the outer cortex of the human brain. IEEE TMI **21** (2002) 513–524

[103] Lohmann, G., Kruggel, F., von Cramon, D.: Automatic detection of sulcal bottom lines in MR images of the human brain. IPMI **1230** (1997) 368–374

[104] Zeng, X., Staib, L., Schultz, R., Win, L., Duncan, J.: A new approach to 3D sulcal ribbon finding from MR images. 3rd MICCAI (1999)

[105] Kao, C., Hofer, M., Sapiro, G., Stern, J., Rottenberg, D.: A geometric method for automatic extraction of sulcal fundi. Proceeding in International Symposium of Biomedical Imaging: From Nano to Macro (2006) 1168–1171

[106] Rusinkiewicz, S.: Estimating curvatures and their derivatives on triangle meshes. Symp. on 3D Data Processing, Vis., and Trans. (2004)

[107] Cachia, A., Mangin, J., Rivire, D., Boddaert, N., Andrade, A., Kherif, F., Sonigo, P., Papadopoulos-Orfanos, D., Zibovicius, M., Poline, J., Bloch, I., Brunelle, F., Rgis, J.: A mean curvature based primal sketch to study the cortical folding process from antenatal to adult brain. Proceeding in Medical Image Computing and Computer-Assisted Intervention **2208** (2001) 897–904

[108] Mumford, D., Shah, J.: Optimal approximations by piecewise smooth functions and associated variational problems. Communication in Pure and Applied Mathematics **42** (1989)

[109] Lui, L., Wang, Y., Chan, T.F.: Solving PDEs on manifolds using global conference parametrization. VLSM, ICCV (2005)

[110] Thompson, P., Hayashi, K., Sowell, E., Gogtay, N., Giedd, J., Rapoport, J., de Zubicaray, G., Janke, A., Rose, S., Semple, J., Doddrell, D., Wang, Y., van Erp, T., Cannon, T., Toga, A.: Mapping cortical change in alzheimer's disease, brain development, and Schizophrenia. NeuroImage **23** (2004) S2–S18

[111] Thiruvenkadam, S., Groisser, D., Y.Chen: Non-rigid shape comparison of implicitly-defined curves. VLSM (2005)